THESIS

CONVERSION OF LOW BMEP 4-CYLINDER TO HIGH BMEP 2-CYLINDER LARGE BORE NATURAL GAS ENGINE

Submitted by

John Ladd

Department of Mechanical Engineering

In partial fulfillment of the requirements

For the degree of Master of Science

Colorado State University

Fort Collins, Colorado

Summer 2016

Master's Committee:

Advisor: Daniel B. Olsen

John Petro
Borgusz Bienkiewicz

ABSTRACT

CONVERSION OF LOW BMEP 4-CYLINDER TO HIGH BMEP 2-CYLINDER LARGE BORE NATURAL GAS ENGINE

There are more than 6,000 integral compressor engines in use on US natural gas pipelines, operating 24 hours a day, 365 days a year. Many of these engines have operated continuously for more than 50 years, with little to no modifications. Due to recent emission regulations at the local, state and federal levels much of the aging infrastructure requires retrofit technology to remain within compliance. The Engines and Energy Conversion Laboratory was founded to test these retrofit technologies on its large bore engine testbed (LBET). The LBET is a low brake mean effective pressure (BMEP) Cooper Bessemer GMVTF-4. Newer GMV models, constructed in 1980's, utilize turbocharging to increase the output power, achieving BMEP's nearly double that of the LBET. To expand the lab's testing capability and to reduce the LBET's running cost: material testing, in-depth modeling, and on engine testing was completed to evaluate the feasibility of uprating the LBET to a high BMEP two cylinder engine.

Due to the LBET's age, the crankcase material properties were not known. Material samples were removed from engine to conduct an in-depth material analysis. It was found that the crankcase was cast out of a specific grade of gray iron, class 25 meehanite. A complete three dimensional model of the LBET's crankcase and power cylinders was created. Using historical engine data, the force inputs were created for a finite element analysis model of the LBET, to determine the regions of high stress. The areas of high stress were instrumented with strain gauges to iterate and validate the model's findings.

Several test cases were run at the high and intermediate BMEP engine conditions. The model found, at high BMEP conditions the LBET would operate at the fatigue limit of the class 25 meehanite, operating with no factor of safety but the intermediate case were deemed acceptable.

ACKNOLEDGEMENTS

The author would like to recognize individual contributors to this work. There were numerous students and staff that played key roles with the research, analysis, testing, and modeling for this project. First and foremost, the author would like to recognize Dr. Daniel Olsen for his countless hours spent on this project and his selfless mentoring. The author would also like to recognize the committee members for their greatly appreciated contributions to the project, Dr. John Petro and Dr. Borgusz Bienkiewicz.

Kirk Evan, director of engineering at the EECL, was an amazing resource for analyzing and managing the vast amounts of data accumulated on this project. Joe Wilmetti, Smash Lab manager, for taking time out of his busy schedule to aid with tensile and hardness testing. Trevor Aguirre, AMPT researcher, for his assistance with imaging the material samples and demonstrating Archimedes' method for density calculation. Steve Johnson, Mechanical Engineering lab manger, for his assistance machining the material sample to desired size and shape. And last but not least, Dr. Christian Puttlitz for his tireless editing and meetings to improve the presentation of results seen in this report.

TABLE OF CONTENTS

LIST OF TABLES

LIST OF FIGURES

ABREVIATIONS AND SYMBOLS

Term	**Abbreviation**
Advanced Materials Processing and Testing Lab	AMPT
After Top Dead Center	ATDC
American Society for Metals	ASM
American Society of Mechanical Engineers	ASME
Brake horsepower	bhp
Brake mean effective pressure	BMEP
Brake Specific Fuel Consumption	BSFC
Computer Numerically Controlled	CNC
Electronic Gas Admission Valve	EGAV
Engines and Energy Conversion Laboratory	EECL
Finite Element Analysis	FEA
Gauge Factor	GF
Large Bore Engine Test Bed	LBET
Mechanical Gas Admission Valve	MGAV
Motor Sport Research Center	MERC
Pipeline Gas Admission Valve	PLGAV
Revolutions per Minute	rpm
Top Dead Center	TDC
Unburned Hydrocarbon Emissions	UHC

1 INTRODUCTION

In 2014, nearly 27 trillion cubic feet of natural gas was consumed in the United States [1]. Natural gas is primarily transported from drilling site to the end user via a vast network of pipelines spanning over 1.5 million miles [2]. To move the natural gas, the pipeline needs to maintain a constant pressure gradient, created by compressor stations spaced every 50 to 100 miles [3]. Many of these compressor stations have been in continuous operation for more than 50 years utilizing the power and reliability of integral compressors.

There are more than 6,000 integral compressors in use on US pipelines, operating 24 hours a day 365 days a year [3]. Integral compressors typically operate at slow speeds with the compressor cylinder directly attached to the combustion cylinder via an articulated connecting rod, Figure 1. Many of these engines have operated continuously for more than 50 years with little to no modifications [4]. Due to recent emissions regulations at the local, state and federal levels much of the aging infrastructure requires retrofit technology to remain within compliance or risks replacement. Retrofit technologies can improve efficiency and decrease emissions at a fraction of the cost of replacement. A large integral compressor operator can save over $4 million by uprating an old engine rather than installing a modern centrifugal compressor [5]. The large bore engine

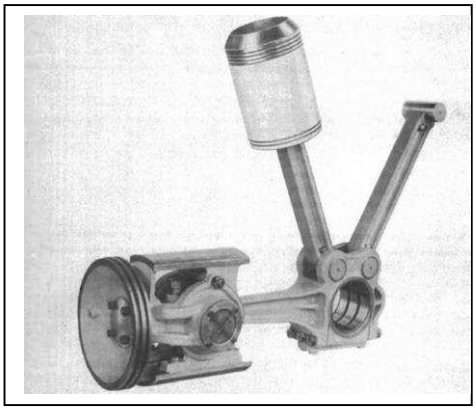

Figure 1: GMV Articulated Connecting Rod Assembly

testbed (LBET) at the Engines and Energy Conversion Laboratory (EECL) provides industry with means to test new technology without sacrificing compressor station throughput.

The EECL utilizes a Cooper Bessemer GMVTF-4 as the LBET. The engine is a slow speed, low brake mean effective pressure (BMEP), large bore integral compressor. Operating as a lean burn, two-stroke cycle engine, producing 440 brake horse power (bhp) at 300 revolutions per minute (rpm), with a 14" (36cm) bore and 14" (36cm) stroke and a total displacement of 140 liters. The engine is outfitted with over 100 independent sensors, allowing the measurement and analysis of pertinent parameters. The engine is loaded with a water-brake dynamometer to simulate compression work. The engine is controlled with a LabVIEW virtual Interface with the ability to attain a wide range of operational parameters to accurately simulate field engine conditions.

1.1 GOAL AND PURPOSE

The goal is to convert and uprate the current GMVTF-4 to a GMVH-2. The motivation for the uprate project is to expand the testing capabilities of the EECL as well as reducing the running and prototyping cost of the engine.

The GMVTF-4 was the second generation model produced by Cooper Bessemer, from 1948 to 1963, operating as a low BMEP (~67psi) model [6]. There were eight new models designed after the GMVTF that were more powerful and more efficient leading up to the high BMEP (~125psi) GMVH model. Uprating the engine to a GMVH would allow the EECL to conduct experiments at conditions that simulate the operation of every GMV model, as well as establishing an uprating practice. Deactivating two of the cylinders will reduce the research and development cost for engine retrofit companies, making the LBET more attractive to industry sponsors.

1.2 LITERATURE REVIEW

A comprehensive literature review was completed to establish the theoretical framework for the proposed work and identify the potential risks.

1.2.1 Engine Background

The EECL was started at Colorado State University with the installation of the GMVTF-4, to provide an independent, unbiased test facility for large-bore, industrial, natural gas engines. The LBET is equipped with over 100 state of the art measuring devices and controls for producing accurate emissions and performance data.

The Cooper Bessemer GMV was known for its excellent performance and ruggedness. In its 55 years of production 4616 models were produced at the Cooper Bessemer plant in Mount Vernon, Ohio [7]. The GMV integral compressor was recognized by the American Society of Mechanical Engineers (ASME) as a Heritage Landmark. The GMV was credited as a major contributor to the world's economy for more than a half century, providing compression energy for the natural gas transmission, gas treatment, petrochemical, refinery and power industries in the United States and forty-four countries around the world [7].

The Cooper Bessemer GMV design was an advancement over the traditional gas driven horizontal compressors. The GMV is a V-angle integral compressor, meaning the compression cylinders are directly attached to the power cylinders. The 60 degree V-angle design reduced the floor space requirements of the engine by up to one half of its horizontal compressor counterparts. The compactness of the engine allowed it to be shipped completely assembled, keeping the original factory alignments, reducing the complexity of installation.

The GMV is a two cycle engine, meaning every other stroke of the engine is a power stroke, having greater power density relative to its four cycle counterparts. On the downward stroke, the power piston first uncovers the exhaust ports allowing the some of the burned gases to exit the cylinder. Further movement of the piston then uncovers the air intake ports and the scavenging air in the receiver rushes into the cylinder sweeping the remaining exhaust gases out and filling the cylinder fresh air, seen on the right cylinder in Figure 2.The stock GMV utilized a trunk style piston with the power pistons controlling the opening and closing of the intake and exhaust ports. Scavenging air was provided by horizontal pistons attached to the cross heads. The stock savaging airflow can be seen in Figure 2 denoted by the white arrows. The LBET utilizes an external supercharger system in place of the scavenging pistons but the cross heads are still in place. At the time of port closure, the mechanically operated injector valve at the top of the cylinder opens and pressurized natural gas is admitted into the cylinder regulated by the governor in accordance with

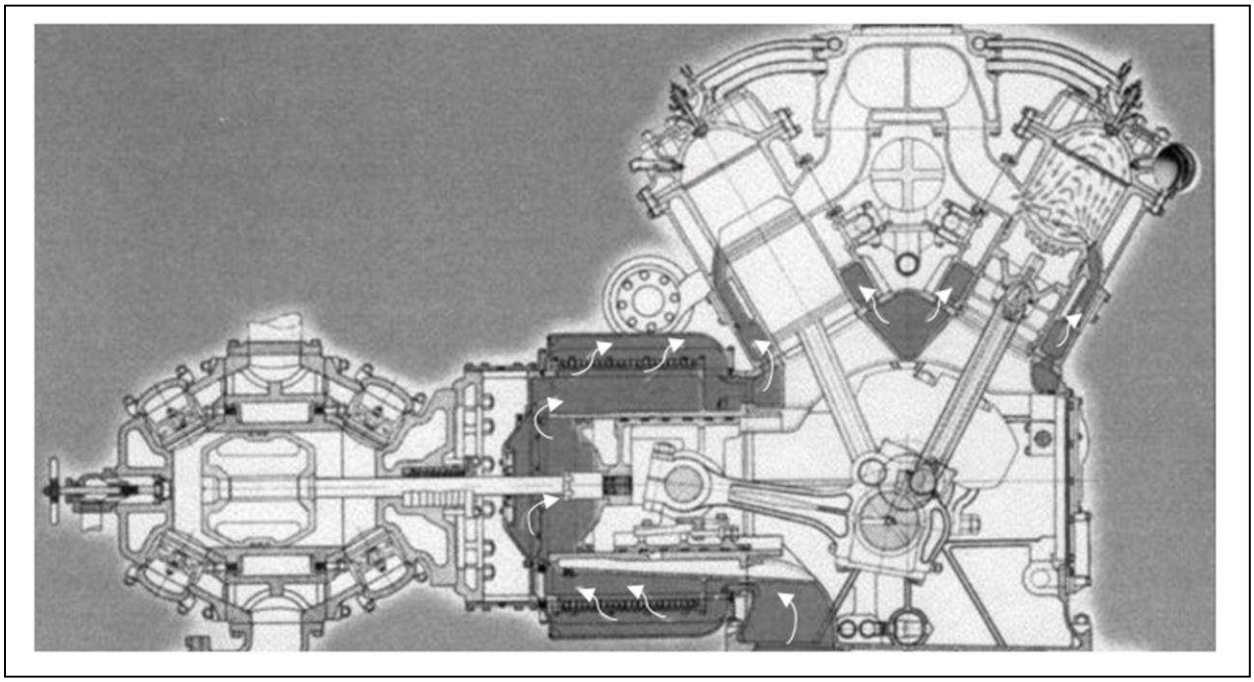

Figure 2: GMV Air Flow Schematic and Cross Section

the load requirements. Shortly before top dead center is reached, ignition takes place, combustion occurs and the cycle is then repeated.

1.2.2 Cylinder Deactivation

To be competitive, the lab needed the capability to simulate a wide range of atmospheric conditions. The requirement was fulfilled by using a supercharger, driven by an electric motor, and a variable back pressure valve. This combination allows the lab to emulate the pressures of a turbocharged engine at the desired altitude of an industry sponsor.

The current supercharger assembly consists of a 300hp Magnetek electric motor connected to Gardener CycloBlower via a V-belt and jackshaft. The current configuration is able to provide enough boost to run the LBET on all four cylinders at GMVA levels, a BMEP of ~72 psi. As configured the system would not be able to provide enough air flow to run the LBET at GMVH levels on four cylinders, but by deactivating two cylinders the system would meet the air throughput demands to run LBET as a GMVH-2 without modification. The need for cylinder deactivation was dictated by the limitation of the supercharger but will reduced associated costs on the LBET. A GMVH typically operates with over 20 inHg of boost and as can be seen in compressor flow curves of Figure 3, the SCFM exponentially decreases as boost level increases [8] [9].

The most common reason for field engine cylinder deactivation is due to reduced power requirements, often associated with depleting gas fields [10]. Large bore two-stroke compression engines are designed to run within a finite range of output power requirements with optimal

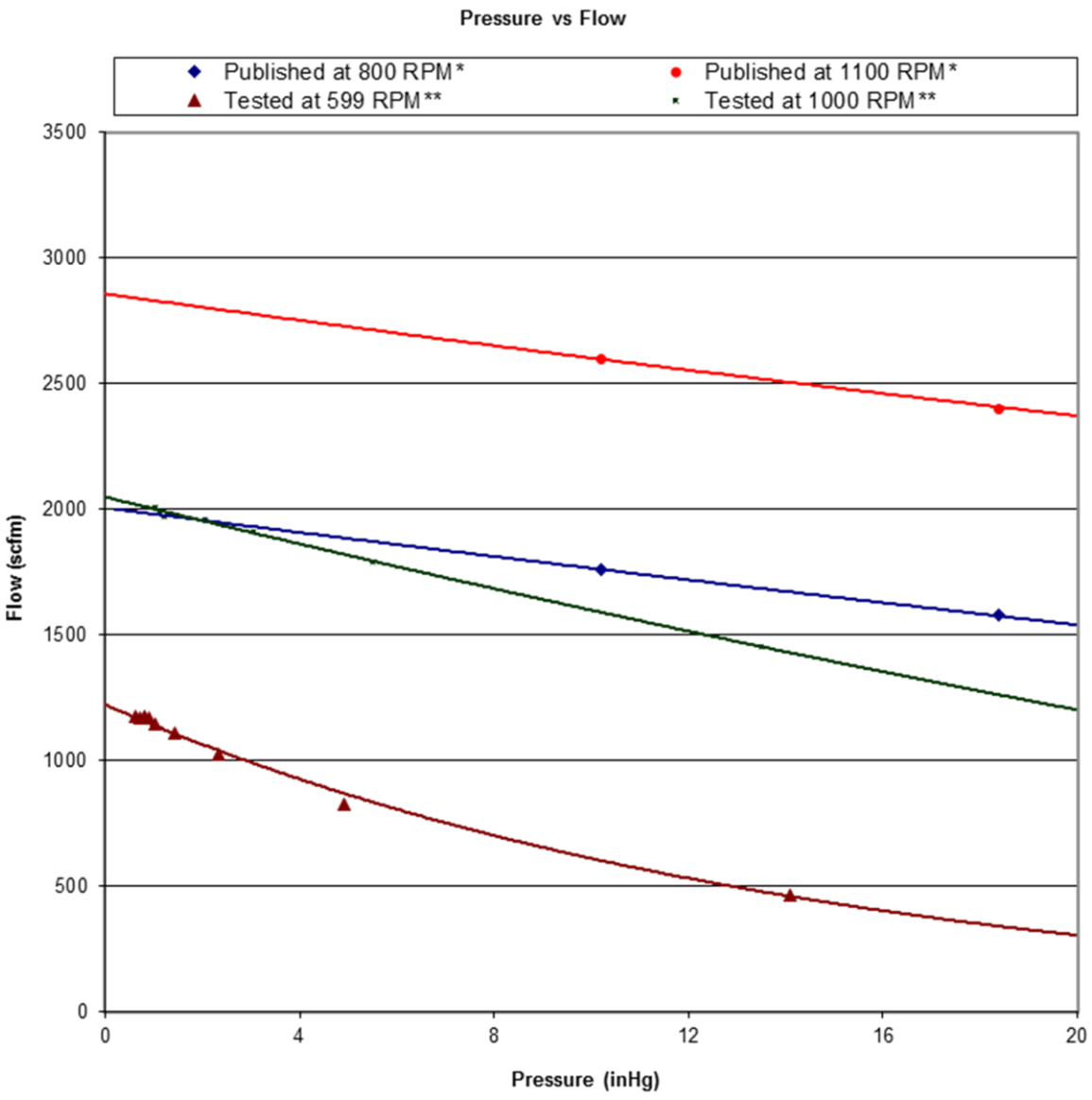

*Data obtained with inlet at 14.7 PSIA and 68 F with no recorded losses.

**Data obtained 110 ft downstream from blower, losses not accounted for.

Figure 3: EECL Supercharger Flow Curves [9]

efficiency at constant 100% load. Reduced load results in an increased propensity to misfire, increased brake specific fuel consumption (BSFC), decreased thermal efficiency, as well as increased emissions [11][12][13][10]. A misfire is considered to be any combustion cycle resulting in an IMEP of less than 10psi [11]. When a cylinder misfires there is incomplete combustion

resulting in high unburned hydrocarbon emissions (UHC's). UHC's represent wasted chemical energy being exhausted to the environment as well as having high warming potential. Old large bore engines, like the GMV, have a fixed air supply, also known as an uncontrolled engine. As load decreases in uncontrolled engines, the fuel governor reduces the fuel to the cylinder, making the in-cylinder mixture leaner [14]. With enough load decrease the engine will approach its lean limit and begin to misfire with increasing frequency, shown in Figure 5. Figure 4 and Figure 5 includes results for three different fuel injection technologies, mechanical gas admission valve (MGAV), electronic gas admission valve (EGAV), and pipeline gas admission valve (PLGAV). As the trapped air/fuel ratio increases the number of misfires increases. PLGAV improves the mixing process and reduces the number of misfires at a given air/fuel ratio.

The increased frequency of misfires also means more fuel is required, Figure 4, to attain the same power output, increasing BSFC [11][12]. The goal of field engine cylinder deactivation is to avoid these negative consequences associated with low load by having each cylinder run as close to 100% load as possible.

There are two different approaches to cylinder deactivation, which are to block the fuel supply to the desired cylinders or remove the cylinder head and connecting rod. Fuel supply regulation can either be done by shutting the fuel admission valves to the cylinder or by utilizing skip-fire technology to rotate which cylinders are deactivated by dynamically regulating the fuel valves. Removing the cylinder head and connecting rods is a time intensive process but does reduce frictional losses.

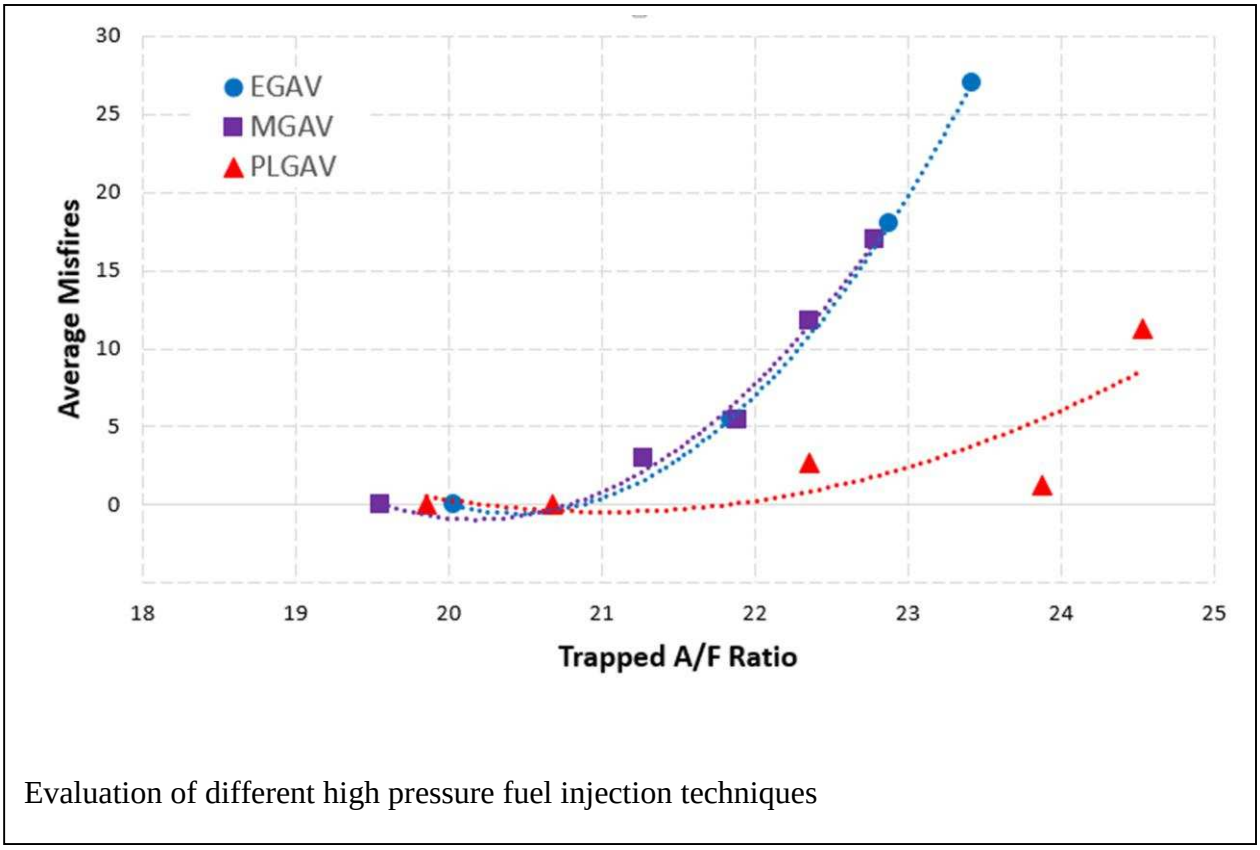

Figure 4: Average Misfires per 100 cycles vs Trapped Air Fuel Ratio [11]

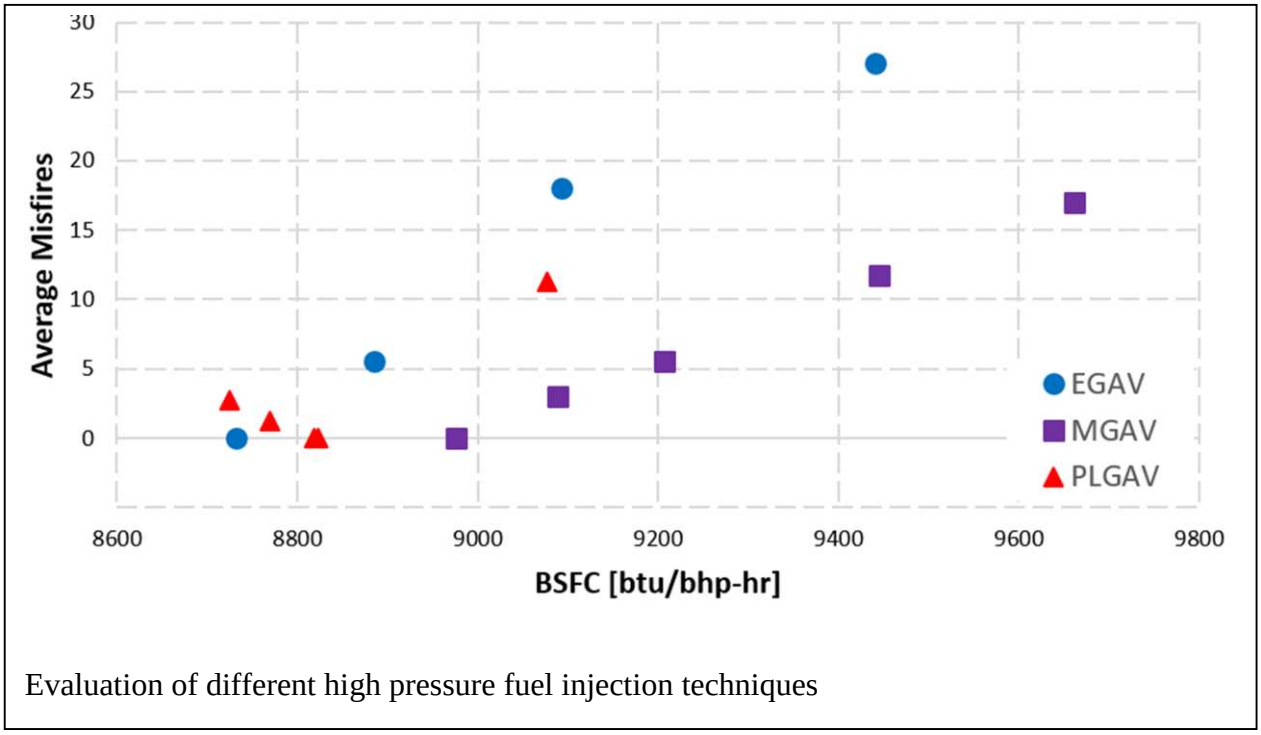

Figure 5: Average Misfires vs BSFC [11]

Smalley et al., through Southwest Research Institute, conducted a study to investigate the effects of cylinder deactivation on two-cycle engine performance [12]. The objectives were to identify any major problems with cylinder deactivation, to quantify likely benefits and any potential increases in load or stress, and to generate guidelines on the basis of project results. They conducted an industry survey to identify common problems associated with cylinder deactivation. The survey yielded that there was a decrease in BSFC between 5% and 23% under part load and a decreased propensity to misfire but there was increased incidence of spark plug fouling as well as minor accumulation of oil in exhaust manifolds. At the conclusion of the industry survey mechanical tests and analysis were conducted on a GMV-10 to create recommendations for engine operators.

A GMV-10 is a pump scavenged engine at 100% load, producing 110 bhp per cylinder at a rated speed of 300rpm, the same operating conditions of the GMVTF-4 at the EECL. Smalley evaluated 23 potential cylinder deactivation patterns on their output torque, combustion stability, and fuel consumption. The scope of the research at EECL is only concerned with the cylinder "bank" deactivation, deactivating one side of the engine. Figure 6 is a schematic of the orientation of the GMVTF-4 at the EECL, the south facing cylinders are where the cross heads are housed

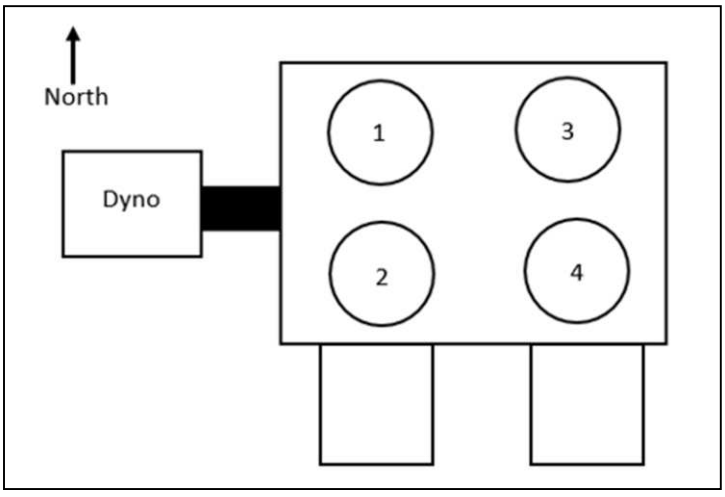

Figure 6: GMVTF-4 Orientation at the EECL

that would drive compressor cylinders if this was a field engine. A GMV-10, the engine Smalley tested, would look very similar but would have 10 power cylinders, 5 crosshead housings, and no dynamometer attached. The EECL engine banks will be referred to, hereafter, as the north (cylinders 1 and 3) or south bank (cylinder 2 and 4). Bank deactivation was the chosen method due to the cylinder firing order. All the firing cylinders are relative to cylinder 1 top dead center (TDC) at 0 degrees, cylinder 2 TDC is at 62 degrees, cylinder 3 TDC is at 180 degrees, and cylinder 4 TDC is at 242 degrees. The bank cylinders are 180 degrees out of phase, which will minimize torque and speed variations compared with other two cylinder deactivation patterns.

Smalley's evaluation of bank deactivation on the GMV-10 completed a mechanical evaluation of parameters that would cause crankshaft distress. A loading and torsional vibration model were completed to determine an annual dollar cost of risk for each arrangement. The greatest concern for cylinder deactivation was increased stresses on the crankshaft and crankcase due excitation of the crankshaft's fundamental frequencies. The GMV-10 crankshaft speeds of concern were when the natural frequency of the crankshaft intersected with the torsional frequency. The speeds of concern were 244 rpm and 279 rpm corresponding to when 8^{th} fundamental frequency intersected with the second torsional and 7^{th} fundamental frequency intersected with the first torsional, respectively. The concern was the engine speed may vary enough to excite its fundamental frequencies, increasing stresses. Smalley found that the engine running on all ten cylinders had an average speed variation of 6 rpm keeping the engine away from speeds that excite its fundamental frequencies. Smalley then conducted tests to determine the speed variation while deactivating one of the cylinder banks. The tests found both banks also had a speed variation of 6 rpm. Smalley conducted subsequent tests on bank deactivating with relaxed speed control, allowing the engine to enter its excitation frequencies. The south bank was determined to impart

a slightly greater torsional stress on the engine at 279 rpm, while at 244 rpm neither bank had an advantage. The conclusion of the bank deactivation analysis was either bank would be adequate given proper speed control was utilized.

The south bank on the GMVTF-4 has shown greater combustion stability, compared to the north bank, making it the preferred test bank to run the engine. The improved combustion stability of the south bank can be attributed to the cylinders running richer relative to the north bank, decreasing the propensity of misfires. Due to the firing order and manifold design, the north bank receives a plugging pulse before the exhaust ports close, making the in-cylinder mixture leaner [15]. The LBET is fitted with adequate speed control to ensure the engine remains close to its operational speed of 300 rpm.

Although there were four different lengths of GMV crankshafts they all had the same diameter and bearing spacing for ease of manufacturing [16]. Due to the similarity of the crankshafts it could be assumed that the relative stiffness of each section would be similar but the mass of the crankshaft would decrease for the smaller models. Following this logic, the GMVTF-4's fundamental frequencies should be greater relative to a GMV-10. Equation 1 demonstrates the concepts of fundamental frequency, used by Smalley, as being dependent upon stiffness and mass

$$f_n = \frac{1}{2\pi} * \sqrt{\frac{k}{m}}$$

Equation 1: Simplified Fundamental Frequency

of an object. A published paper could not be found identifying the fundamental frequencies of a GMV-4 but a torsional study was completed by Cooper Bessemer Applied Mechanics group, on a GMV-6; the study found that the 8th and 9th fundamental frequencies were 343 rpm and 305 rpm respectively, demonstrating the effectiveness of the aforementioned assumption [17]. If there is a

fundamental frequency within a 10 rpm range of the nominal operating speed of 300 rpm the frequencies would be of the 9^{th} or 10^{th} order, having minimal increase on crankshaft torsional stresses.

On the LBET, the north bank cylinders can either be left in the engine or removed to reduce frictional losses. Smalley's experiments found that leaving the cylinder "dead" cylinders in the engine reduced the total output of the engine to 40% of maximum load, but removing the "dead" cylinder, would theoretically allow the engine to operate at 50% of maximum load. At the current rating the GMVTF-4, BMEP ~67 psi, operating on two cylinder would produce ~180 bhp but at a GMVH-2 rating, BMEP ~125 psi, the engine could produce ~330 bhp, Equation 2. If the deactivated cylinders were removed the frictional losses would reduce, increasing the power output to ~220 bhp and ~410 bhp for GMVTF-2 and GMVH-2 configurations, respectively.

Either option would be viable at the EECL but there are concerns to both methods.

$$\frac{GMVH_{BMEP}}{GMVTF_{BMEP}} = \frac{125psi}{67psi} = 1.86 \qquad BMEP = \frac{\dot{w}_{brake}}{\frac{rpm}{60} * Vol_{disp}}$$

Equation 2: BMEP Ratio and Calculation

Smalley's survey polled industry users of large bore two stroke compressor engines like the GMVTF on their experience with cylinder deactivation. The users polled in the survey did not remove the power cylinders, like Smalley's experiments. The only problems reported with cylinder deactivation was spark plug fouling in the deactivated power cylinders and oil accumulation in the exhaust manifold. Smalley classifies these concerns as minor but noted they should not be neglected to ensure the safe operation of the engine. Typically the LBET runs less than 15 days a year allowing for the regular inspection of the engine without effecting operational deadlines.

Jackson et al. completed a similar investigation as Smalley but on a 4-stroke White Superior V-16 engine [10]. The engine's load requirements dropped below 50% of its rated power and was running inefficiently. Jackson's investigation determined the engine as an ideal candidate for cylinder deactivation to improve combustion stability. The cylinder deactivation was completed in two phases. First, eight of the engine's cylinders were deactivated by removing the push rods to an entire bank. This prevented the intake and exhaust valves from opening and was thought to have less frictional losses than to have the valves remain open [10]. The engine ran for three months in this configuration to determine if running "dead" cylinders was detrimental to engine performance. Other than the expected frictional losses the "dead" cylinders did not affect the engine performance; the cylinders had normal wear patterns on the liners, pistons, rings, valves, and cylinder heads without any excessive oxidation. The engine could be run in this configuration indefinitely but the frictional losses were detrimental to the total brake specific fuel consumption.

Jackson moved forward with the deactivation experiment to reduce the frictional losses by removing the "dead" cylinders. To complete this task, the pistons, cylinder heads, connecting rods, and valve push rods were removed, the oil admission holes were plugged to maintain engine oil pressure, and the exhaust manifold openings were sealed with a steal plate. Jackson then completed an in depth torsional analysis of the now modified crankshaft. By removing the cylinder heads and connecting rods the concentrated inertia of each of the eight crank assemblies was reduced by 22.5%. The reduction in inertia resulted in the node one fundamental frequency to increase by 7.5%. It was noted that the multiple node frequencies also increased but had very limited effect on the stresses measured on the crank case and bearings. The bank deactivation BSFC savings increased from 12% to 25% when the power cylinders were removed, reducing the frictional losses. In addition to the improved BSFC the engine was also noted to have less misfire events as

well as reduced spark plug fouling associated with the improved combustion stability of running the engine near 100% load per cylinder.

Cylinder bank deactivation will be viable for the GMVTF-4 at the EECL. The north cylinders will be the ideal bank to deactivate due to the increased combustion stability of the south bank. The engine will be able to run with "dead" cylinders or conduct a similar cylinder removal project as Jackson. If the cylinders are not removed regular engine inspection should be completed to ensure that oil is not accumulating in the manifold or in the "dead" cylinders. To address the speed and torque variation concern identified by Smalley, a tight speed control should be implemented to keep speed fluctuations within 10 rpm of 300 rpm. This method will allow the lab to move between two and four cylinder operation with ease, which will depend upon the industry sponsor's desire. Removing the cylinders from the north bank would be a time intensive project and would require additional analysis. An in depth torsional analysis would be beneficial to determine if a significant fundamental frequency would be within the operational range of the engine. Additional investigation would also have to be considered on how to manage the airflow through the engine, because a two stroke engine like the GMV does not utilize valves like a 4-stroke.

1.2.3 Engine Uprate

The domestic natural gas supply is estimated to have over 348 trillion cubic feet of natural gas [18]. The collection and distribution of this vast supply has steadily increased over the past century, as shown in Figure 7. To meet the ever increasing market demand the U.S. pipeline network has continued to expand, installing new high speed compressor engines as well as uprating the old slow speed integral compressors. The purchase and installation of new high speed compressor engines to meet the increased demands can cost upwards of $16 million per engine [5]. In contrast,

uprating a comparable existing integral compressor can cost between $5 and $10 million, representing massive savings potential for engine operators [5].

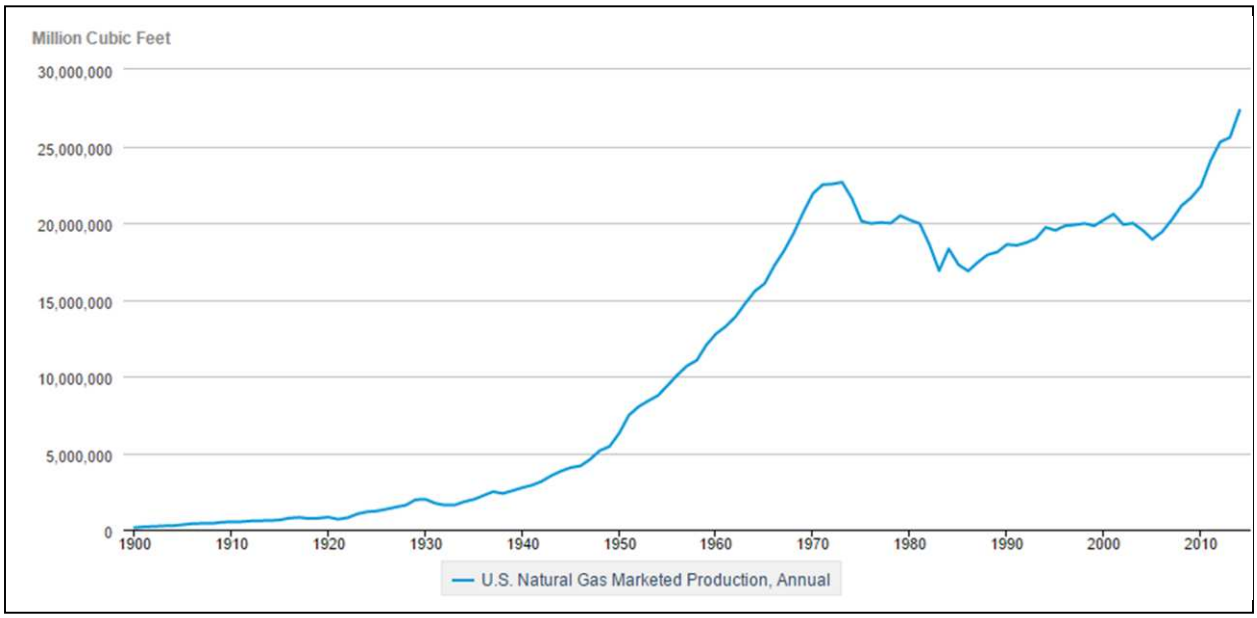

Figure 7: U.S. Yearly Natural Gas Production [1]

There are two main methods for increasing an engine's power: increasing the operational speed, revolutions per minute, or the implementation of elevated forced air induction to increase the brake mean effective pressure. Increasing the operational speed of an engine increases the power due the relationship between torque, engine speed and power, illustrated in Equation 3. The combustion force, torque, of each combustion event, in a steady state engine, is relatively constant; but by increasing the operational speed, the frequency of combustion events increases, elevating the total power output. Although increasing the speed of an engine does increase the net power

$$Power\ (bhp) = \frac{Torque\ (ft \cdot lbf) \cdot Speed\left(\frac{rev}{min}\right)}{5252\left(\frac{\frac{ft \cdot lbf}{min}}{\frac{2\pi\ (rad)}{rev}}\right)}$$

Equation 3: Horsepower Equation

output, it does not increase the BMEP. The brake mean effective pressure calculation normalizes

an engine's power by its displacement and operational speed, allowing for a one to one comparison of single combustion events between engines. To increase the BMEP, the power of each combustion event must be increased. Increasing the amount of in-cylinder air, increases the amount of available oxygen. The additional in-cylinder oxygen means more fuel can be combusted while maintaining a constant air to fuel ratio. The elevated fuel density increases the amount of potential chemical energy for the cylinder to use per combustion event. This corresponds to higher in-cylinder pressures, increasing the work per combustion event.

A standard GMVTF was a pump scavenged engine running at 300 rpm with a peak combustion pressure of ~500psi; while a GMVH was turbocharged, running at 330 rpm with a peak combustion pressure of ~900 psi [8]. The concern with uprating the GMVTF is that the increased operational stresses may cause premature failure of the crankshaft or the crankcase. To address these concerns analyses of engine materials and stresses associated with combustion and engine speed were performed.

The GMVTF-4 at the EECL was constructed at the Cooper foundry in the Mount Vernon foundry. The GMV ran using a high strength steel crankshaft. During Smalley's cylinder deactivation investigation an in depth strength analysis was conducted on the GMV's crank shaft. The crank shafts were mass produced at the Mount Vernon facility with a "generous diameter to length ratio" giving the crankshaft extreme ruggedness and resistance to torsional stresses [16]. The crank shaft is supported by two main bearings between each crank throw and an end bearing on each end resulting in comparatively low bearing pressures. Despite its 12 inch diameter Smalley suggested to avoid premature failure the torsional stresses should remain below 8 ksi on the crankshaft [12].

Unlike many engines of its time period, the GMV crankcase was cast out of a meehanite iron rather than typical gray iron [16]. Meehanite is a trademark for an engineering process for making a range of cast irons produced under carefully controlled and precise conditions [19]. Exceptional strength and wear resistance of meehanite can be attributed to its close grained, uniform matrix [16][19]. The literature did not specify the grade of meehanite the crankcase was cast out of but there are three broad types: high duty flake iron (gray iron), high duty nodular iron (ductile iron), and a specialized group designed for heat, wear, and corrosion resistance. As the meehanite process is trademarked the grade names are consistent regardless of manufacturer. Courtesy of Meehanite Metal Corporation in Mequon Wisconsin a metal selection guide was acquired, Appendix A. Upon investigation of the selection guide the possible crankcase materials were narrowed down to "G" and "S" series meehanite. The "G" series is a flake graphite iron known for good impact strength, shock resistance, and machinability as well as responding well to heat treatment. The "G" series iron have fatigue strengths ranging from 11 to 30 ksi; compared to standard gray iron with fatigue strengths between 8 and 10 ksi [19][20]. The "S" series is a nodular graphite iron with primarily a pearlitic matrix known for its high strength and machinability, resulting in fatigue strengths between 30 and 53 ksi [19]. The engineering department at Colorado State University has technology to measure the hardness and tensile strength of material samples as well as the ability to polish, etch and image samples to determine material properties.

Reynolds French is a service company specializing in repair of cracked and damaged engine casting. Many GMV castings were repaired by Reynolds French, and they outline the most common repairs in their GMV repair brochure, Appendix B. Many of their GMV repairs were replacing worn pieces of the engines and re-alignment projects but they have completed several crankcase repair projects. GMV series engines have a common crankcase design and Reynolds

French has noted that as the horsepower was increased through the use of turbochargers, the breakage was consistently found along the upper web of the engine, depicted in Figure 8. The crankcase failures begin as small cracks but if not repaired the crack can propagate through the

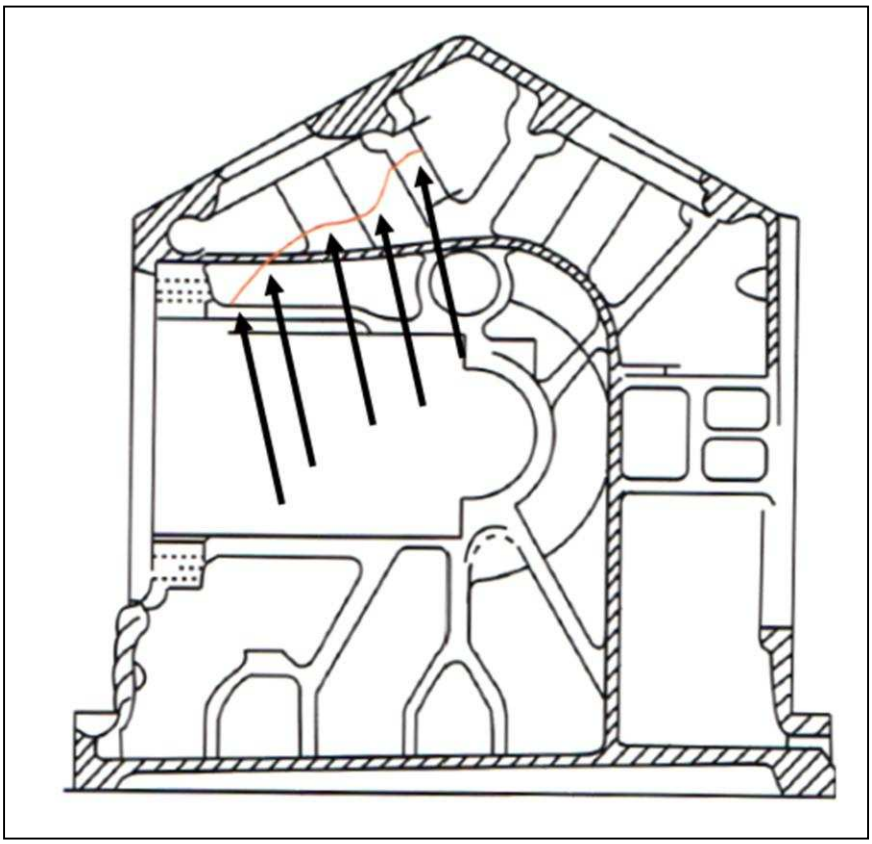

Figure 8: Common Crankcase Failure Noted by Reynolds French [35]

web resulting in catastrophic engine failure. Figure 9 shows an extensive repair of a propagating crack in a GMV crankcase. To avoid costly repairs and failure, Reynolds French suggests conducting annual crankcase inspection to insure the integrity of the engine.

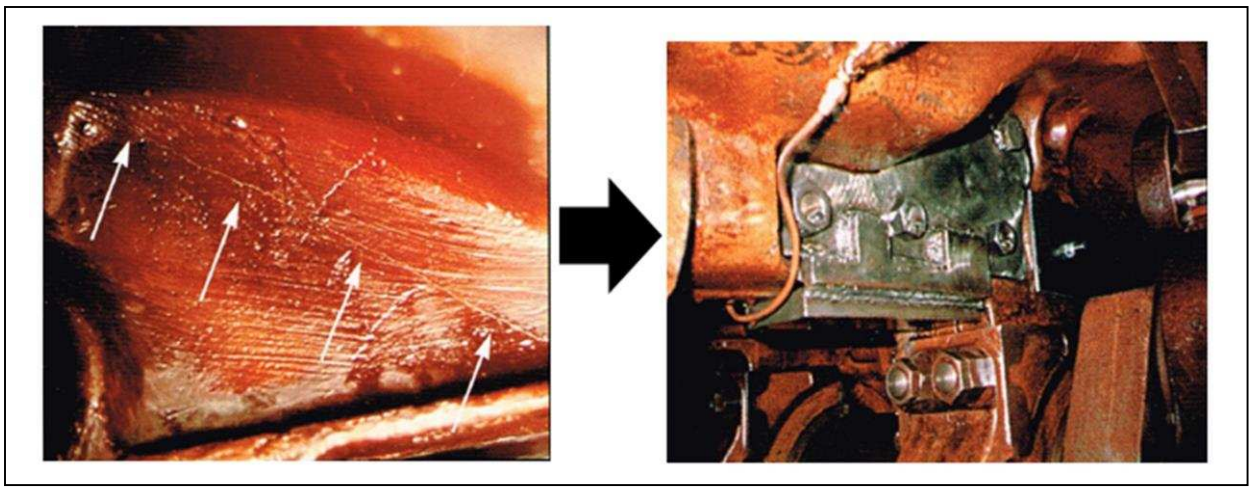

Figure 9: GMV Crankcase Crack Identification and Repair [35]

Dennis Schmitt conducted an investigation on the uprate technology development for pipeline compressor engines. The majority of his research was focused on the Clark TLA-6 but he also conducted a crankcase strength analysis on the GMVTF-4 at the EECL. Schmitt used a combination of modelling techniques to predict the forces and responses associated with the GMV's operation. He later evaluated his findings by taking on-engine measurements.

S chmitt created a simplified three dimensional model of the GMV crankcase and determined the areas of greatest stress were above and below the main bearing in the GMV [21]. The areas of high stress were determined as the points of interest where strain gauges would be mounted inside the crankcase, Figure 10. Schmitt's model did not identify the upper webs as an area of concern, as noted by Reynolds French. Moving forward, the bearing and upper web stress should be monitored to ensure the safe operation of the GMVTF under uprated operation. An in depth material analysis should also be completed to determine the true strength characteristics of the crankcase to accurately predict its behavior.

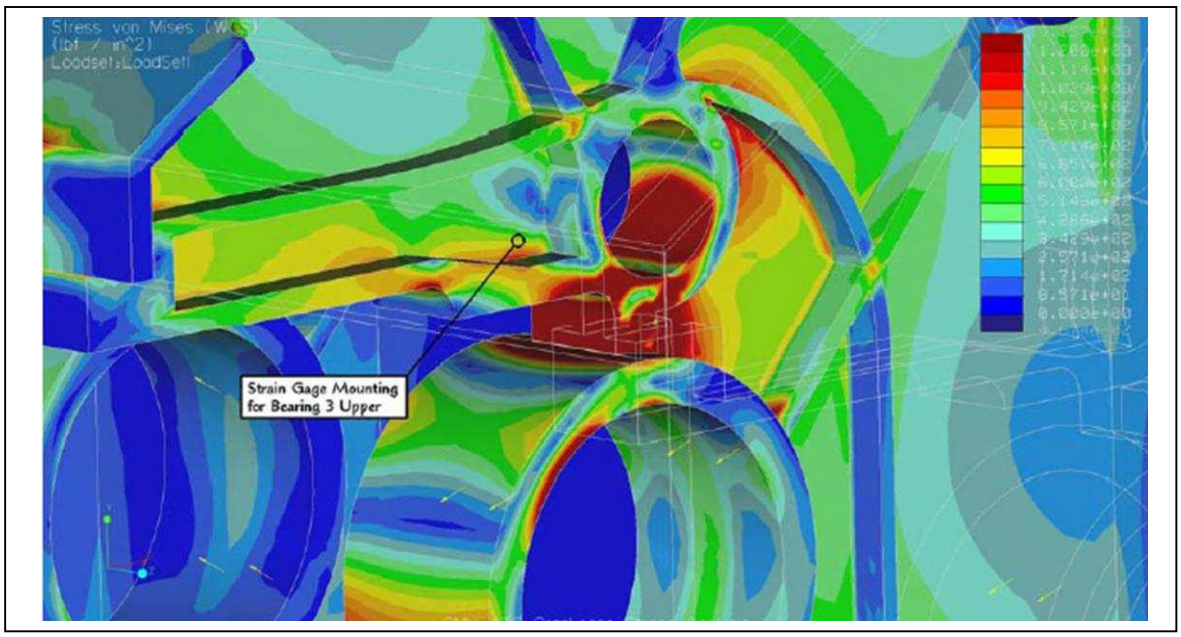

Figure 10: High Stress FEA Results [21]

Although the GMV's crankcase was cast from meehanite iron an in-depth material analysis should be completed to determine its strength characteristics. Once the grade of meehanite is determined, development of a three dimensional model will be needed to identify the regions of high stress. The use of Schmitt's force data will be used to predict the input forces on the crankcase. Like Schmitt, the new model will be used to identify the regions of high stress and identify any concerns. The findings will then be evaluated to determine if the GMVTF-4 can be safely converted into a GMVH-2.

1.2.4 Finite Element Analysis Background

Finite Element Analysis (FEA) is a numerical technique to find approximate solutions by subdividing a large problem into several smaller parts consisting of nodes and elements. FEA was originally developed for stress analysis of aircraft structures but has grown with the advancement in computing technology to many diverse applications in the engineering field [22] [23] [24] [25]. The most common applications for FEA are structural analysis, mechanical design analysis, electromagnetics, heat transfer, fluid mechanics, and biomechanics [25]. Within each application

there are different types of analysis but equilibrium is the most common when analyzing structural mechanics [25].

FEA is a very powerful engineering tool but the user must understand it is not an exact solution. This method uses numerical approximations and is not composed of closed form analytical equations [22]. Conducting stress analysis, the FEA numerical methods will discretize the three dimensional model into many "finite elements" and solve for an equilibrium, determined by the spatial distribution of the forces, shown in Figure 12. The numerical methods approximation are defined at the boundaries of each element, or nodes. Once the boundary nodes are determined, the internal nodes are approximated using interpolation equations.

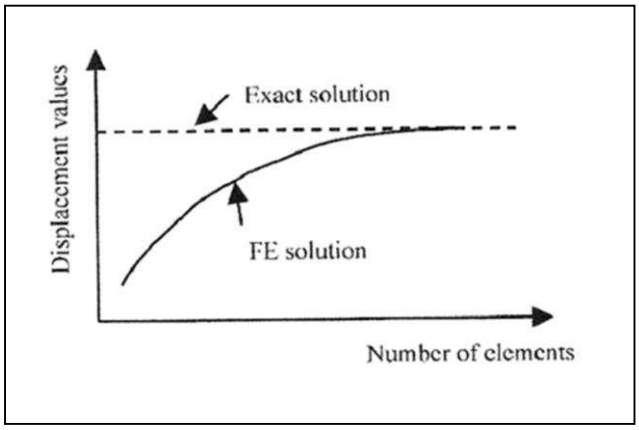

Figure 11: FEA Solution Approximation [27]

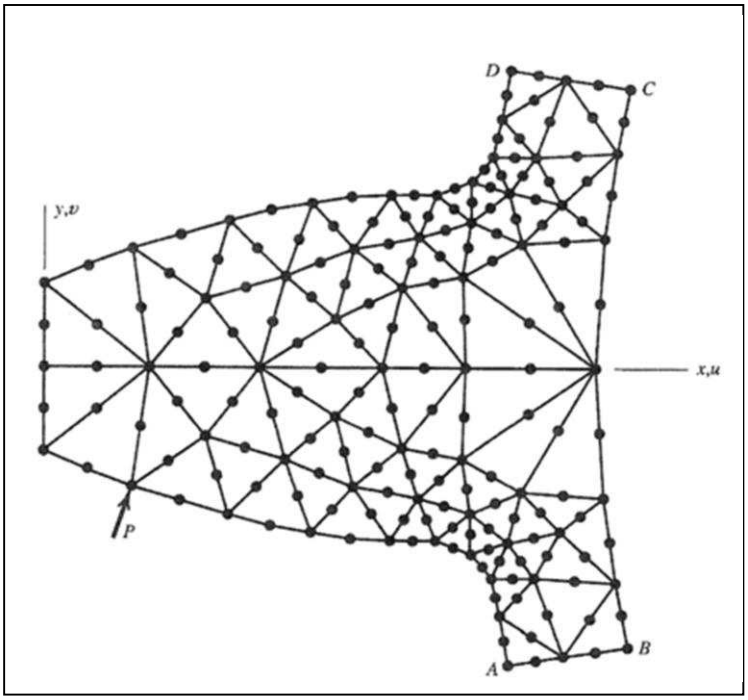

Figure 12: Two Dimensional Geometry Discretized into Finite Elements [26]

Although FEA is an approximate numerical solution the accuracy of the model can often be improved by increasing the number of finite elements representing the geometry. By increasing the number of finite the elements the accuracy of the model does increase. But the cost of the greater accuracy has a point of diminishing return where the significantly more computing power does not warrant the additional elements, illustrated in Figure 11.

FEA allows the user to predict the behavior of very complex geometries. Complex geometries cannot be analyzed using closed form solutions and using numerical methods would lead to drastic simplification of the part. FEA allows a user to analyze these geometries but the user must determine the validity of the generated results. One key process for FEA, the user must conduct a "reality check" do determine if the results are reasonable. To determine whether the results are reasonable the user can evaluate a closed form solution to verify the model findings [22] [26] [26] [27]. Closed form solutions and on sample measurement allows the user to calibrate the FEA

models. Once the model is calibrated the user can extrapolate and explore theoretical test cases. A process map for validating the FEA measurements is outlined in Figure 13.

The improvement of solid modelling is an iterative process that leads to many revisions of the model to obtain an accurate representation of the specimen.

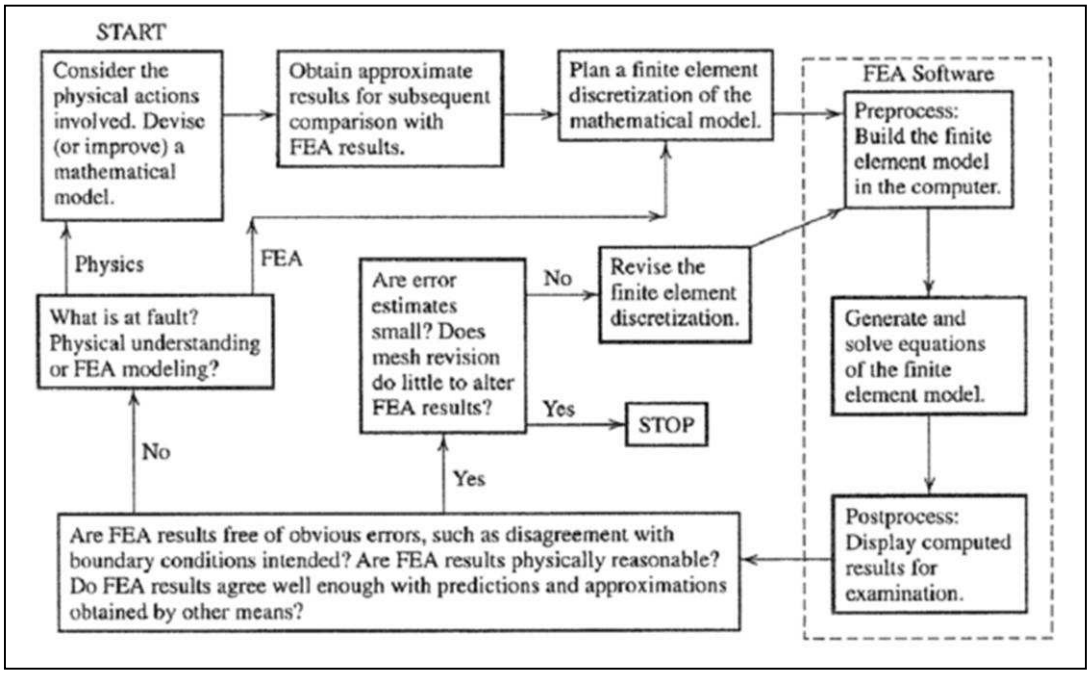

Figure 13: FEA Validation Process Map [24]

2 CRANKCASE MATERIAL DETERMINATION

2.1 OVERVIEW

There are two main categories of material testing, non-destructive and destructive. Due to the engine's size and location the techniques to evaluate the crankcase properties would have to be brought to EECL or samples would need to be removed and evaluated. Removing small samples from the engine was chosen due to cost constraints and the increased flexibility to take the samples to multiple labs. Non-destructive tests were favorable because it allowed each sample to be tested for multiple properties but unfortunately some properties could only be determined using destructive means.

2.2 MATERIAL ANALYSIS METHODS

To determine the specific grade of meehanite, the metal selection guide in Appendix A provided a guideline for the material properties to be analyzed. The material properties of interest were the graphitic microstructures, hardness, density, tensile/fatigue strength, and modulus. The literature review narrowed down the potential material candidates to "G" and "S" grades of meehanite with flake and nodular graphite microstructures, respectively. A common metallographic technique for determination of a sample's microstructure is the process of grinding, polishing, etching and imaging using an optical microscope. The grinding process roughly shapes the sample to a manageable size and to a flat and uniform finish. The polishing phase is a precise form of grinding, smoothing the surface to a mirror finish, often a smoothness of one micron [28] [29]. The use of etchants helps expose grain boundaries, highlights the metallic phase, and exposes the general microstructure. Varder Voort suggests using a nital solution with a concentration

between a 2% to 6%, to etch the sample[29]. Nital is a mixture of nitric acid and alcohol. The etchant works because nitric acid has a strong oxidation response to ferritic metals, enhancing the imaging of the material microstructure. The polished and etched sample must be handled with care to ensure no surface contamination or damage before imaging. An optical microscope is adequate for the determination of the type of graphic structure present on the meehanite samples. The Advanced Materials Processing and Testing Lab (AMPT) at the Motor Sport Research Center (MERC) run by Dr. Troy Holland has the ability to process the material samples to determine the microstructure. The AMPT also has the capability to conduct precise density calculations using Archimedes' method.

Once the microstructure and density is determined, hardness testing can further narrow potential candidates. The Smash Lab at CSU, managed by Joe Wilmetti, has the ability to conduct Rockwell B hardness testing using a 1/16 inch ball indenter. The lab has the ability to take multiple hardness samples and then to average the data to ensure an accurate hardness was determined. The determination of the microstructure, hardness, and density are non-destructive tests allowing a single sample to be used multiple times to determine the properties.

The determination of tensile strength and modulus of a sample requires stressing the sample until failure, which is destructive testing. A common method to determine the ultimate tensile strength of a material is to machine it into a dogbone, as specified in ASTM E8 [30]. The dogbone sample can either be cylindrical or rectangular. The CSU Smash lab has various sizes of tensile testing machines able to accommodate the "standard" sizes of ASTM dogbone samples. The tensile testing machines in the Smash Lab are equipped with hydraulic wedge style grips that are only capable of holding rectangular dogbone samples. To test "sub-sized" dogbone samples the

construction of a specialized jaw adapter would be required to ensure the material does not slip out of the jaw assembly.

Dogbone samples are designed to be easily held and manipulated by tensile testing machines with the "reduced section" as the designed point of failure, seen in Figure 14. To ensure the failure occurs in the reduced section the radius between the shoulder and the reduced section are designed to minimize stress concentration and have the failure occur in the known area of the reduced section [30]. The surface of the sample should also be smooth to further reduce stress concentrations.

The MTS tensile testing machines are interfaced with a data acquisition and control system to measure and regulate the jaw speed and applied force. The system has the ability to record the applied force and relative displacement of the jaws once the test has commenced. In conjunction with the MTS software, an extensometer should be used to accurately measure the change in length of the gauge area. The extensometer is used to accurately measure the strain of the sample. The software is capable to measure the total displacement of the machine sample but this method is inadequate to determine the sample strain. ASTM E8 strongly advised against using the total sample displacement for modulus calculation [30].

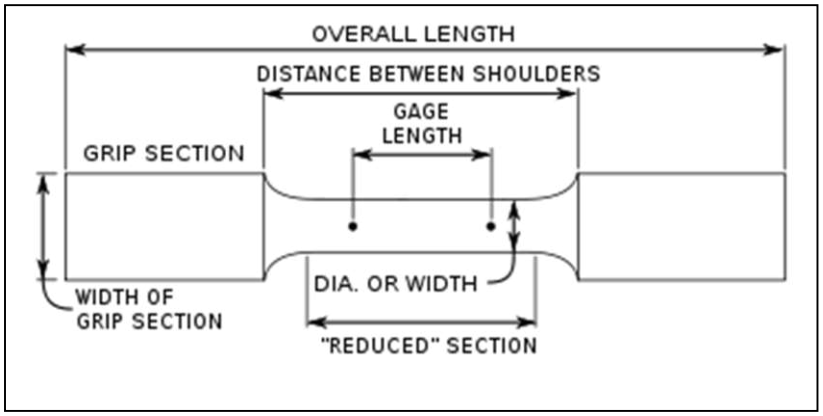

Figure 14: ASTM E8 Dogbone for Tensile Test [30]

Prior to pulling the test piece the dimensions of the dogbone must be measured and recorded to properly calculate the stress and strain. The important characteristics to measure are the gauge length and the cross sectional area of the gauge length.

To calculate the modulus the stress and the strain of the sample must be determined [31]. The force, for the stress calculation, is measured from the MTS load cells in conjunction with displacement of the system and the extensometer at a rate of ~2.5kHz. The gauge length and area is measured before the test using precise engineering calipers to determine the cross section area (A_{gauge}) and the original length ($L_{o\text{-}gauge}$), Equation 6a and Equation 6b. The data is then used to create an engineering stress-strain curve, like the curve shown in Figure 15. An engineering stress strain curve does not take into account the necking, shrinking area of the gauge section of the iron but is the curve used to determine engineering material properties [31]. The linear elastic region

$$\sigma[psi] = \frac{Force[lbf]}{A_{gauge}}$$

Equation 6a: Stress Calculation [31]

$$\varepsilon = \frac{L_{gauge} - L_{o-gauge}}{L_{o-gauge}}$$

Equation 6b: Strain Calculation [31]

$$E[psi] = \frac{\sigma[psi]}{\varepsilon}$$

Equation 6c: Modulus Calculation [31]

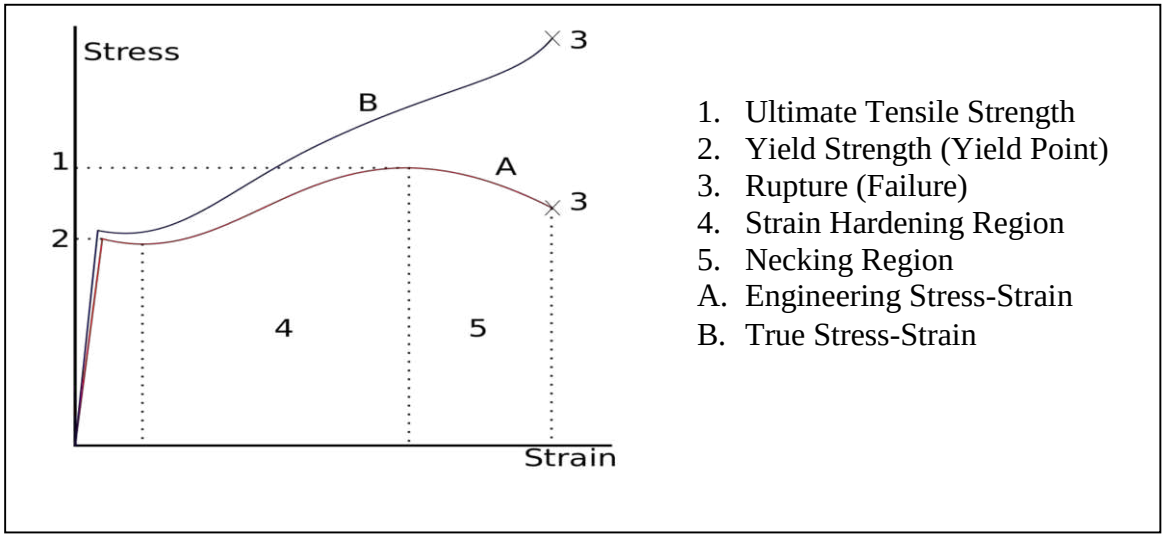

Figure 15: Engineering vs True Stress-Strain Curve [31]

of the curves, from the start of collection to the yield point, is where the modulus of elasticity is calculated. Modulus is the measure of an object's resistance to elastic deformation when force is applied. In the elastic region, the material can be deformed under load but once the load is removed the material will return to its original shape. However, past the yield point the part will be permanently or plastically deformed.

All the techniques described above were used to narrow down the likely grade of meehanite iron of which the GMV crankcase was cast.

2.3 MATERIAL TESTING

Two samples were removed from the north side of the engine under the crankcase doors, shown in Figure 16. The samples were roughly 14 inches long with a rough triangular-like cross section (Figure 17). Several non-destructive and destructive tests were conducted to determine the material properties of the meehanite crankcase. The material testing was conducted at the CSU Smash Lab and the AMPT.

Figure 16: Sample Location

Figure 17: Cross Section Slice from Sample

2.3.1 Non-Destructive Testing

Two cross sectional slices were used to determine the graphitic structure, density, and hardness of the samples. There were two possible classes of meehanite the crankcase could be cast out of, “G” series or “S” series with flake and nodular graphite structures respectively (Figure 18).

2.3.1.1 Imaging to Determine Graphitic Structure

To determine the graphitic structure of the iron a combination of grinding, polishing, etching, and imaging techniques were used at the AMPT laboratory.

The first step in the process, grinding, was crucial to have the surface of the slices as flat as possible. The process required the use of successively finer sandpaper to flatten and smooth the surface. Once the sample was relatively flat, it was mounted to the platen. The platen was a precise smoothing tool used in conjunction with a sanding wheel to give a precise flat finish seen in Figure 19 and Figure 20**.** The platen’s carbide feet resist wear themselves while the operator was able to provide steady, even pressure on the sample. The process to flatten and smooth the sample was to move the platen along the outer circle in the clockwise direction while the sanding wheel is spinning in the counter-clockwise direction, shown in Figure 21. The counter rotation technique

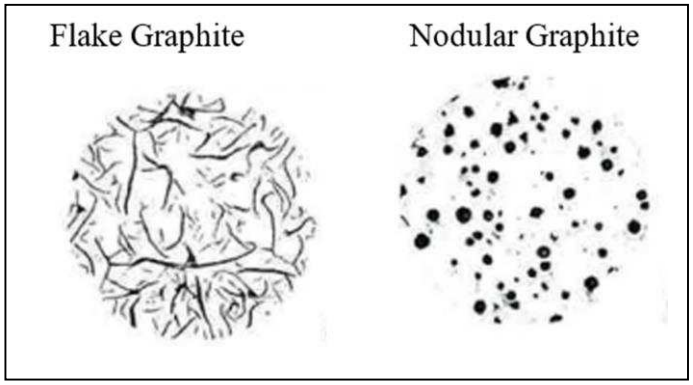

Figure 18: Flake vs Nodular Graphite in Meehanite [19]

gave the sample a smooth, even finish. The process was repeated using finer sandpaper until 800 grit sandpaper was used.

The polishing of the sample was completed in three steps: 6-micron finish followed by 3-micron finish, and finally a 1-micron finish. All the polishing steps used a specific polishing pad and a polishing media applied to the pad. The pad and media combination was essentially very fine sandpaper and the same counter rotation technique was used to attain the finishes. Once the

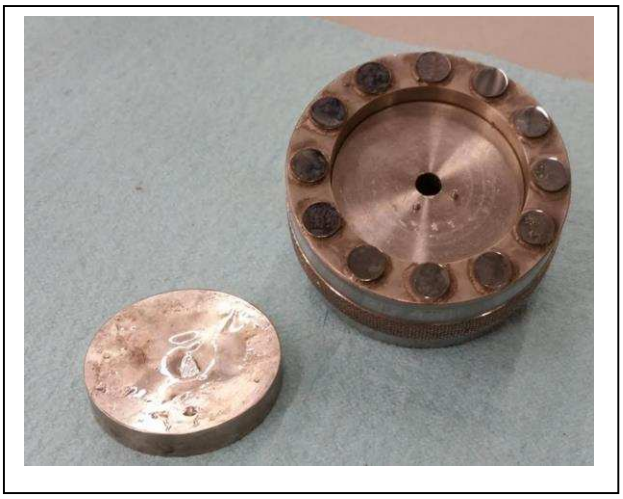

Figure 19: Platen Tool

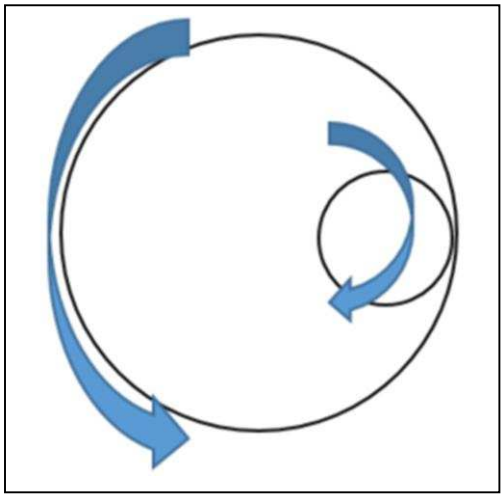

Figure 21: Counter Rotation Technique

Figure 20: Grinding and Polishing Wheel

1-micron finish was achieved the sample had a mirror finish and was ready to be removed from the platen and subsequently etched in nital.

Before the etching process, the sample was cleaned using a fine brush and non-abrasive soap to remove the polishing media. The sample was then immediately rinsed with ethanol to prevent the water from causing surface oxidation. The cleaned sample was etched by submerging it in a 4% nital solution. When the sample was removed it no longer had a mirror finish but a smooth, “grainy” appearance, seen in Figure 22. The sample was handled with care to ensure no surface blemishes were introduced so that clear images could be obtained.

The sample was imaged using an optical microscope at three magnifications: 10x, 20x, and 40x. Several images were taken of the sample at the three magnification levels. Figure 24, Figure 23, and Figure 25 were chosen as representative images to show the microstructure. Comparing the images to images from Meehanite Metal, the crankcase appears to be cast from a flake iron, or “G” grade.

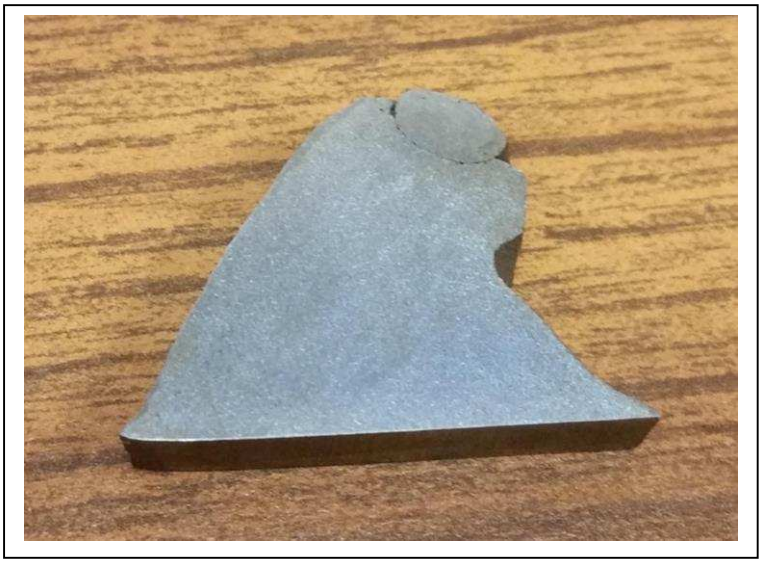

Figure 22: Etched Sample

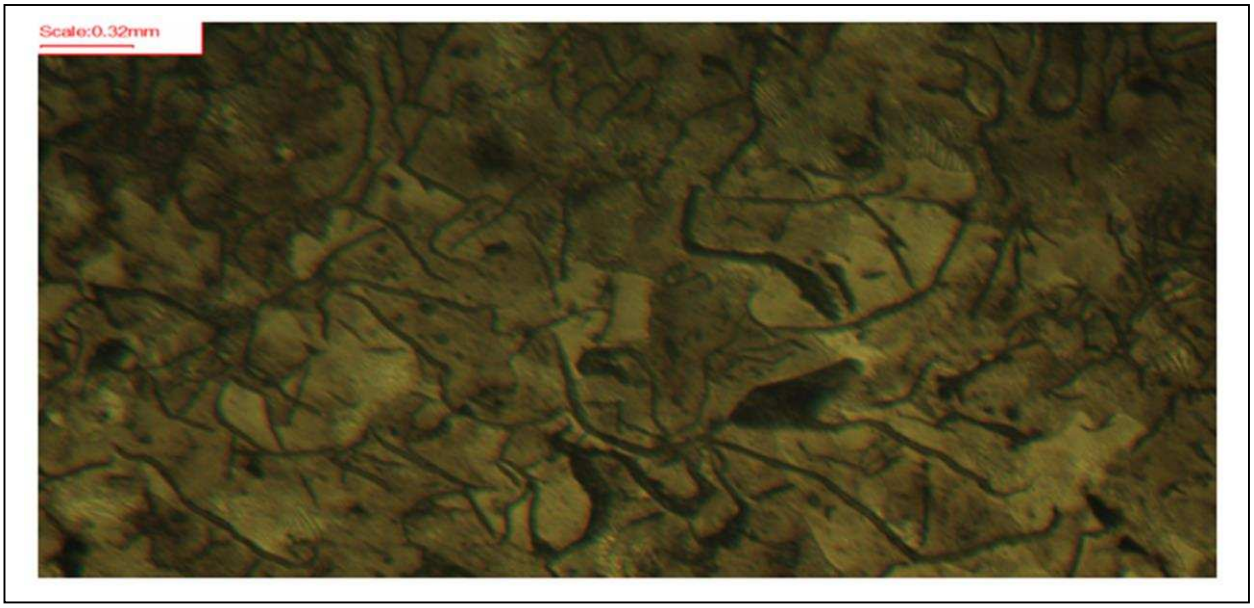

Figure 24: 10x Sample Image

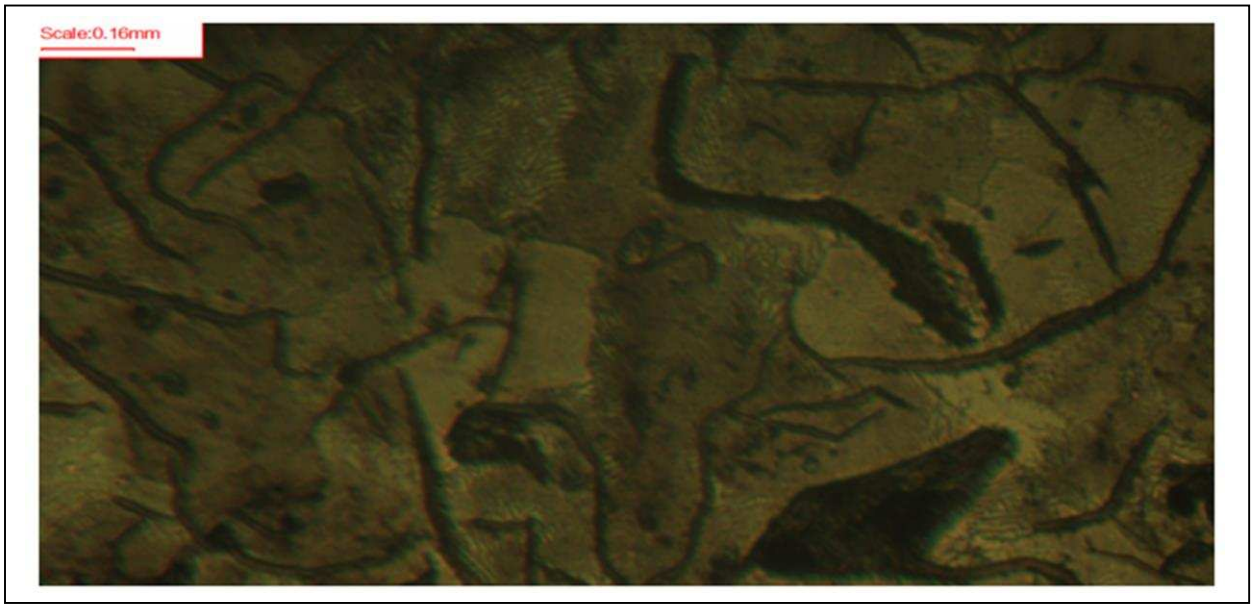

Figure 23: 20x Sample Image

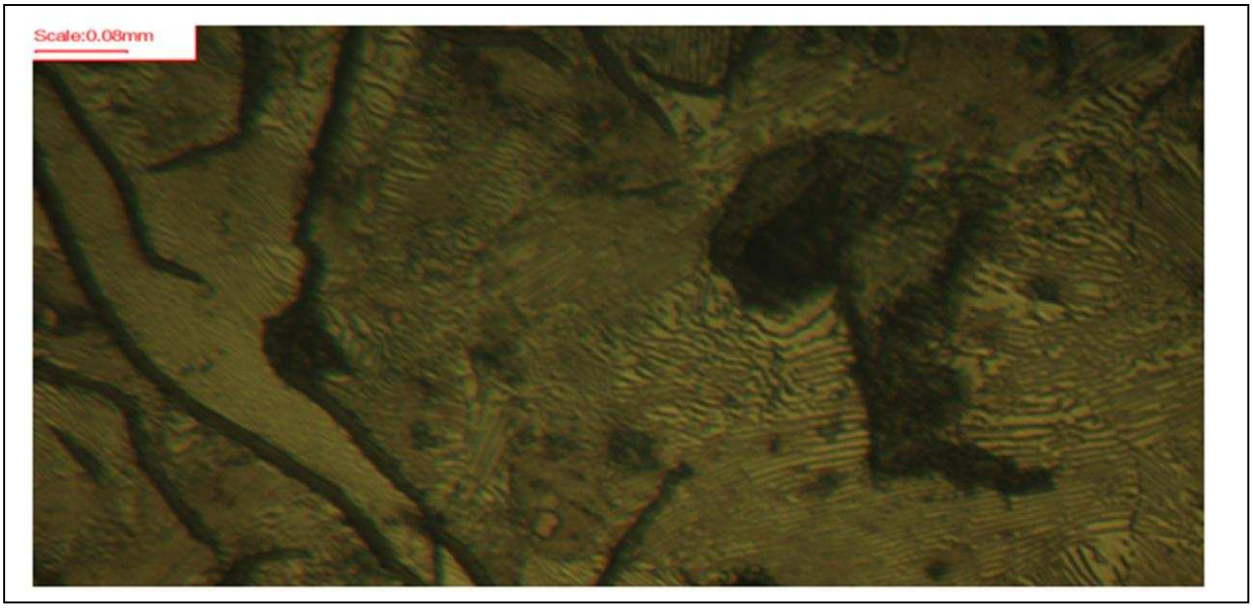

Figure 25: 40x Sample Image

2.3.1.2 Density Calculation

Density is defined as the mass per unit volume and is an important measurement for determining material properties. One particular method for determining density is to use Archimedes' principle. The basis of the Archimedes' principle is the buoyant force on a submerged object is equal to the weight of the fluid displaced. If the weight of the fluid displaced can be measured, the fluid volume displaced can be calculated and in-turn the density of the sample can be determined. Figure 26 shows a visual representation of Archimedes' principle. In the example, the sample has a weight of 7 kg when not submerged and weight of 4 kg when submerged, meaning 3 kg of water is displaced. At room temperature, water roughly has a density of 1 g/cm^3, meaning that 3,000 cm^3 of water was displaced. This would give the sample a density of 2.33 g/cm^3. This procedure was repeated to calculate the density of the GMV sample, using the equipment at the MERC.

The scale at the MERC was a RADWAG XA 110/2x capable of 7 significant figures of accuracy. Figure 27 corresponds to the left drawing in Figure 26 and Figure 28 to the right

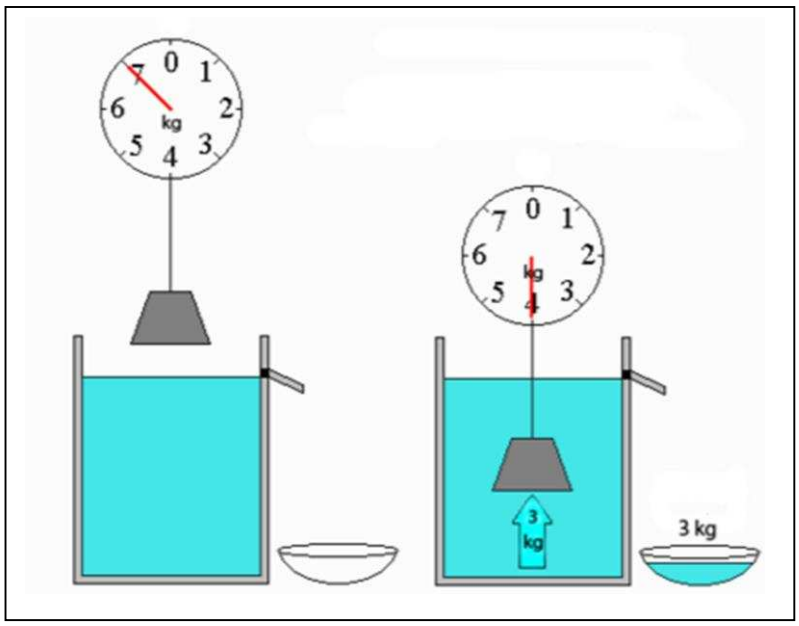

Figure 26: Archimedes' Principle Diagram

drawing. In Figure 28 the basket support system, that sample was held in, was directly connected to the load cell of the scale and the beaker was supported over the load cell. The apparatus was set up and allowed to stabilize before "zeroing" the scale, to take into account the weight and buoyancy of the basket assembly. Table 1 shows the measurements and results from the Archimedes' method.

The imaging results determined the sample was a flake graphite, limiting the grade possibilities to "G" type. Archimedes' method determined the sample's density was 7.02 g/cm^3. The determined density was close to the density of GE-30 from Meehanite metal at 7.06 g/cm^3 and the ASTM class 25 iron at 7.15 g/cm^3 [19][20][32].

Table 1: Archimedes' Density Measurement Results

Object	**Measurement**
Water Temperature	21° C
Water Density	0.9968 g/cm^3
Sample Mass	27.58253 g
Submerged Mass	23.66623 g
Mass of Water Displaced	3.92 g
Volume of Water Displaced	3.93 g
Density of Sample	7.02 g/cm^3

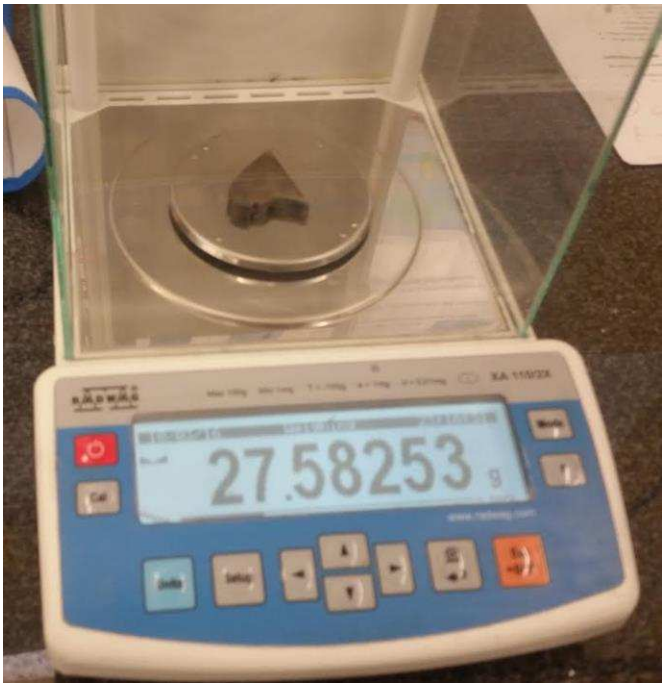

Figure 27: Measuring Sample Mass

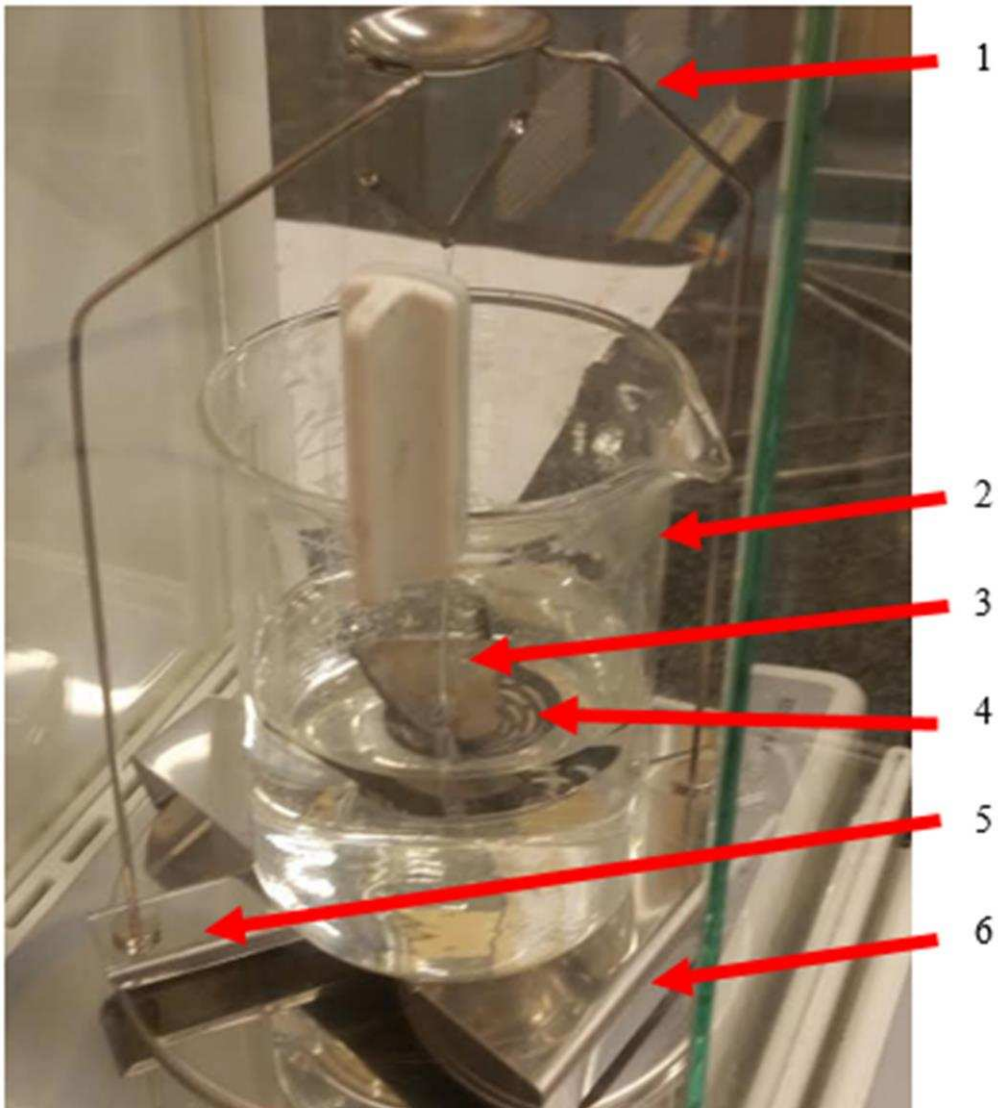

1. Basket Support
2. Beaker of Water
3. Sample
4. Sample Basket
5. Load Measurement
6. Beaker Support

Figure 28: MERC Archimedes' Scale

2.3.1.3 Hardness Testing

The ASM Handbook defines hardness as resistance of a metal to plastic deformation [33]. Hardness is a homogenous property for meehanite. To determine the hardness of a material there are various methods, but the Smash Lab at CSU has the capability to conduct Rockwell B hardness testing. The procedure for conducting Rockwell B hardness testing is defined in ASTM-E-18.

The Rockwell hardness is determined by measuring the plastic deformation of a part relative to a "zero" point [34]. The penetration depth of the indenter and the hardness are inversely proportional, shown in Equation 7. To calculate the hardness, a uniform sample is placed in the apparatus and preliminary load is applied to establish the "zero" point. The test force is then applied, for the Rockwell B test the test force in 100 kg. The force is then relaxed to the preliminary load and the depth measurement is determined, denoted as "h". The described process can be seen in Figure 30.

Equation 7: Rockwell Hardness Equation [34]

$$Rockwell\ Hardness = 130 - \frac{h}{0.002}$$

The Antonik Tester Service Rockwell hardness tester, in the CSU Smash Lab, was used to conduct multiple hardness tests on the material samples, shown in Figure 29. The average Rockwell B hardness was determined to be 92 with a standard deviation of 6. This corresponds to a Brinell hardness range of 160 to 180. This harness reported hardness from Meehanite Metal of the GC-40 grade and the GE-30 grade were hardness measurements of 180 and 160, respectively, and the ASTM class 25 iron had a reported hardness of 174 [19][20][32]. This result aligned with the density determination from the previous section.

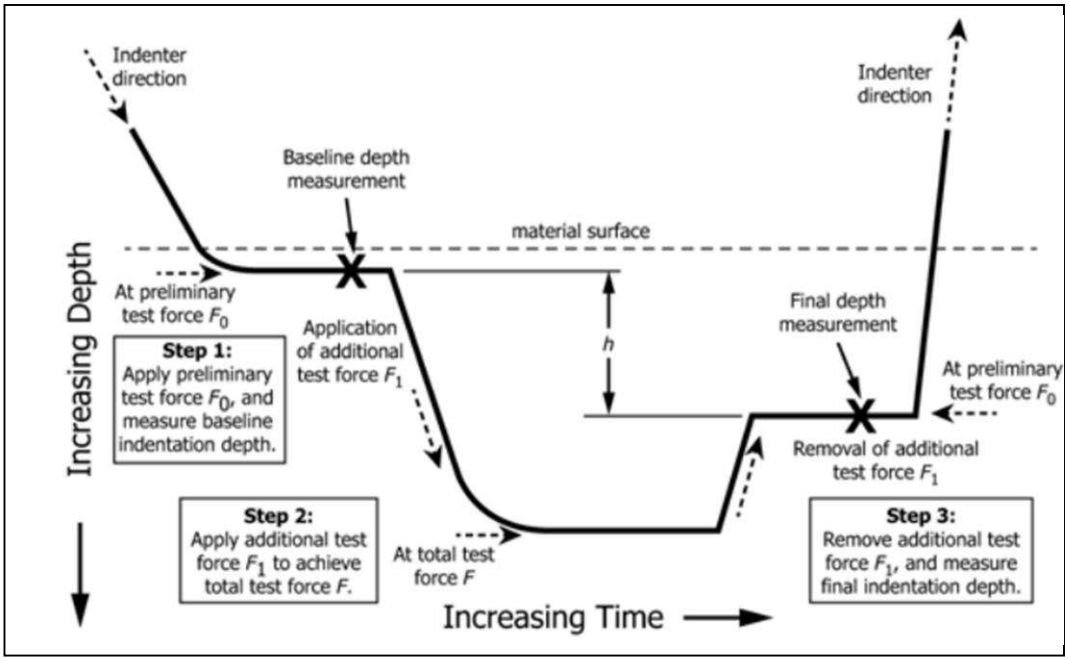

Figure 30: Rockwell Hardness Test Procedure

Figure 29: CSU Hardness Test Apparatus

2.3.2 Destructive Testing

The original large samples were cut into four smaller samples to collect more data to confirm the material properties. Recall from Figure 22 the original samples were long bars with a rough triangular cross section. To shape the sample bars into a rectangular cross section a vertical mill was used to remove one of the triangular corners as well as flatten the sample, seen in Figure 31. The large rectangular bars were subsequently cut into four smaller bars. The four smaller bars had dimensions of 3” x 1” x 0.5”. To machine the samples into dogbone samples the ASTM tensile testing was consulted to determine the proper dimensions for the specimens [30].

The code specified the samples would have a 1/8” round to neck the grip section down to the gauge length. The designed specimens had a gauge length of 1.5” with a cross sectional area of roughly 0.1875 square inches. The specified dimensions were then used to generate a tool path for a computer numerically controlled (CNC) milling machine producing four identical pieces like

Figure 31: Milling Sample into Rectangular Cross Section

that shown in Figure 32. The four samples were deburred and sanded to a 220 grit finish to remove the possibility of stress multipliers per the ASTM standard.

Due to the small size of the grip section the MTS tensile tester was not able to adequately hold the samples during the test. As a result, a set of jaw adapters was machined to hold the dogbones in the MTS jaws. The Jaw adaptors were machined out 3” x 0.5” steel stock. The stock was cut into four identical pieces of 4” in length. Like the dogbone specimens the samples were machined using a CNC mill. The final jaws with a dogbone sample can be seen in Figure 32.

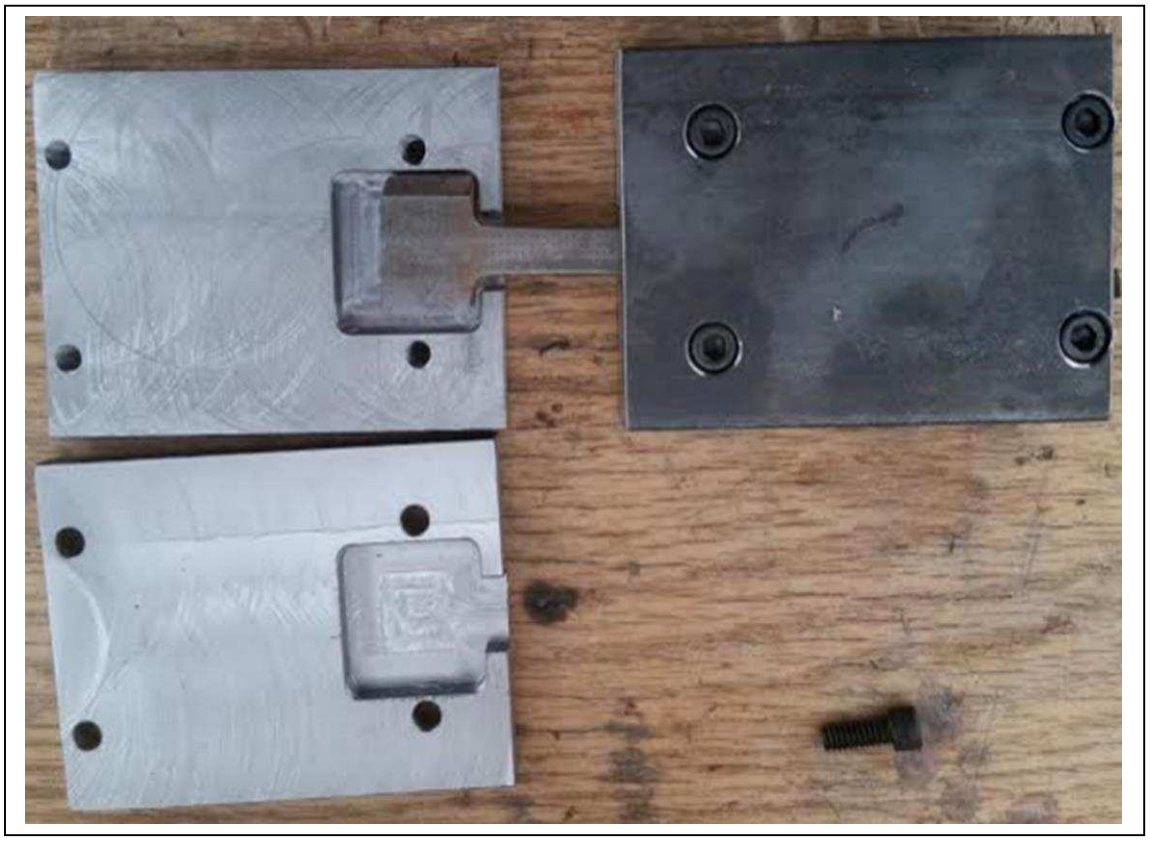

Figure 32: Micro Dogbone Sample and Jaw Adaptors

To complete the tensile testing the Smash Lab's MTS 647 apparatus was used with hydraulic wedge grips. The MTS machine was used in conjunction with an extensometer externally attached to measure the strain of the gauge section of the tensile specimens. The complete setup of the tensile testing machine can be seen in Figure 33 with extensometer seen between the grips. The entire machine is controlled by the MTS software that actuates the jaws in conjunction with collecting the force and strain data.

Figure 33: MTS Tensile Testing Apparatus with Extensometer

Prior to conducting the tensile testing each of the four sample's dimensions were measured and recorded to calculate the stress within the gauged section, shown in Table 2. The MTS software was also used to define the "pull rate" of the samples. The "pull rate" is how much displacement the machine will put on the sample per given time interval. The standard "pull rate"

Table 2: Dogbone Sample Dimensions

Sample	Height [in]	Width [in]	Cross Sectional Area [in^2]	Gauge Length [in]
1	0.481	0.383	0.184	1.498
2	0.503	0.385	0.194	1.497
3	0.503	0.383	0.193	1.500
4	0.486	0.385	0.187	1.496

for iron samples of this size is 0.04 in/min and was implemented on the system [30].

The sample was monitored by watching the real time stress strain graph generated by the MTS software. The user watches the graph to find when the sample enters the "necking" or strain hardening regime of the stress strain curve. This was when the sample was no longer behaving elastically and would be expected to fail shortly. Once the necking regime was entered the tensile test was halted. Material fracture is a very traumatic event and can damage extensometers. To protect the integrity of the instrument it was removed at this point. The test was then continued to ultimate failure. Figure 35 shows the stress strain graph from sample 3 and Figure 34 showing the fractured sample 3. Unfortunately due to the small gauge length the extensometer was not able to be directly fastened to the sample and produced inconclusive strain results. Consequently, an accurate modulus could not be determined for the tensile tests. The same technique was used for the remaining three samples with the results seen in Table 3.

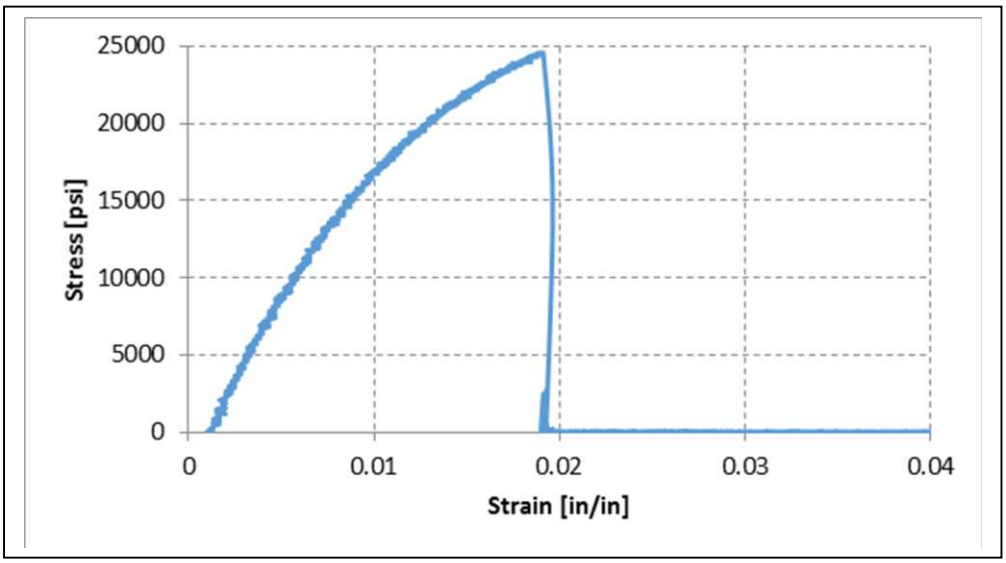

Figure 35: Stress Strain Curve from Sample 3

Figure 34: Fractured Sample 3

Table 3: Tensile Test Results

Sample	Ultimate Failure Strength [ksi]
1	24.49
2	24.89
3	24.04
4	22.55
Average	23.99

The average failure stress of the samples was determined to be ~24 ksi while GE-30 has an ultimate tensile strength of 30 ksi and ASTM grade 25 iron has an ultimate tensile strength of 26 ksi [19][20]. As can be seen in Figure 34, the sample exhibits a grey fracture surface, consistent with gray iron [32]. A fatigued sample would show beach marking in this grade of iron but the fracture surface was a brittle fracture with no cyclic loading concerns. Based on this, the engine crankcase is likely cast out of a Class 25 grade of Meehanite.

2.4 MATERIAL ANALYSIS CONCLUSION

The most likely grade of meehanite the crankcase was cast out of a class 25 meehanite. Although Meehanite metal does not currently produce a class 25 the selection guide can still provide an approximation for iron properties. ASTM cites that class 25 iron is often used for cylinder heads, as well engine blocks and housings [20].

Class 25 irons are flake graphite iron with a pearlitic matrix. This result is consistent with the findings from section 2.3.1.1. Class 25 grade had a densities of 7.15 g/cc, compared to the measured sample density of 7.02 g/cc from section 2.3.1.2, corresponding to a percent difference 1.8% [20]. The class 25 grade had a reported hardness of 174 on the Brinell hardness scale compared to the measured sample hardness range from section 2.3.1.3 of 160 to 180, encompassing the reported value. The class 25 iron had an ultimate tensile strength 26 ksi and the average failure stress of the samples was ~24 ksi corresponding to percent difference of 7%. After speaking with Joe Wilmetti, the Smash Lab manager, the MTS machine has not had a factory calibration for over 5 years, and citing Dr. John Petro's experience in material testing this could result in a 5% measured load error. This likely error could explain the discrepancy between the reported ultimate tensile strength and the measured.

The FEA software had a gray cast iron already in its material toolbox with properties between the GE-30 Meehanite and ASTM class 25 grade. This material was assumed to adequately predict the engine material properties for conducting FEA.

To determine the exact grade of iron a spectrographic analysis would be required to determine the elemental composition within the metal.

3 CRANKCASE MODEL DEVELOPMENT AND FEA TESTING

3.1 OVERVIEW

The goal of creating a three dimensional model and FEA was to identify the regions of high stress in the engine, where failure was likely to occur. A combination of past models, engineering drawings, and on engine measurements were used to develop an improved representation of the LBET. The previous FEA conducted by Schmitt only considered the force inputs at the main bearings. The enhanced computing ability of the engineering compute servers allowed for more input forces and a finer mesh analysis to be conducted, improving the model accuracy.

3.2 MODEL IMPROVEMENT

The three dimensional model of the LBET was constructed in Creo Parametric. Creo is a suite of design software supporting product design by PTC. The suite consists of several apps, each delivering a distinct set of capabilities for product development. The direct modeling and model assembly features, within Creo, were used to create a virtual three dimensional representation of the engine.

The model was constructed using a combination of past models, engineering drawings, and on engine measurements. Schmitt's simplified model provided the groundwork for the development of an accurate representation of the GMV crankcase. Schmitt constructed the simplified model of the crankcase due to computing power limitations. He noted that more complex geometries needed for a more accurate model would produce meshing errors in the FEA program [22].

The new GMV crankcase model was focused on improving the accuracy of the bearing caps, the web design, and removing artificial stress concentrations. Particular interest was given to improving the upper web accuracy, because of common premature failures noted in field engines [35]. The model improvement was an iterative process and was constantly improved after each FEA simulation to remove artificial stress concentrators due to the meshing method. Particular care was placed in the assembly and modeling of the combustion cylinders to account for the reactionary forces placed on the upper webs due to in-cylinder pressures. The improved model of the GMV can be seen in Figure 36.

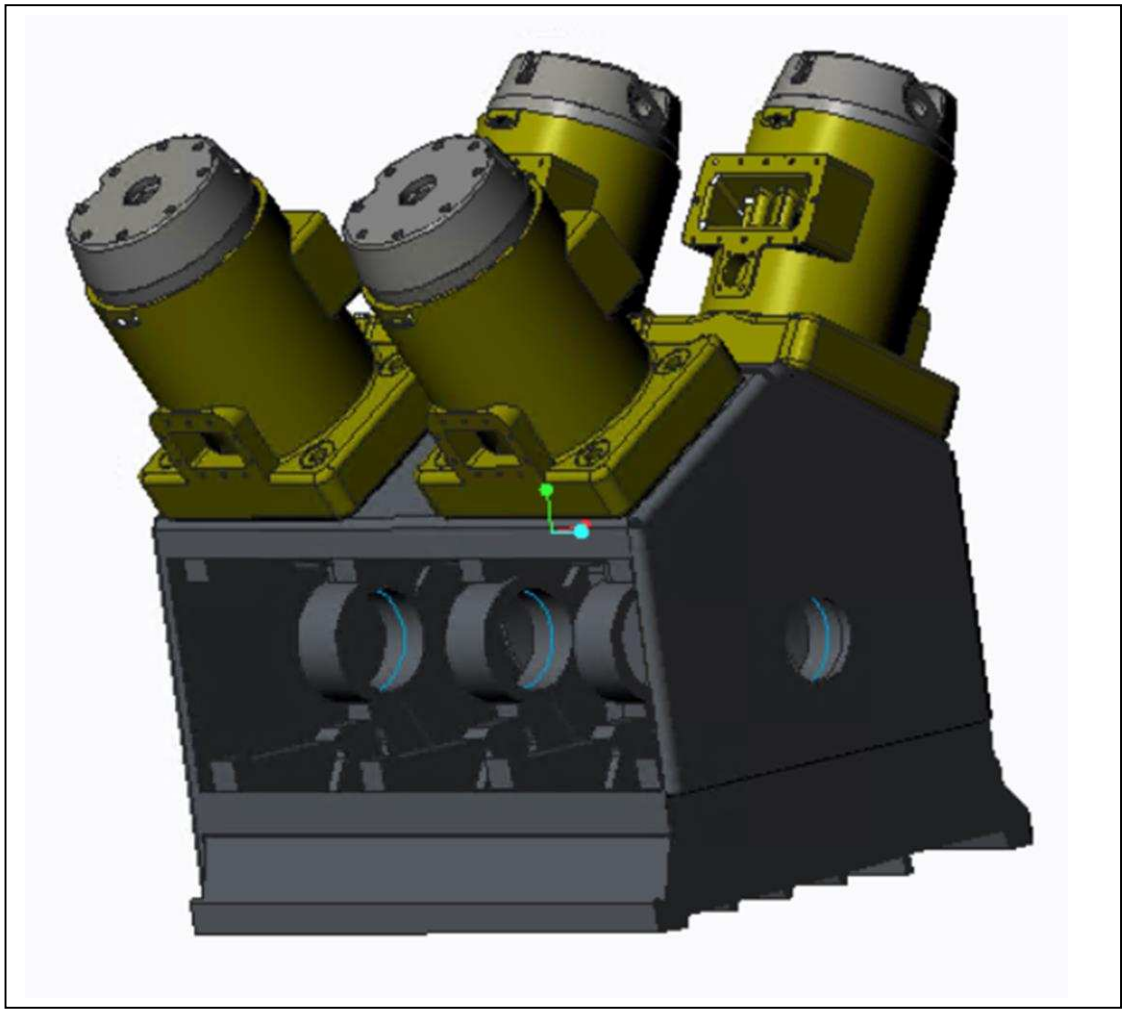

Figure 36: Improved GMVTF Crankcase Model with Power Cylinders

The model was then imported into a FEA program, Ansys Workbench, to compete an in depth structural analysis of the engine.

3.3 FEA SET UP AND RESULTS

Ansys Workbench was the software used to conduct the FEA investigation. Ansys has a wide range of capabilities but only the Mechanical toolbox was used. Ansys Mechanical toolbox is a finite element analysis tool for structural analysis. The generated model can be manipulated and improved to provide the most accurate representation of the LBET.

The findings from the material testing determined the engine crankcase was cast out of class 25 grade of meehanite. The material properties for class 25 meehanite were very similar to the existing gray cast iron already available in the Ansys toolbox but some of the values were modified to better reflect the class 25 iron. The crankcase and cylinder geometries were designated as the modified gray cast iron for all the simulation cases.

FEA modeling was conducted in three steps, pre-processing, analysis and post-processing or result interpretations.

3.3.1 Pre-Processing

The pre-processing step was where the FEA model was constructed using the three dimensional Creo model. Ansys divided the imported three dimensional geometry into a finite number of discrete sub-regions, “elements”, connected at discrete points called, “nodes” [36]. Each of the nodes will either have defined loads or a set displacement dependent upon the model assumptions. The final model consisted of 662,686 nodes and 407,582 elements. Once the mesh was generated the input forces were implemented on the model.

3.3.1.1 Bearing Forces

The articulated crank assembly of the GMV, has a complex motion that would make predicting the bearing forces very complicated using simple analytical methods. Schmitt used the software Working Model to predict the how combustion forces would be translated to the bearings. MSC Working Model was an engineering simulation software product by Design Simulation Technologies, utilizing virtual mechanical components to simulate an objects response in a two dimensional work space.

The model was constructed using test data collected from the LBET running at nominal conditions, standard mechanical gas admission valve fuel injection, and sea level manifold conditions with a boost of 7.5 inHg gauge [22]. The in cylinder pressure data were converted into the input force for the Working Model simulation with the peak pressure maintained at 18° after top dead center (ATDC) [22]. The working model simulation took into account the weights and inertial loading of the components that move and rotate, but the geometries were simplified for two dimensional representation [22]. Each of the two simulated banks consisted of the crankshaft, master connecting rod, two power piston connecting rods, two power pistons, and one cross head. The simulation also took into account the frictional losses of the entire mechanism

It was assumed the journal bearings were under normal operating conditions. The main journal bearings are fluid film bearings, where under normal conditions they were in a full hydrodynamic regime with minimal frictional losses [16]. Schmitt assumed the bearing friction was 0.01 [22]. The assumed frictional value of 0.01 was within the known friction coefficients for standard journal bears in the hydrodynamic regime [37]. The wrist bearing's coefficient of friction was assumed to be 0.05 which is within the typical range of oil lubricated iron on iron joints [37].

Schmitt also accounted for the frictional losses due to the piston rings. The GMV has dynamically lubricated steel rings and cast iron sleeves and assumed the friction between them were 0.1 [22].

Due to the limitations of the two dimensional simulation the bearing reactant forces were assumed to have zero out of plane force and were only vertical and lateral components. Appendix C has partial input and results data as well as how the Working Model simulation was organized. Figure 37 was the output results from the working model simulation used as bearing input forces in Schmitt's FEA model.

The university no longer holds a license for Working Model and resources were unavailable to purchasing software licenses for this project. The output from Schmitt's models could be used to predict the engine's stress response while running at nominal GMVTF conditions but could not be directly modified to predict the bearing forces at uprated conditions.

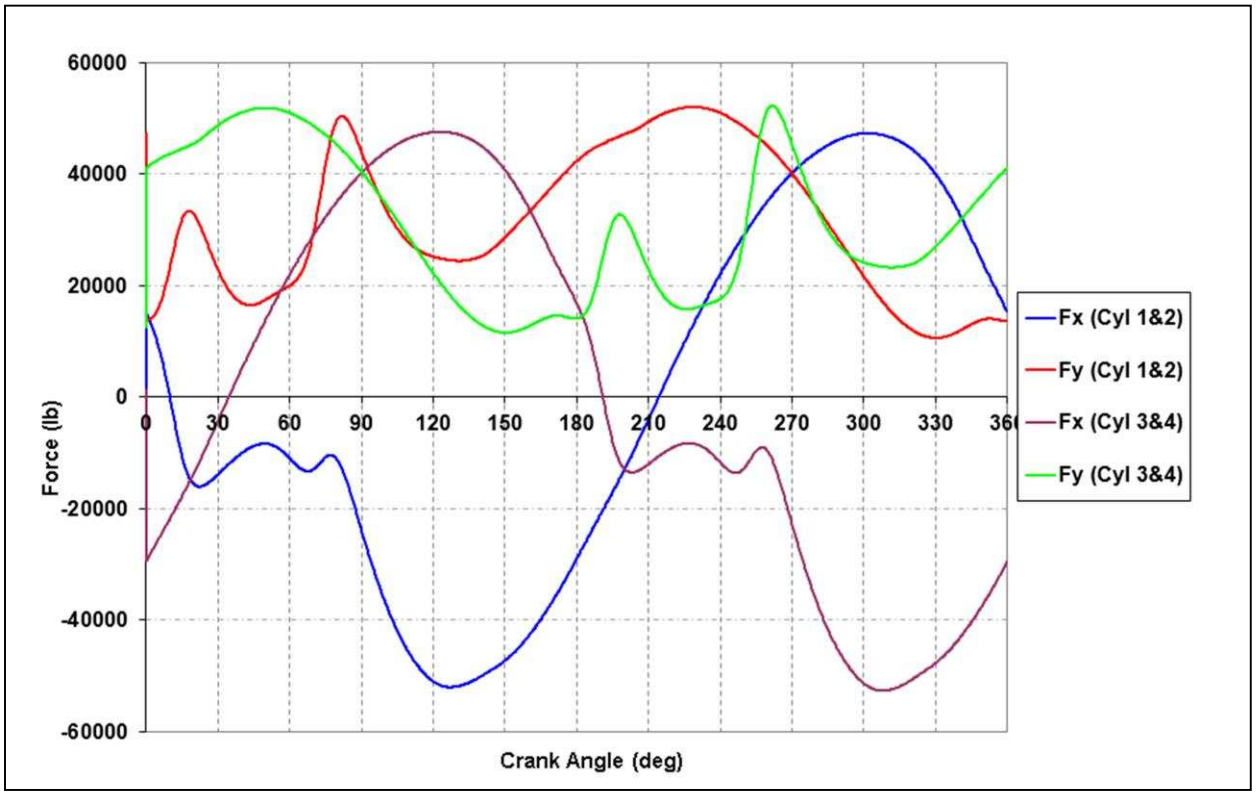

Figure 37: Working Model Force Outputs [21]

To predict how the bearing load would change at uprated conditions, a relationship from the original model was determined. The Working Model simulation used a number of equations to predict how the load would be transferred from the power pistons to the main crank bearings. The load on the bearings is directly related to the in-cylinder pressure and the speed of rotation. As the engine's operational speed would remain at 300 rpm at the uprated conditions, it was assumed the inertial loading on the crank bearings would relatively remain constant. To account for the greater in-cylinder pressures, GMVA and GMVH pressure data was obtained. The EECL had conducted testing on the LBET at GMVTF and GMVA conditions with peak pressures of ~500 psi and ~600 psi respectively. To determine the average peak pressure of a GMVH, data from Southwest Research Institute from their GMVH-6 research engine was obtained. The GMVH had a typical peak pressure of ~900 psi [38]. The pressure ratios were 6:5 for the GMVA condition and 9:5 for the GMVH condition. To determine the how the in-cylinder pressures related to the bearing force a correlation was created using Eureqa. Eureqa is a mathematical software tool originally created by Cornell's Creative Machines Lab and distributed by Nutonian, Inc. The software utilizes symbolic regression to determine the simplest mathematical equations to describe a given data set. Four models were developed to predict the x and y forces on the bearings.

Nine variables were input into the Eureqa's data set: crank angle [rad], cylinder 1 force [lbf], cylinder 2 force [lbf], cylinder 3 force [lbf], cylinder 4 force [lbf], force x for bearings group 1, force y for bearings group 1, force x for bearings group 2, and force y for bearings group 2. The cylinder force bearing group and crank angle data were designated as the input and the bearing force data were designated as the output. Four models were created to predict the force magnitude for each of the output variables, defined by the function in Figure 38. Notice that "crank" was defined as function of sine or cosine and bearing group 1 was only dependent upon cylinders 1 and

2, like bearing group 2 was only dependent upon cylinder 3 and four. These parameters were chosen because the crank had cyclic pattern that can be approximated by a combination of trigonometric functions. And the original Working Model simulation had the same input force arrangement for the two bearing groups.

The Eureqa software was left to run for 84 hours to develop a correlation for the four components of the bearing forces. A comparison between the original case and the predicted case can be seen in Figure 39 for x force of bearing group 1. All four Eureqa models matched the original prediction just as well. Figure 40 shows the extrapolation of the Eureqa model predicting the force outputs for the GMVA and GMVH conditions. As expected, at the peak pressure events of cylinders 1 and 2 the model predicts greater bearing load but at all other part of the cycle the model does not predict much change in the predicted bearing force. It was noted that the Eureqa model may have over predicted the bearing forces at cylinder peak pressures. In Figure 40, the GMVH bearing force was predicted to be 4.5 times greater than the GMVTF condition when the peak pressure was only 1.8 times greater. Based on this observation all predictions from the Eureqa model were used except for the peak pressure cases. At the peak pressure cases a force ratio was determined based upon the peak pressures to multiply the GMVTF case by. The ratio between GMVA and GMVTF was 6:5 and between GMVH and GMVTF was 6:5.

Fx1 = f((Cylinder 1)*sin(Crank), (Cylinder 1)*cos(Crank), (Cylinder 2)*sin(Crank), (Cylinder 2)*cos(Crank), (Cylinder 1), (Cylinder 2))

Fy1 = f((Cylinder 1)*sin(Crank), (Cylinder 1)*cos(Crank), (Cylinder 2)*sin(Crank), (Cylinder 2)*cos(Crank), (Cylinder 1), (Cylinder 2))

Fy2 = f((Cylinder 3)*sin(Crank), (Cylinder 3)*cos(Crank), (Cylinder 4)*sin(Crank), (Cylinder 4)*cos(Crank), (Cylinder 3), (Cylinder 4))

Fx2 = f((Cylinder 3)*sin(Crank), (Cylinder 3)*cos(Crank), (Cylinder 4)*sin(Crank), (Cylinder 4)*cos(Crank), (Cylinder 3), (Cylinder 4))

Figure 38: Eureqa Model Definition Functions

Eight points of interest were determined as likely points of high crankcase stress. The four peak pressure events and four high magnitude points between the peak pressure points were determined as the points of interest. These eight points were also extrapolated to the GMVA and GMVTF cases. Table 4 has complete list of bearing input forces for the FEA simulation.

The four bearing force prediction equations can be seen in Figure 41.

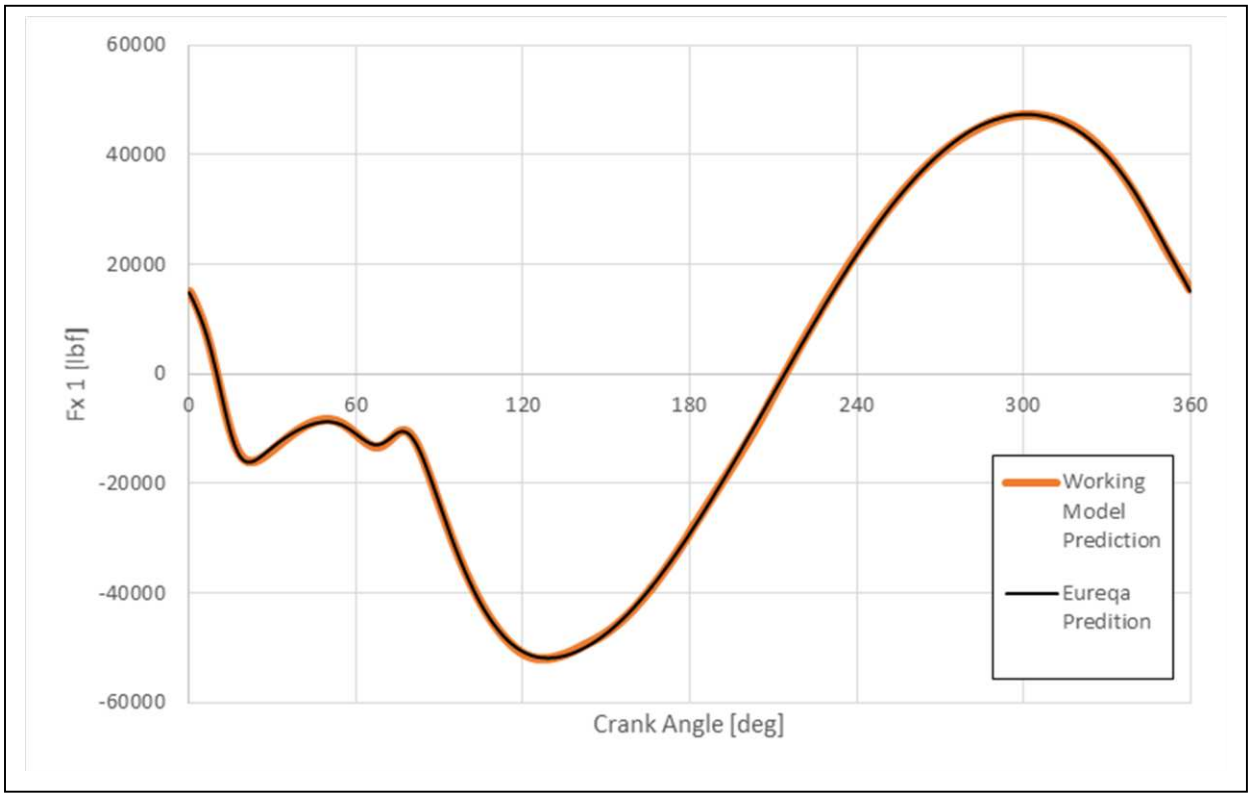

Figure 39: Force x for Bearing Group 1 Prediction

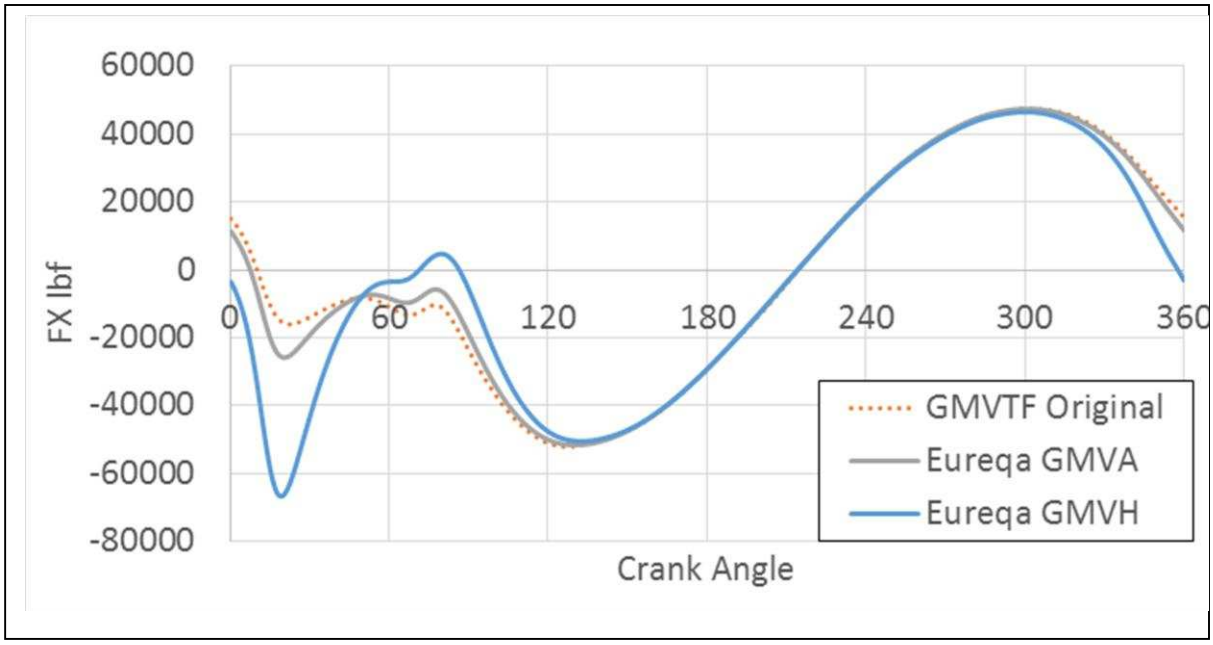

Figure 40: Eureqa Model Extrapolation

$$Fx1 = 26190.8321692538 * \cos(Crank) + 0.380162614368341 * (Cylinder\ 2) * \sin(Crank) + 0.431614877825036 * (Cylinder\ 2) * \sin(Crank) * \cos(Crank) - 2906.28481120668 - 43766.1771040602 * \sin(Crank) - 3.89640790435468e-6 * (Cylinder\ 1)^2 - 0.117196977464897 * (Cylinder\ 1) * \sin(Crank) - 1.85497842363945e-6 * (Cylinder\ 2)^2 * \sin(Crank) * \cos(Crank)$$

$$Fy1 = 15632.3901219083 + 0.70434411892895 * (Cylinder\ 1) + -\frac{33720426.5295551}{Cylinder\ 2} + 0.783833789125519 * (Cylinder\ 2) * sin(Crank) + \frac{-26833.9758996126 * (Cylinder\ 2) * cos(Crank) - 30994.7191659876 * (Cylinder\ 2) * sin(Crank)}{(Cylinder\ 2) - 430.297946416151} - 0.0270047482483026 * (Cylinder\ 1) * sin(Crank) - 0.0595178205918653 * (Cylinder\ 2) * cos(Crank)$$

$$Fy2 = 1724.6689217039 + 0.865765617161382 * (Cylinder\ 4) + 0.863050795429134 * (Cylinder\ 3) + 31005.5393170058 * cos(Crank) + 25342.5288021276 * sin(Crank) + 7.48794957520975e-6 * (Cylinder\ 3) * (Cylinder\ 4) * cos(Crank) + \frac{22591145.4767864 * (Cylinder\ 4) * sin(Crank) - 7138312039.59382}{(Cylinder\ 4)^2}$$

$$Fx2 = 43596.1729505245 * sin(Crank) + 0.152681058192636 * (Cylinder\ 3) * sin(Crank) + 0.453695965263003 * (Cylinder\ 4) * sin(Crank) * cos(Crank) - 2700.70130440417 - 26948.0390566538 * cos(Crank) - 3.81094682631715e-6 * (Cylinder\ 3)^2 - 0.38784006128314 * (Cylinder\ 4) * sin(Crank) - 2.40993225141399e-6 * (Cylinder\ 4)^2 * sin(Crank) * cos(Crank)$$

Figure 41: Final Eureqa Output Equations

Ansys Mechanical has the ability to simulate the characteristics of a bearing load, using the "bearing load" load constraint. The constraint was assumed to be identical for bearings 1 and 2 using the F_{12x} and the F_{12y} forces, similarly the F_{34x} and the F_{34x} were used for bearing 3 and 4 on the engine. The bearing surfaces were selected, seen in Figure 42, and twenty four load case were analyzed, eight points from the three operating conditions.

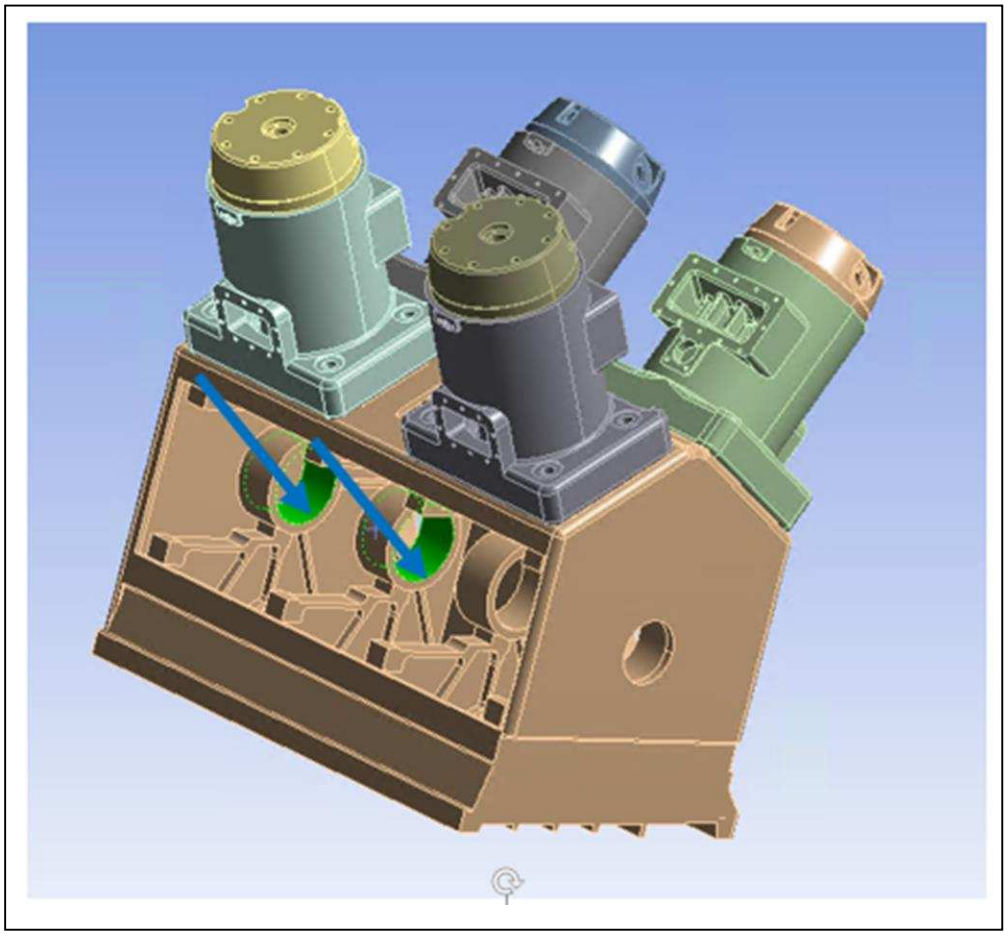

Figure 42: Bearing Load Force Input for Bearings 3 and 4

Table 4: FEA Bearing Input Forces

GMV-TF

Crank Angle [deg]	Fx1 [lbf]	Fy1 [lbf]	Fx2 [lbf]	Fy2 [lbf]	Magnitude 1 [lbf]	Magnitude 2 [lbf]
18.00	1.48E+04	-3.30E+04	1.49E+04	-4.47E+04	3.61E+04	3.62E+04
50.50	8.57E+03	-1.72E+04	-1.36E+04	-5.18E+04	1.92E+04	2.19E+04
80.50	1.18E+04	-4.97E+04	-3.50E+04	-4.45E+04	5.10E+04	6.08E+04
127.25	5.19E+04	-2.41E+04	-4.63E+04	-1.90E+04	5.72E+04	5.22E+04
197.75	1.44E+04	-4.74E+04	1.17E+04	-3.28E+04	4.96E+04	4.88E+04
229.25	-1.32E+04	-5.19E+04	8.39E+03	-1.60E+04	5.36E+04	5.26E+04
260.50	-3.55E+04	-4.47E+04	1.04E+04	-5.21E+04	5.71E+04	4.58E+04
307.75	-4.70E+04	-1.71E+04	5.26E+04	-2.34E+04	5.00E+04	5.53E+04

GMV-A

Crank Angle [deg]	Fx1 [lbf]	Fy1 [lbf]	Fx2 [lbf]	Fy2 [lbf]	Magnitude 1 [lbf]	Magnitude 2 [lbf]
18.00	1.76E+04	-4.01E+04	1.49E+04	-4.54E+04	4.38E+04	4.28E+04
50.50	1.01E+04	-2.12E+04	-1.36E+04	-5.17E+04	2.35E+04	2.52E+04
80.50	1.42E+04	-6.03E+04	-3.49E+04	-4.44E+04	6.20E+04	6.97E+04
127.25	6.24E+04	-2.95E+04	-4.58E+04	-2.04E+04	6.90E+04	5.45E+04
197.75	1.44E+04	-4.83E+04	1.40E+04	-3.93E+04	5.04E+04	5.02E+04
229.25	-1.32E+04	-5.26E+04	1.01E+04	-1.92E+04	5.42E+04	5.36E+04
260.50	-3.54E+04	-4.56E+04	1.24E+04	-6.26E+04	5.77E+04	4.72E+04
307.75	-4.68E+04	-2.01E+04	6.32E+04	-2.80E+04	5.09E+04	6.63E+04

GMV-H

Crank Angle [deg]	Fx1 [lbf]	Fy1 [lbf]	Fx2 [lbf]	Fy2 [lbf]	Magnitude 1 [lbf]	Magnitude 2 [lbf]
18.00	2.63E+04	-6.01E+04	1.49E+04	-4.75E+04	6.57E+04	6.20E+04
50.50	1.51E+04	-3.18E+04	-1.34E+04	-5.24E+04	3.52E+04	3.46E+04
80.50	2.13E+04	-9.05E+04	-3.43E+04	-4.53E+04	9.29E+04	9.68E+04
127.25	9.37E+04	-4.42E+04	-4.42E+04	-2.54E+04	1.04E+05	6.25E+04
197.75	1.44E+04	-5.00E+04	2.10E+04	-5.90E+04	5.21E+04	5.42E+04
229.25	-1.31E+04	-5.42E+04	1.51E+04	-2.88E+04	5.57E+04	5.62E+04
260.50	-3.51E+04	-4.73E+04	1.86E+04	-9.38E+04	5.89E+04	5.09E+04
307.75	-4.60E+04	-2.66E+04	9.48E+04	-4.21E+04	5.31E+04	9.84E+04

3.3.1.2 Pressure Forces

Schmitt's models assumed the forces exerted by pressure were mono-directional along the connecting rods, into the crank bearings, when in reality the in-cylinder pressure exerts force in all directions. Reynolds French noted failures were common along the upper web of the engine which Schmitt did not find as an area of interest in his models. By including the cylinder heads in the model, the reactionary forces of the combustion events can now be included. Three sources of pressure data were used in conjunction with the predicted bearing forces to simulate the engine running at GMVTF, GMVA, and GMVH conditions.

The pressure forces were inputted into the model using the "pressure" load constraint. The top of cylinder heads were the selected surfaces where the forces of interest and cylinder walls were neglected. It was assumed the hoop stress exerted on the cylinder walls would not

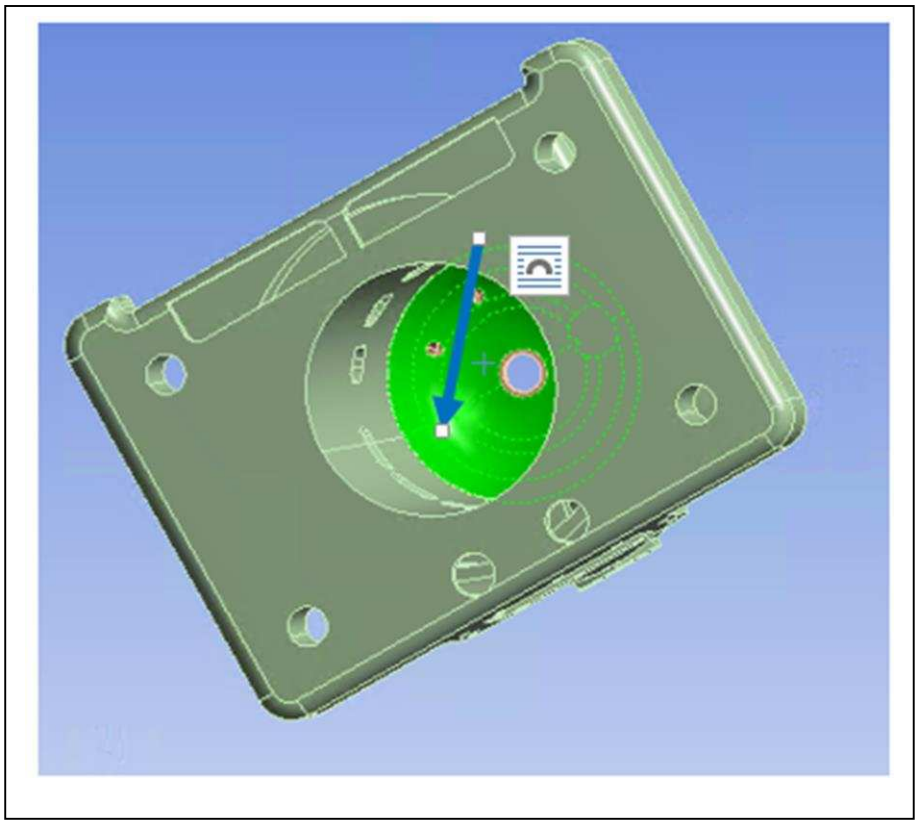

Figure 43: Pressure Force Load Constraint on Cylinder Head 2

substantially affect the forces transferred to the upper web of the crankcase. The pressure loads were inputted to act normal to the surface of interest, seen in Figure 43, using the same tabular method as the bearing loads at the same eight points for each engine condition, with values seen in Table 5.

Table 5: FEA Pressure Input Forces

GMV-TF					
Crank Angle [deg]	Cylinder 1 [psi]	Cylinder 2 [psi]	Cylinder 3 [psi]	Cylinder 4 [psi]	Significance
18.00	504.42	81.33	16.00	13.15	PP of Cyl 1
50.50	207.55	252.44	16.61	13.38	High Magnitude
80.50	99.59	504.42	20.44	16.16	PP of Cyl 2
127.25	41.02	140.84	62.20	20.40	High Magnitude
197.75	16.00	25.54	485.78	91.86	PP of Cyl 3
229.25	16.01	15.15	210.73	237.50	High Magnitude
260.50	19.36	16.06	97.12	520.47	PP of Cyl 4
307.75	62.28	16.02	42.00	129.53	High Magnitude
GMV-A					
Crank Angle [deg]	Cylinder 1 [psi]	Cylinder 2 [psi]	Cylinder 3 [psi]	Cylinder 4 [psi]	Significance
18.00	605.31	97.60	19.21	15.78	PP of Cyl 1
50.50	249.06	302.93	19.94	16.06	High Magnitude
80.50	119.50	605.31	24.53	19.40	PP of Cyl 2
127.25	49.23	169.00	74.64	24.48	High Magnitude
197.75	19.20	30.64	582.94	110.23	PP of Cyl 3
229.25	19.22	18.18	252.88	285.00	High Magnitude
260.50	23.23	19.27	116.54	624.56	PP of Cyl 4
307.75	74.73	19.23	50.40	155.44	High Magnitude
GMV-H					
Crank Angle [deg]	Cylinder 1 [psi]	Cylinder 2 [psi]	Cylinder 3 [psi]	Cylinder 4 [psi]	Significance
18.00	907.96	146.40	28.81	23.68	PP of Cyl 1
50.50	373.59	454.39	29.90	24.09	High Magnitude
80.50	179.25	907.96	36.79	29.10	PP of Cyl 2
127.25	73.84	253.50	111.95	36.72	High Magnitude
197.75	28.81	45.96	874.40	165.34	PP of Cyl 3
229.25	28.82	27.27	379.32	427.50	High Magnitude
260.50	34.85	28.90	174.81	936.84	PP of Cyl 4
307.75	112.10	28.84	75.60	233.16	High Magnitude

The FEA predicted stresses were ignored in the cylinder heads because the installed cylinders are from a GMVH were assumed to be able to safely operate at the uprated condition.

3.3.1.3 Crankcase Constraints and Assumptions

Defining the constraints on an object when conducting FEA is equally as important as properly defining the force inputs [24]. The GMV User's Manual specifies the mounting system for the LBET should be very stable and level [16]. The mounting system was designed to be long lasting and maintain rigidity. To simulate the mounting system on the LBET, the base of the modeled crankcase was defined as a fixed support in Ansys. The fixed support constraint prevents movement in all six degrees of freedom, meaning the crankcase cannot translate or rotate.

Recall from Figure 36 the cover plates, above where the material specimens were removed, were not modeled. The cover plates provided additional structural support to the engine and constraints were needed to simulate them. The remote displacement tool was utilized to maintain a rigid distance between the top of the opening and the bottom with properties consistent with the assumed class 25 meehanite properties.

After the selection of the constraints and loads, the model was ready to move to in depth analysis.

3.3.2 Analysis

The analysis step of FEA was where the model was interpreted by the Ansys Mechanical Code. Ansys Mechanical discretized the elements and nodes constructing a system of linear and non-linear equations to predict the model's reaction to forces [36]. Equation 8 represents the matrix

Equation 8: FEA Node Reaction Matrix [36]

$$K_{ij}u_{ij} = f_{ij}$$

construction of the system of equations Ansys used to predict the results of each discrete point. "K_{ij}" was the constructed matrix dependent on the type of point and the method to numerically solve for it, "f_{ij}" represents the input forces at the given point, and "u_{ij}" was the reaction of the point. Ansys conducted thousands of calculations per second but user did not directly interact with this aspect of the program. Ansys provides a status bar to let the user know where in the calculation process the program was, Figure 44. Despite the modern computing power, the average run-time for the fully constructed model was upwards of five hours.

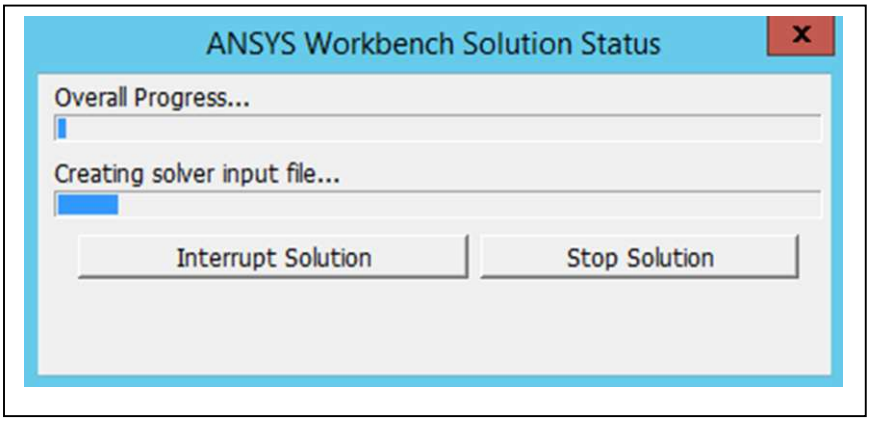

Figure 44: Ansys Workbench Solution Status Window

3.3.3 Post-Processing, FEA Results

Ansys Mechanical can calculate deformation, strain, stress, energy, and damage each node would sustain at the given condition. Meehanite metal gave the failure fatigue stress of the GE-30 grade of meehanite as 13.5 ksi and ASTM specifies the fatigue strength of class 25 irons as 12 ksi so the predicted Von Mises stress at each node must be less than 12 ksi to avoid fatigue failure [19][20][32]**.** The Von Mises stress was calculated because it allows for direct comparison to the ultimate strength and endurance limit of a material [20].

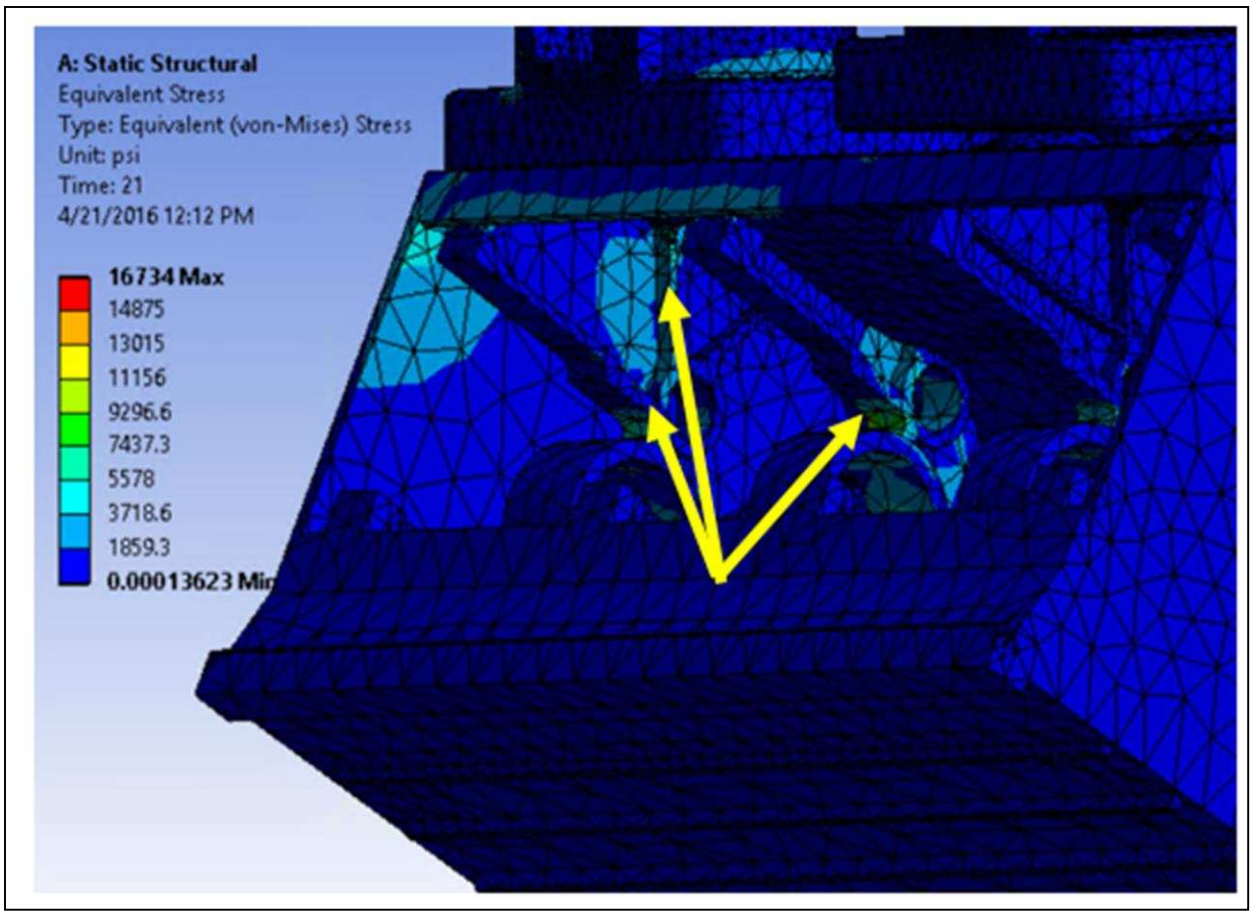

Figure 45: Areas of Maximum Stress above Bearings 3 and 4 at PP for Cylinder 3 at GMVH Rating

Figure 45 displays the regions of high stress above main crank bearings three and four at peak pressure for cylinder 3 at GMVH rating. As can be seen in Figure 45, the maximum stress for the entire engine is 16,734 psi but this was measured in head of cylinder 3 while the max stress in the crankcase at this test point was 9,621psi. Recall the predicted stress within the cylinder head will be neglected as they are GMVH cylinders and are assumed to be able to operate at GMVH rating. The high stress regions directly above the bearing are consistent with the findings of Schmitt, while high stress region along the upper web is where Reynold French typically sees premature engine failure in the field [21] [35]. The stresses below cylinders 1 and 2 were very similar as the stresses below cylinders 3 and 4 at their relative peak pressures. Looking towards on engine testing, mounting strain gauges below cylinders 3 and 4 is the most practical because there is already an

instrumentation port installed in the east crankcase door. Four points of interest were analyzed for each of the test cases, directly above bearing 3 and 4 and the upper webs above bearings 3 and 4, seen in Table 6. The max stress were often seen above the main crank, likely due to model simplifications.

Recall, class 25 grade meehanite had a fatigue strength of 12 ksi. None of the points of interest approached this level of stress but the some of the max stress values in the crankcase at GMVH level were above this fatigue strength. The model's max stress regions could not be practically instrumented nor was visual confirmation available to determine whether the regions were accurately modeled.

The results in Table 6 were the final FEA iteration of the LBET before strain gauge measurements were taken. Based upon the on-engine measurement, outlined in chapter 4, the model was progressively iterated and improved to create the most accurate representation of the GMV crankcase. But by simply looking at the max stress values it is possible the LBET could be operated at GMVH levels but at this operation point there would no factor of safety. However, this is not advised as the identified regions of max stress could not be visually verified to determine if they were an accurate representation of the crankcase.

Table 6: FEA Model Results

GMV-TF

Crank Angle	Above Bearing 4	Upper Web 4 [psi]	Above Bearing 3 [psi]	Upper Web 3 [psi]	Max Crankcase Stress [psi]
18.00	833	295	1024	586	6549
50.50	1022	710	1202	472	7427
80.50	1249	752	1530	428	7562
127.25	727	954	1205	422	2968
197.75	1750	1027	1670	1186	5228
229.25	967	665	922	647	6397
260.50	854	481	874	548	6711
307.75	1180	234	1524	961	3600
Max	1750	1027	1670	1186	7562

GMV-A

Crank Angle	Above Bearing 4	Upper Web 4 [psi]	Above Bearing 3 [psi]	Upper Web 3 [psi]	Max Crankcase Stress [psi]
18.00	986	1205	345	703	7842
50.50	1239	1463	825	569	8935
80.50	1486	1817	879	511	9043
127.25	904	1447	1177	525	3533
197.75	2130	2019	1243	1589	6298
229.25	1194	1122	798	805	7692
260.50	997	1016	596	687	8039
307.75	1410	1813	255	1186	4320
Max	2130	2019	1243	1589	9043

GMV-H

Crank Angle	Above Bearing 4	Upper Web 4 [psi]	Above Bearing 3 [psi]	Upper Web 3 [psi]	Max Crankcase Stress [psi]
18.00	1512	1845	515	1081	11784
50.50	1865	2194	1244	833	13358
80.50	2272	2768	1344	771	13607
127.25	1336	2140	1692	734	5341
197.75	3161	3018	1872	2130	9386
229.25	1711	1638	1226	1167	11526
260.50	1549	1583	867	955	12046
307.75	2145	2732	450	1704	6489
Max	3161	3018	1872	2130	13607

4 ON-ENGINE MEASUREMENTS

4.1 OVERVIEW

Based on the findings from the modeling analysis and historical field data the regions of concern were determined to be above the main crank bearings and along the upper webs of the LBET crankcase. To determine the validity of the findings from chapter 3, on engine measurements were completed using strain gauges. The strain gauges were calibrated on an external test piece and were then mounted inside the crankcase.

4.2 ENGINE OPERATION AND DATA ACQUISITION

The LBET operates at 300 rpm, loaded with a computer-controlled, water brake dynamometer to provide load control. The nominal rated load is 440 bhp, which corresponds to a BMEP of 68 psi. For this testing the engine was to be operated at a GMVA rating of 500 bhp, which corresponds to a BMEP of 77 psi.

The LBET is controlled and monitored using a LabVIEW data acquisition system. The system monitors, records, and controls important engine operating parameters. These measurements are taken at a speed of 2 Hz or once every half second. A snapshot of the front panel of the LabVIEW program can be seen in Figure 46. The data acquisition system is also interfaced with a high speed combustion analyzer.

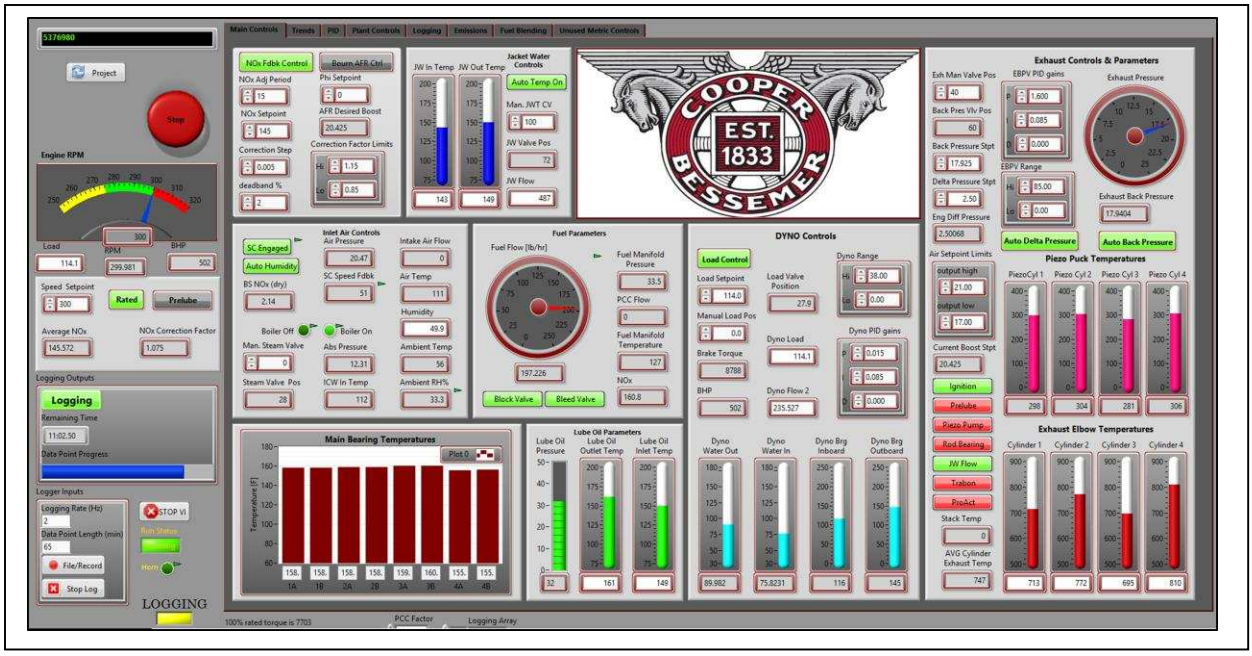

Figure 46: LBET LabVIEW Control Panel Controller

The central component of the high speed system is an NI PXI-1002, interfaced with a high resolution encoder. The NI system records the signal inputs at every step of the encoder, meaning 3,600 data point are taken per revolution. The signal inputs are four cylinder pressure transducers and the six strain gauge signal conditioners. The data from the NI system is then written into files containing 1,000 complete combustion cycles, roughly capturing three minutes of data. The data files can then be post processed to determine the combustion and strain characteristics.

4.3 STRAIN GAUGE THEORY, CALIBRATION, AND ENGINE MOUNTING

4.3.1 Strain Gauge Theory

Engineering strain is the fractional relationship between amount of deformation and the original "length" of the area illustrated in Equation 9 and Figure 47 [39]. Engineering strain is a dimensionless parameter but is often expressed with units of in/in.

Equation 9: Engineering Strain

$$\varepsilon = \frac{\Delta L}{L}$$

There are many methods to measure strain but the most common method is with a strain gauge. A strain gauge works by relating the amount of electrical resistance to the amount of deformation [39]. A strain gauge consists of a set of metallic foils arranged in a grid pattern. The grid pattern is designed to maximize the amount of wire parallel to the active strain direction and to minimize the cross sectional area. This arrangement enhances the strain signal in the active direction while minimizing the effects of shear strain. All strain gauge foils have nominal resistances with the most common being 120Ω, 350 Ω, and 1,000 Ω.

To determine the amount of measured strain the foil's gauge factor (GF) must be known. The gauge factor is the foil's sensitivity to strain and is defined as the ratio of fractional change in electrical resistance to the engineering strain, illustrated in Equation 11.

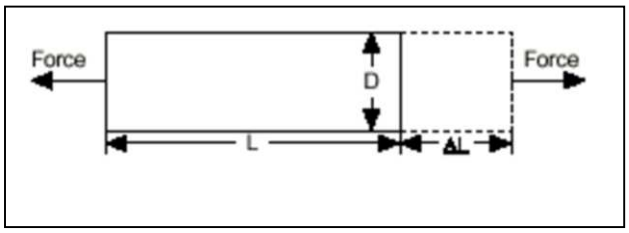

Figure 47: Illustration of Strain [39]

Equation 11: Gauge Factor Relationship

$$GF = \frac{\Delta R/R}{\Delta L/L} = \frac{\Delta R/R}{\varepsilon}$$

Suppose the point of interest undergoes moderate strain of 500 x 10^{-6} in/in. A strain gage with a gage factor of 2 and nominal resistance of 120 Ω will experience a change in electrical resistance of 0.12 Ω, or a 1% change. To accurately measure such a small change in resistance, strain gauges are configured with a voltage excitation source in a Wheatstone bridge, shown in Figure 48. The bridge consists of four resistive arms with an excitation voltage, of $V_{ex,}$ applied across the bridge with the output of the bridge V_o defined in Equation 10.

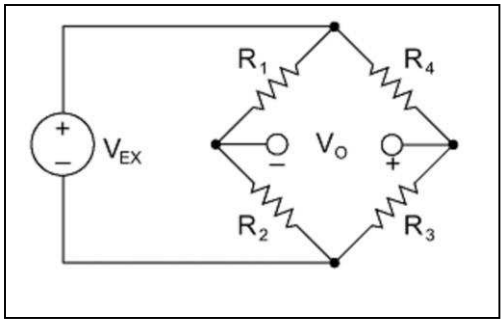

Figure 48: Wheatstone Bridge [39]

Equation 10: Output Voltage Equation

$$V_o = \left[\frac{R_3}{R_3 + R_4} - \frac{R_2}{R_1 + R_2}\right] * V_{ex}$$

There are different bridge configuration to determine the placement of the strain gauges in the circuit. The "quarter bridge" configuration replaces R_4 with a strain gauge with nominal resistance of R_G while the other three resistors should equal the nominal resistance of the strain gauge. When there is no strain on the system the bridge will be "balanced" because $R_G=R_1=R_2=R_3$ and the output voltage will be zero. Once a strain is applied to the system, the bridge will be "unbalanced" because $R_G \neq R_1=R_2=R_3$ and the output voltage will respond accordingly. The relationship from Equation 11 is plugged into Equation 10 the response of voltage output is defined in Equation 12 for the quarter bridge configuration.

Equation 12: Quarter Bridge Vo response

$$\frac{V_o}{V_{ex}} = \frac{-GF * \varepsilon}{4}\left(\frac{1}{1 + GF * {}^{\varepsilon}/_{2}}\right)$$

The circuitry for a quarter Wheatstone bridge, less the strain gauge, is often a part of an integrated circuit called a signal conditioner. A signal conditioner will provide the excitation voltage, the three reference resistors, and as well as calibration ability. The data acquisition system can then store the output voltage and post processing can be used to determine the strain at the point of interest.

Strain rarely occurs in a uniaxial direction. To get an accurate representation of the strain at the points of interest, the transverse strain must also be accounted for. The most common method to measure the multidirectional strain is to use multi-foil strain gauge rosettes. Rosettes have three foils, known as the A, B, and C foils, with each foil oriented at 0°, 45°, and 90°, respectively. Each foil connected to its own quarter bridge signal conditioner to calculate its local strain.

Once the strain of each foil is determined, the elastic modulus (E) and Poissons ratio (ν) are used to calculate the two principle stresses outlined in Equation 13. The elastic modulus and Poisons ratio for class 25 meehanite are ~14,000 ksi and 0.29 respectively [20]. The two principle stresses are then used to calculate the two dimensional Von-Mises stress, Equation 14. The Von-Mises stress is used to predict the equivalent stress at the point of interest as if the entire stress was being loaded in a uniaxial tensile direction [20].

The calculated Von-Mises stress can then be compared to the modeled Von-Mises stresses from chapter 3.

Equation 14: Principle Stress Calculation for Three Foil Rosette

$$\sigma_{12} = \frac{E}{2} * \frac{(\epsilon_A + \epsilon_C)}{1 - \upsilon} \pm \frac{\sqrt{(\varepsilon_A - \epsilon_C)^2 + (\varepsilon_B - \varepsilon_A - \varepsilon_C)^2}}{1 + \nu}$$

Equation 13: Two Dimensional Von-Mises Stress

$$\sigma_{von\ mises} = \sqrt{\sigma_1^2 - \sigma_1\sigma_2 + \sigma_2^2}$$

4.3.2 Strain Gauge Instrumentation and Calibration

Six Omega strain gauge signal conditioners were used for this project, seen in Figure 49. To minimize project costs, the strain gauges were selected to be compatible with the signal conditioner. The signal conditioners provided an excitation voltage of 10V and had nominal resistance values of ~120Ω for the remaining three legs of the Wheatstone bridge. A complete

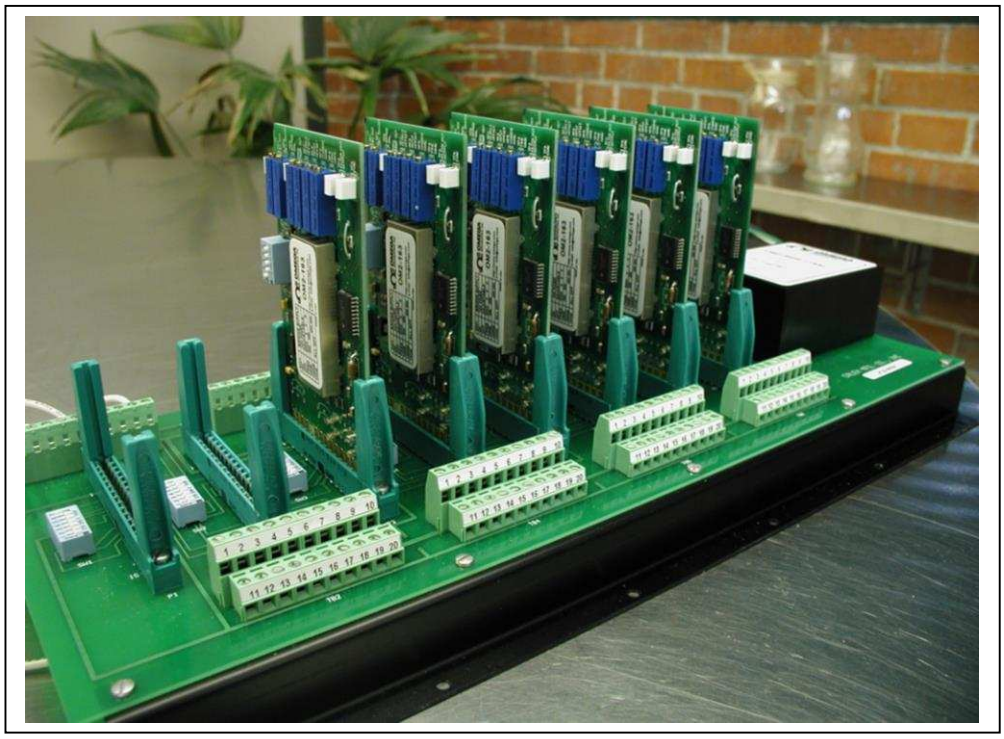

Figure 49: Omega Strain Gauge Signal Conditioners

product description of the signal conditioners is available in Appendix D. To meet these requirements Omega KFH-6 three foil strain gauge rosettes were selected, seen in Figure 50. Each of the three foils had a nominal resistance of 120.4 Ω ± 0.35% and gauge factor of 2.04 ± 1.0%.

To evaluate the accuracy of the strain gauges and the signal conditioners a test apparatus was constructed. The apparatus was designed to put a bending moment and a torsional load at a point of interest.

A cantilever beam with a torsional offset was selected as the designed test apparatus, seen in Figure 51. The apparatus was constructed out of 4" by 4" square steel tube with 0.25" thickness as the base and a 24.5" steel tube with an outer diameter of 1.32" and a wall thickness of 0.24" and

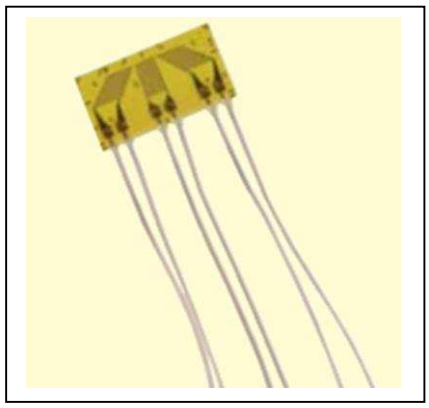

Figure 50: KFH-6 Three Foil Strain Gauge

Figure 51: Torsional Cantilever Beam Apparatus

welded to the base. And finally a 7.5” x 2” angle stock was welded to the end with 0.18” thickness. The apparatus was also modeled in Creo Parametric to conduct FEA on the bar. The Ansys model of the apparatus can be seen in Figure 52. The load was applied to the end of the edge of the angle stock and the square tube base was assumed to be rigidly mounted to the table. As expected, the area of greatest stress was at the end of the steel pipe where the torsional and bending moments were maximized. In conjunction with the FEA model, a closed form solution was also completed as a third check to the FEA assumptions and the strain gauge measurements. Figure 53 is the collection of governing equations used to calculate the closed form solution for a torsional cantilever beam with a ~10 lb force applied [20].

For a ~10 lb load the closed form solution predicted a stress of 1623.4 psi and the FEA model predicted a stress of 1617 psi, a 0.4% difference. The strain gauge was mounted onto the test apparatus using the provided epoxy. It was mounted 20” from the end of bar where the weight was attached. The strain gauge was interfaced with three of signal conditioners for each test. Three

Figure 52: Ansys FEA Model of Test Apparatus

loading and unloading events were measured with an average calculated stress of 1567 psi. This corresponds to a 3% difference between the predicted stresses and the measured stresses. Following this result, the signal conditioners and strain gauges were deemed acceptable to begin mounting inside the LBET crankcase.

Knowns:

$d_o := 1.32in$ $d_i := d_o - 2 \cdot 0.127in$ $d_i = 1.066 \cdot in$ Measured pipe dimensions

$l_1 := 7in$ $l_2 := l_1 - \frac{d_o}{2}$ $l_2 = 6.34 \cdot in$ Length or torque arm

$l_3 := 20in$ Distance from end of bar to location of strain gage

$J := \frac{\pi}{32} \cdot \left({d_o}^4 - {d_i}^4 \right)$ $J = 0.171 \cdot {in}^4$ Torsion moment of inertia

$I := \frac{\pi}{64} \cdot \left({d_o}^4 - {d_i}^4 \right)$ $I = 0.086 \cdot {in}^4$ Bending moment of inertia

Assumptions:

Torsion bar is mild steel
Torsion bar is is in a combination of pure bending and pure torsion

$F := 10.157lbf$ $T_2 := F \cdot l_2$ $T_2 = 64.4 \cdot lbf \cdot in$ $\tau_{xy2} := \frac{T_2 \cdot r}{J}$ $\tau_{xy2} = 248.1 \cdot psi$

$M_2 := F \cdot l_3$ $M_2 = 203.1 \cdot lbf \cdot in$ $\sigma_{x2} := \frac{M_2 \cdot c}{I}$ $\sigma_{x2} = 1565.5 \cdot psi$

$$\sigma_{1\_2} := \frac{\sigma_{x2} + \sigma_y}{2} + \sqrt{\left(\frac{\sigma_{x2} - \sigma_y}{2} \right)^2 + {\tau_{xy2}}^2}$$ $\sigma_{1\_2} = 1603.9 \cdot psi$

$$\sigma_{3\_2} := \frac{\sigma_{x2} + \sigma_y}{2} - \sqrt{\left(\frac{\sigma_{x2} - \sigma_y}{2} \right)^2 + {\tau_{xy2}}^2}$$ $\sigma_{3\_2} = -38.4 \cdot psi$

$$\sigma'_{vm} := \sqrt{{\sigma_{1\_2}}^2 - \sigma_{1\_2} \cdot \sigma_{3\_2} + {\sigma_{3\_2}}^2}$$ $\sigma'_{vm} = 1623.4 \cdot psi$

Figure 53: Governing Equations and Calculations for Cantilever Beam

4.3.3 Strain Gauge Engine Mounting

Recall from chapter 3, the predicted stresses were very similar above all the crank bearings but the crankcase door in front of bearings three and four already had an instrumentation port to allow for instrumentation wiring to pass through the crankcase. This led to the decision to only mount the strain gauges behind this door to minimize engine modifications. Four locations were selected to mount the Omega strain gauges, directly above main crank bearing 3 and 4 and along the upper webs of the crank bearings, seen in Figure 54 and Figure 55. Originally only four strain

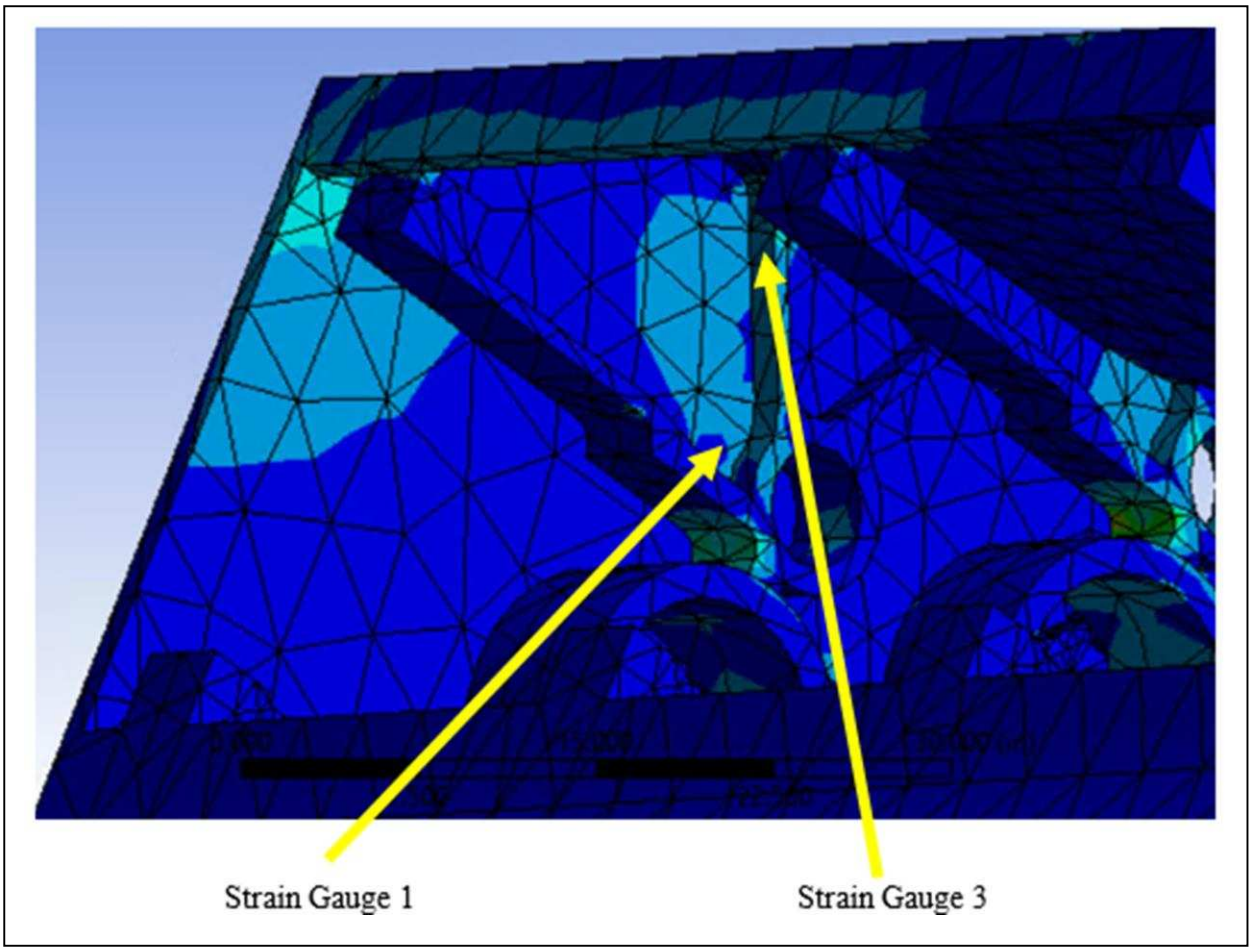

Figure 54: Strain Gauge 1 and 3 Mounting Locations Above Bearing 4

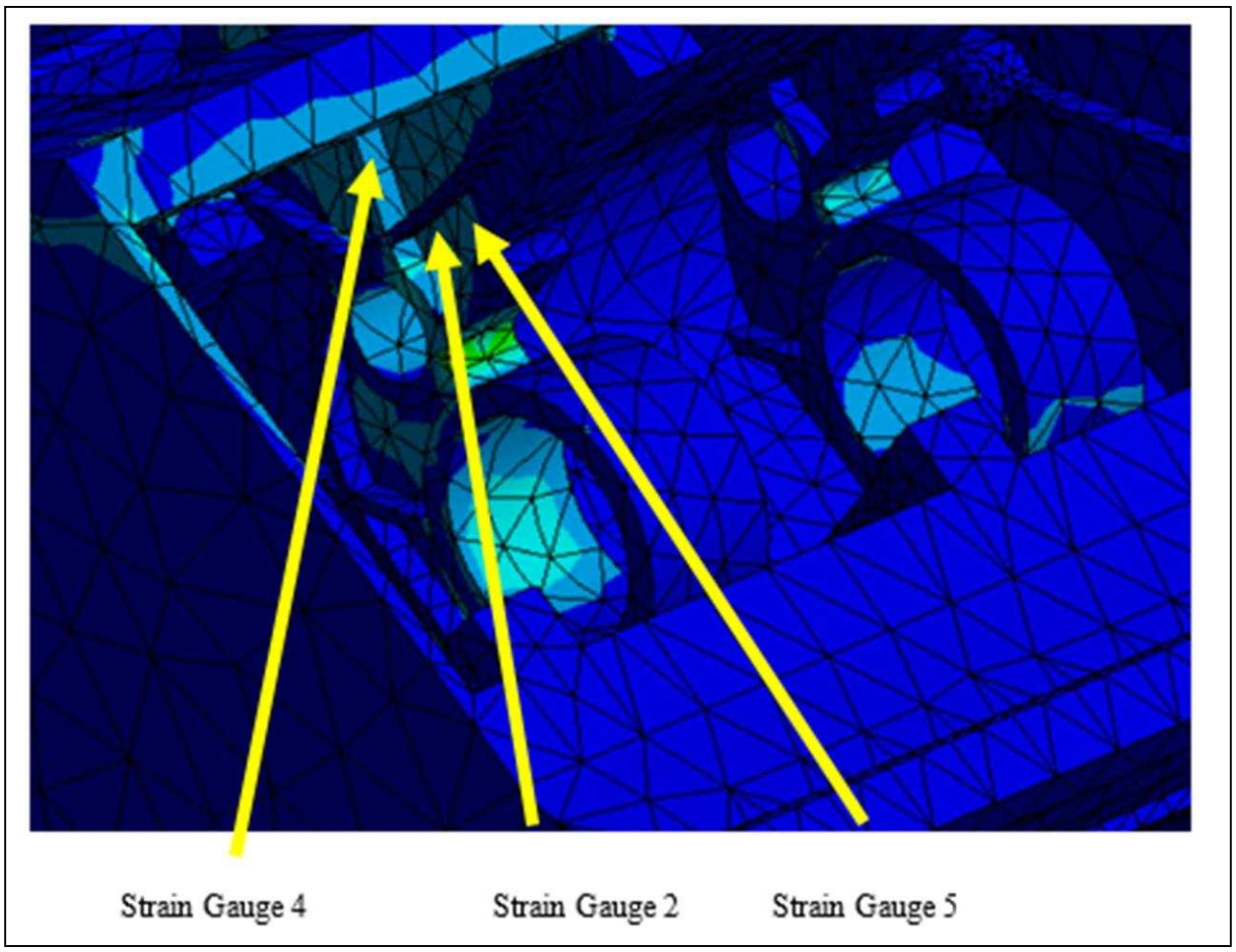

Figure 55: Strain Gauge 2, 4 and 5 Mounting Locations above Bearing 3

gauges were mounted, but after the first day of testing the original strain gauge number two failed. It was replaced and the last strain gauge, number 5, was also placed inside the crankcase as a redundancy measure.

Proper strain gauge mounting was crucial to obtain accurate strain measurements with the instructions provided by Omega in Appendix E. Once the crankcase door was removed a tarp was placed inside the crankcase to prevent the grinding contaminants from falling into the oil reservoir, seen in Figure 56. After the tarp was placed in the engine the mountain locations were marked inside the engine.

Figure 56: Tarp Placement in the Crankcase

As specified by Omega, the strain gauge must be directly mounted to the contaminant free surface. First the internal paint was ground off until the crankcase metal was exposed. It was then ground to a smooth uniform finish, followed by hand sanding using 120 grade Emery paper. This attained the desired surface finish to maximize adhesion and minimize the chance of air bubbles forming in the epoxy.

Surface cleaning was crucial to remove all grease and other contaminants. As specified by Omega, gauze pads were soaked in acetone to clean the mounting surface. Several rounds of cleaning were completed to ensure no contaminants were left on the surface. The same technique was used to clean the strain gauges before the mounting process.

The Omega strain gauge adhesive had a setting time of 60 to 120 seconds and required the user to very quickly secure the strain gauge after application. The adhesive was directly spread onto the strain gauge surface and then the gauge was quickly pressed to the location of interest in

the crankcase. The top of the strain gauge was held in place with a Teflon film for 2 to 3 minutes to ensure proper adhesion. These steps were repeated for all mounted strain gauges and were left to cure for 24 hours. After the curing process a nonconductive gasket material was placed over the strain gauges to mitigate oil contamination of the instruments. The final strain gauge mount locations can be seen in Figure 57.

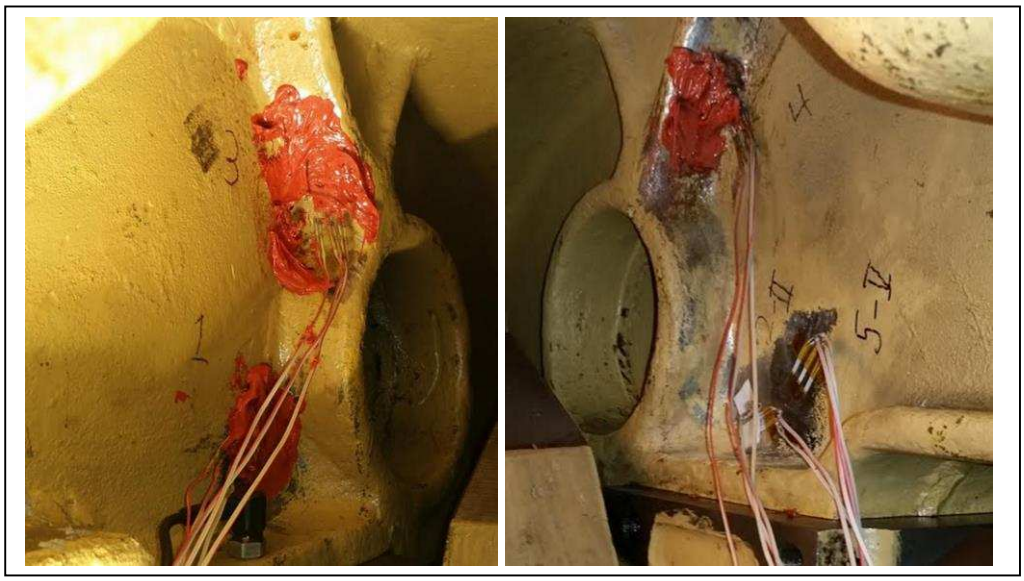

Figure 57: Final Strain Gauge Mounts

4.4 On Engine Strain Gauge Measurements

There were 3 testing blocks with measured strain data. The first testing block was conducted between January 5th and 9th of 2015, the second testing block was completed June 28th and 29th of 2015, and the third testing block was completed between September 29th and October 2nd of 2015.

The LBET was operated at GMVA rating to establish the baseline point of operation to determine the validity of the FEA modeling. The six strain gauge signal conditioners allowed for two of the five rosettes to be collected simultaneously. And were directly interfaced with the high speed combustion analyzer. Before any data points were taken the engine was allowed to reach temperature equilibrium. The selected Omega strain gauges were selected to have minimal

dependence on temperature when bonded to ferritic metals. The strain foils were designed to a have a thermal expansion coefficient very close to that of ferritic metals and as a result the output voltage was expected to vary by 1.63×10^{-8} volts per Rankine. The engine crankcase temperature was determined by measuring the lube oil and jacket water temperatures which were 160° F and 150° F, respectively. This corresponds to a measured voltage increase of 1.023×10^{-5} Volts, which was 3 orders of magnitude smaller than the average peak to peak voltage measurement.

Peak to peak voltage was determined as the best method to determine the dynamic strain at the points of interest. The peak to peak voltage value encompasses both the tension and compression aspects of the complete combustion cycle, but it was assumed the loading would primarily be in tension.

Two cylinder deactivation attempts were conducted on the LBET. To conduct the cylinder deactivation attempts no modification were made to the engine. The only changes from nominal operation was reducing the load on the dynamometer and shutting off the fuel to deactivated cylinders. The first attempt was successful at running the LBET with only cylinder 1 deactivated and the second attempt was able to deactivate both cylinders 1 and 3 and attain relatively stable operation.

4.4.1 Nominal Condition

Nominal condition data was taken during all three test blocks to establish a baseline for engine operation at the GMVA power rating. The engine was operated at constant speed of 300 rpm and loaded at 500 bhp with an average IMEP of ~150 psi and a BMEP of ~77 psi. Based on the FEA models the expected Von-Mises stress for strain gauges are outlined in Table 7.

During the first block of testing the strain data was unable to be interfaced with the LBET's encoder, as a result the strain data could only be analyzed against time. This error was corrected by the second block of testing and continued to work through the third block. In the second half of the first block of testing it was noted that strain gauge number two began to fail and was replaced before the second block of testing with addition of strain gauge 5 as redundancy. During the second block of testing strain gauge number one failed and was no longer valid for collecting strain data. Unfortunately, there were no spare strain gauges to correct this issue.

Table 7: Original Maximum FEA Predicted Von-Mises Stress at GMVA Rating

Original Maximum Predicted VM stress at each Strain Gauge Location				
Strain Gauge 1 [psi]	Strain Gauge 2 [psi]	Strain Gauge 3 [psi]	Strain Gauge 4 [psi]	Strain Gauge 5 [psi]
2130	2019	1243	1589	2019

4.4.1.1 Test Block 1

The high speed combustion analyzer did not calculate the stress and strain during the time of collection. The raw voltage signals were post processed to determine the Von-Mises stresses. The first test block was primarily focused on collecting data from the upper webs of the crankcase, strain gauges 3 and 4. But data were also taken from strain gauges 1 and 2, the results seen in Table 8. The data from strain gauge two was inconclusive because of an electrical short on its "A" foil.

Table 8: Test Block 1 On-Engine Stress Data

On-Engine Strain Data Test Block 1				
	Strain Gauge 1 [psi]	Strain Gauge 2 [psi]	Strain Gauge 3 [psi]	Strain Gauge 4 [psi]
Max Stress	2164	4709	988	1507
Stress Std Dev	77	84	58	104

The short was noticed during the post processing the strain data. The voltage traces for all other foils had a very smooth and regular curve. The voltage trace from the 2A foil was very jagged and did not follow a regular trend, shown in Figure 58. Note that all voltage traces but 2A are on the secondary y-axis. After disregarding strain gauge number two all the remaining data was analyzed and compared to the predicted FEA stress, shown in Figure 59.

The on-engine stress data was averaged together and the standard deviation was used to determine the error bars on the bar graph. The measured data from strain gauge 1 and 4 are very similar to the FEA prediction but the range for strain gauge number 3 did not align with the predicted stress from the FEA modeling. The original FEA model was analyzed to determine the discrepancy cause.

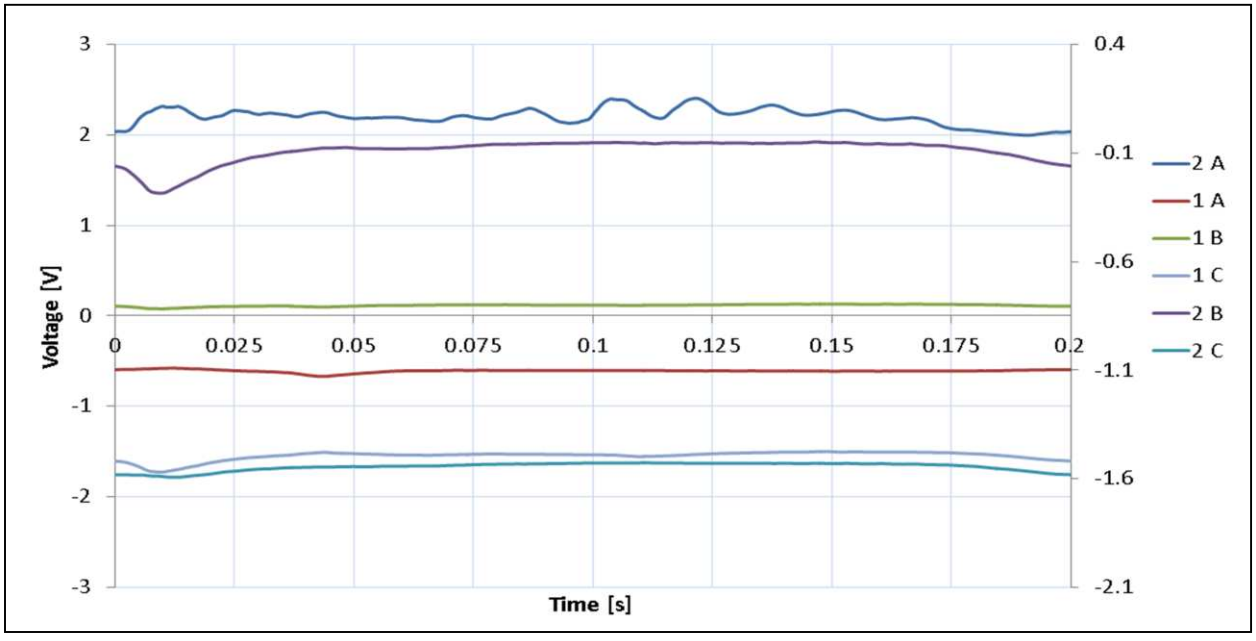

Figure 58: Foil 2A Electrical Short

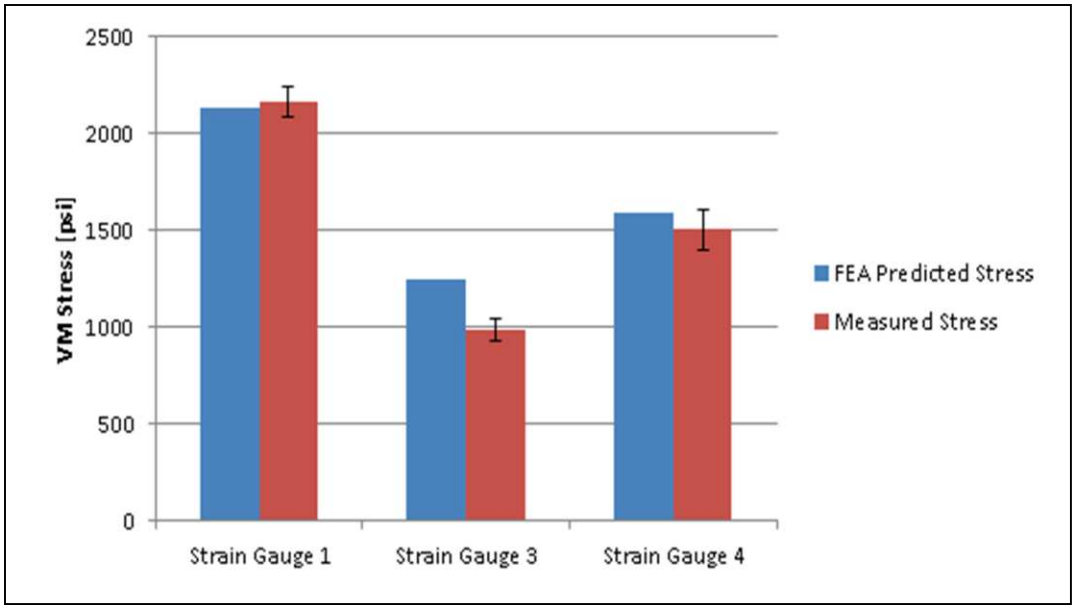

Figure 59: Test Block 1 data comparison

The strain gauge mounting process was very difficult. There was limited space and mobility to mount the strain gauges at the desired locations. When comparing the actual strain gauge location to the point of interest in the FEA models there was a discrepancy. The upper part of the web, above bearing number four, could not be reached as desired. This shortfall is illustrated in Figure 60. The new location's max stress was determined by FEA to be 1150 psi, which was still outside the experimental range. A likely cause of high predicted stresses in FEA models is often due to sharp corners acting as stress concentrators [26]. Seen in Figure 60, the model does not have rounded corner like the actual engine and was identified as a likely cause of the elevated predicted stress inside the crankcase. The original crankcase model was modified to address this concern and reanalyzed in Ansys Workbench. The updated max stress values at the points of interest are given in Table 9.

The updated model did not predict much change at the strain gauge 1, 2, and 5 locations, as they were not close to a sharp corner. But the addition of the rounding along the webs reduced the stresses at strain gauge location 3 and 4. The new predicted stresses for strain gauge 3 fell within the experimental range.

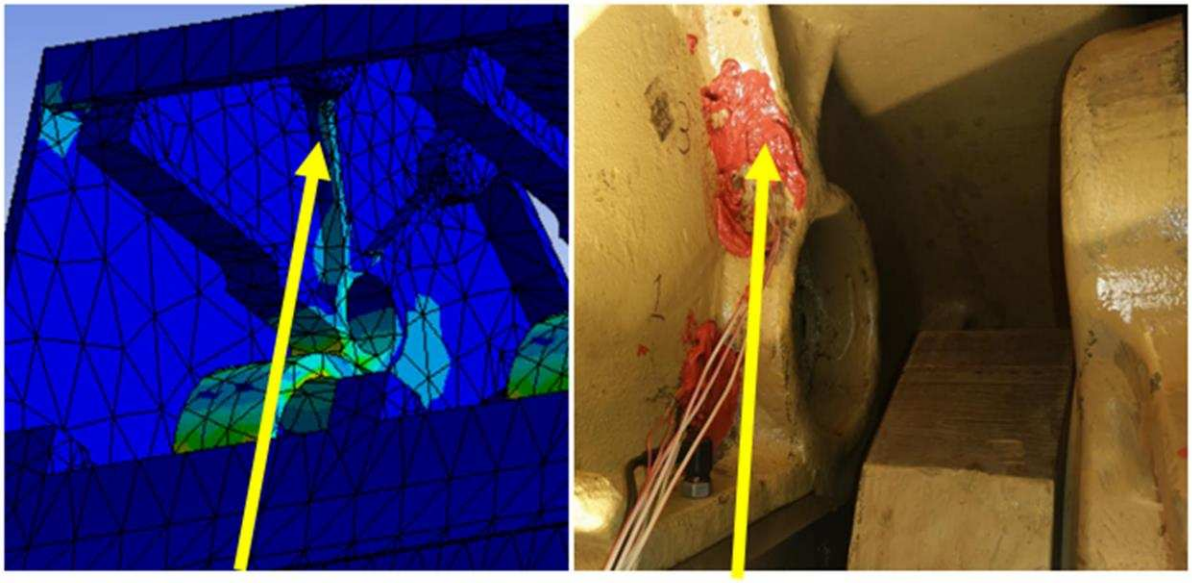

Figure 60: Strain Gauge Mounting Discrepancy

Table 9: Updated Predicted Von-Mises Stress at GMVA Rating

Updated Maximum Predicted VM stress at each Strain Gauge Location				
Strain Gauge 1 [psi]	Strain Gauge 2 [psi]	Strain Gauge 3 [psi]	Strain Gauge 4 [psi]	Strain Gauge 5 [psi]
2134	2017	1016	1543	2134

4.4.1.2 Test Block 2

Prior to test block 2, the strain gauge number 2 was replaced and the redundant strain gauge number 5 was installed. The encoder signal was also corrected to have the voltage data relative to crank angle. The encoder's reset coincided with the TDC of cylinder 1. The TDC's of the cylinder 2 was 62°, cylinder 3 was 180°, and cylinder 4 was 242°. During the first day of block two, strain

gauge number 1 had a short similar to the failure from test block 1. There were no additional strain gauges available to replace the broken strain gauge so for the second day of block two testing strain gauges 2 and 3 were sampled.

Figure 62 displays the average pressure and strain gauge voltage traces for one of the data collections from test block 2. Note the graph does not show the calculate stress but the raw voltage data from data acquisition system but recall, from strain gauge theory, a high voltage change corresponds to a high stress. The greatest voltage changes for "B" and "C" foil of strain gauge two were observed at the peak pressure event for cylinder 3 and the max voltage change for "A" was at peak pressure of cylinder 4. This observation was consistent with the other voltage traces from the test block.

Only data from strain gauges 2 and 3 were analyzed and the results can be seen in Table 10 with a comparison to the updated model in Figure 61. The measured stress from strain gauges 1, 3, and 4 align with the updated FEA model but strain gauge 2 did not. Further model investigation was conducted to identify the cause for this discrepancy.

Upon comparing the FEA model to the LBET it was identified the "airbox" was extruded through the webbing. This caused there to be extra material at the stain gauge 2 location, shown in Figure 63. The "airbox" extrude error was corrected and the FEA model was run again. The updated FEA value for strain gauge was 2268 psi, which was inside the experimental data range.

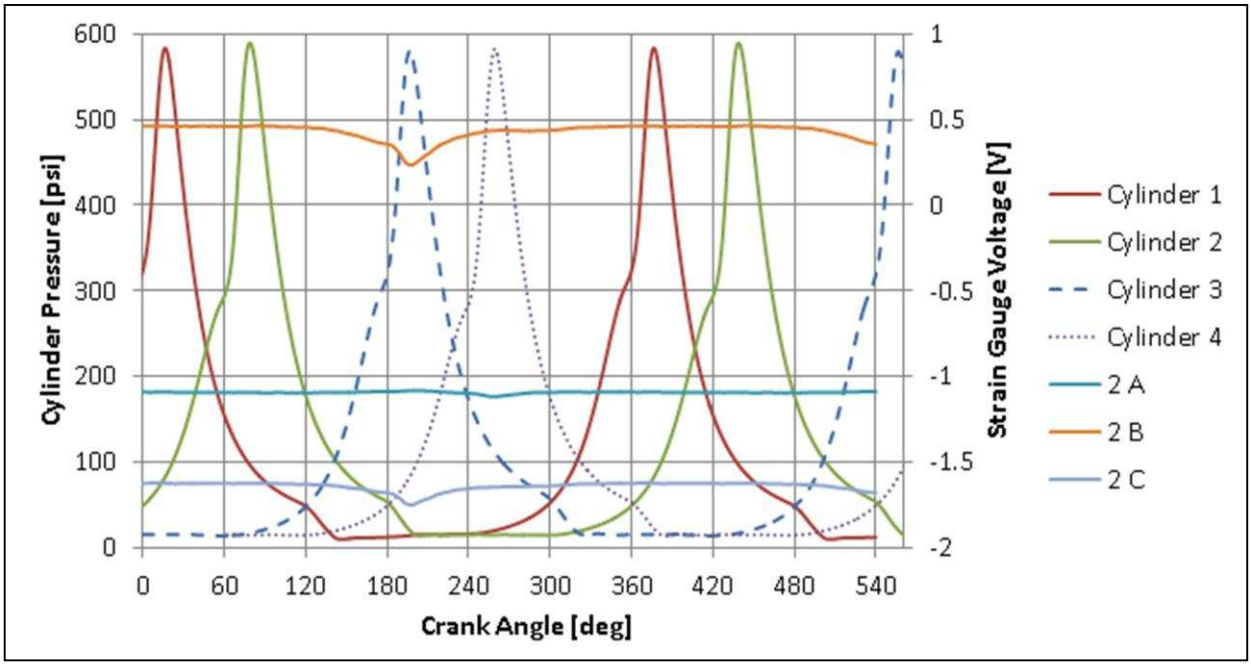

Figure 62: Average Pressure and Voltage Traces from Test Block 2

Table 10: Test Block 2 Max Stress Results

On-Engine Strain Data Test Block 2		
	Strain Gauge 2	Strain Gauge 3
Average	2115	987
Std Dev	86	84

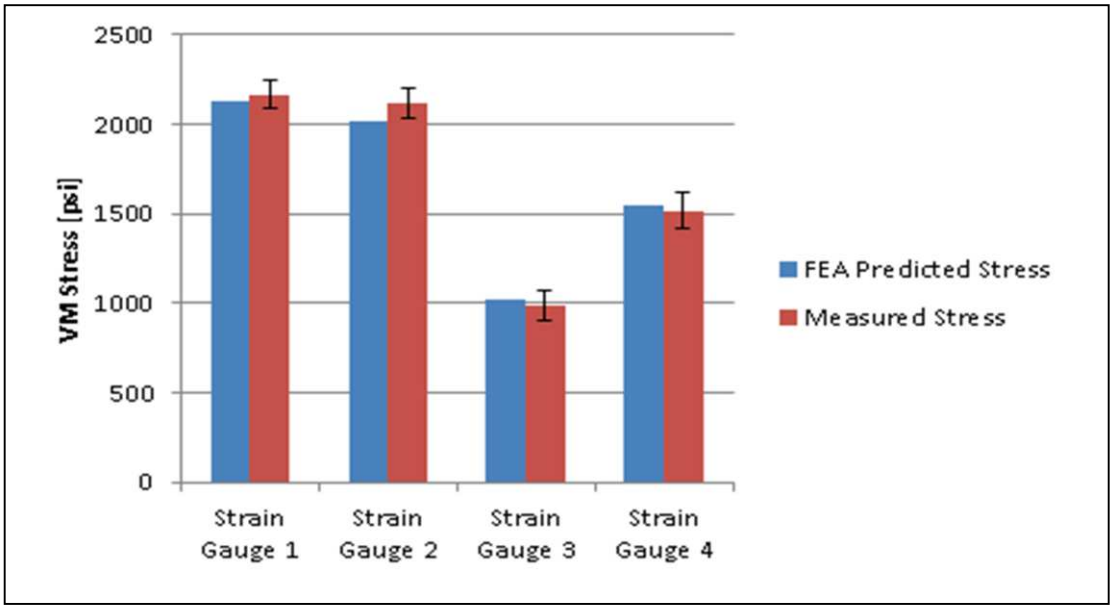

Figure 61: Test Block 2 Data Comparison

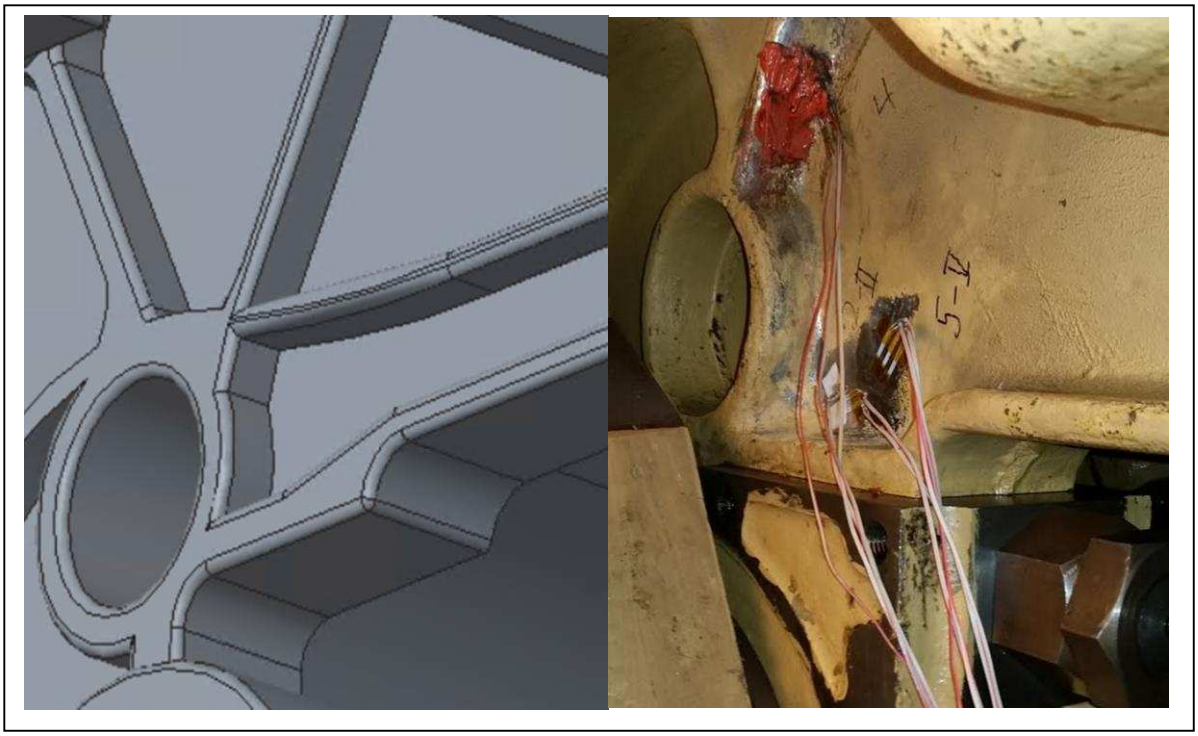

Figure 63: Over Extruded "Airbox"

4.4.1.3 Test Block 3

The intent of collecting nominal data during test block 3 was to confirm the strain gauges 2 and 3 were operating as intended for the cylinder double cylinder deactivation attempt. Strain gauges were operating as expected and were ready for cylinder deactivation data.

The additional collected data was added to the averages for strain gauge 2 and 3. The averages of all the strain data can be seen in Table 11with a comparison to the FEA models in Figure 64. The improved FEA model appears to be an accurate representation of the LBET at the designated points of interest.

Table 11: All On-Engine Strain Data

All On-Engine Strain Data				
	Strain Gauge 1 [psi]	Strain Gauge 2 [psi]	Strain Gauge 3 [psi]	Strain Gauge 4 [psi]
Max Stress	2164	2226	968	1517
Stress Std	77	109	103	104

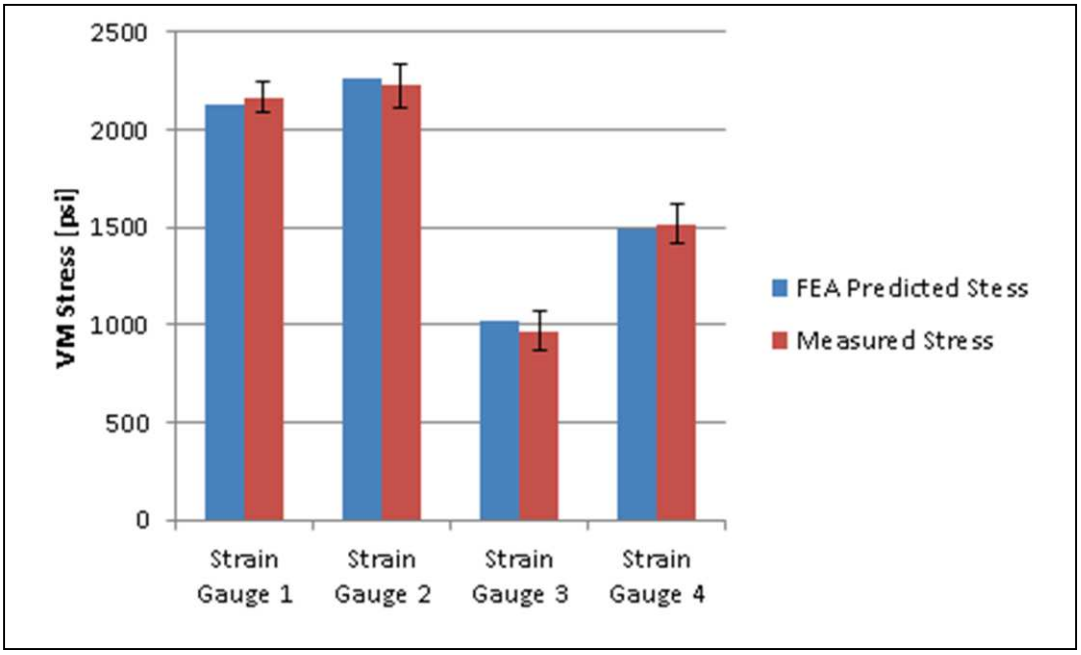

Figure 64: Final Nominal Data Comparison

4.4.2 Single Cylinder Deactivation

The first cylinder deactivation attempt was completed during test block 2, at the conclusion of another project's test day. Recall, deactivating an entire bank of a large bore engine will reduce the output power by 60% [12]. To complete the cylinder deactivation testing the engine was unloaded to ~180 bhp, 40% of 440 bhp. Once the engine stabilized at this operating condition the, fuel to cylinder 1 was cut. The engine had several knock and misfire events in the remaining three cylinders as they began to compensate for cylinder 1 no longer firing. Once the engine combustion

stabilized it was noted that load on the dynamometer was slowly increasing. The LabVIEW code controlling the engine was unable to halt the load increase of the dynamometer. When the fuel was cut to cylinder 3 the engine load at 220 bhp (50%). The load was too great for the LBET to run on only two cylinders and following several misfire and knock events in the active cylinders the LBET shut down.

The water break dynamometer only has inlet flow controls, greatly limiting its ability to regulate loads less than 60%. This was identified as the cause of the steady rise of the load until the engine shut down. Despite the sudden shut down very interesting results were noted.

The magnitude of the stress data at strain gauge location 2 was significantly smaller than the average nominal data collected earlier that day, seen in Table 12. Recall, the high change in voltage measured on the strain gauges was often seen at or near the combustion events of cylinders

Table 12: Test Block 2 Cylinder Deactivation Comparison

On-Engine Strain Data Test Block 2		
	Strain Gauge 2 Nominal [psi]	Strain Gauge 2 Cylinder 1 Deactivation [psi]
Average	2226	930
Std	109	190

3 and 4. The average peak pressure for cylinders 3 and 4 were only ~400 psi compared to the ~600 psi peak pressure from the testing at GMVA rating. A comparison of the voltage traces from 2A for both test cases can be seen in Figure 65. Note how the GMVA voltage trace has a much larger change magnitude than the deactivated case but the rest of the voltage trace was very similar.

The lower peak pressure also lowered the IMEPs of cylinder 3 and 4 from 150 psi and 140 psi to 106 psi and 104 psi, respectively This phenomenon prompted the investigation to determine if there was a correlation between IMEP and measured stress. As the load was steadily increasing

during the cylinder deactivation the IMEP was also increasing. Figure 66 shows the relationship between IMEP and the measured stress at strain gauge 2. The stress data has substantial scatter but there is a bulk upward trend in the data that suggests the IMEP is a major contributing factor the measured stress.

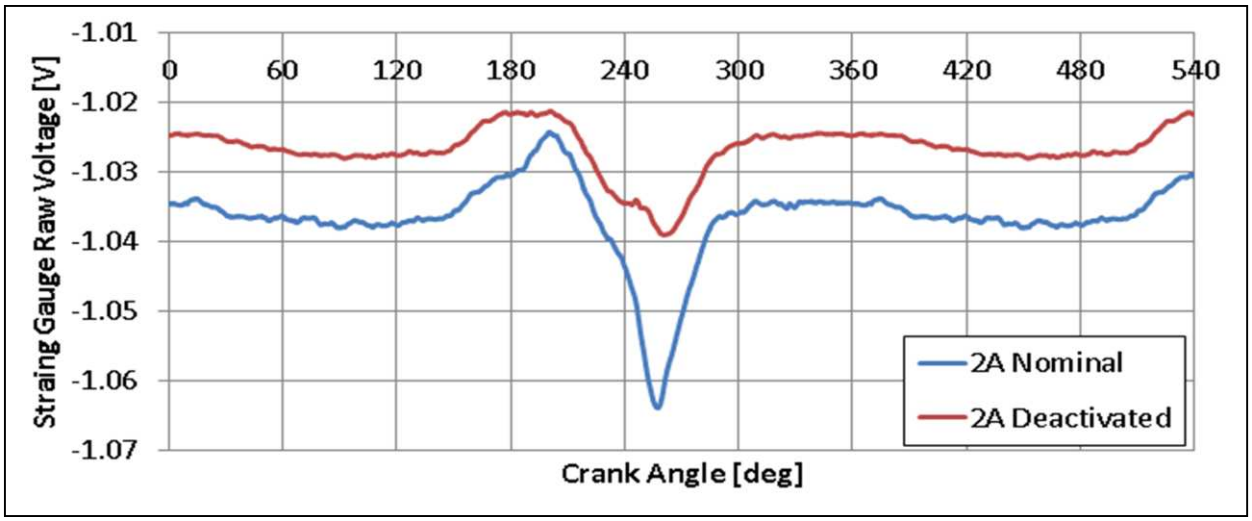

Figure 65: Voltage Trace Comparison between Nominal and Single Cylinder Deactivation

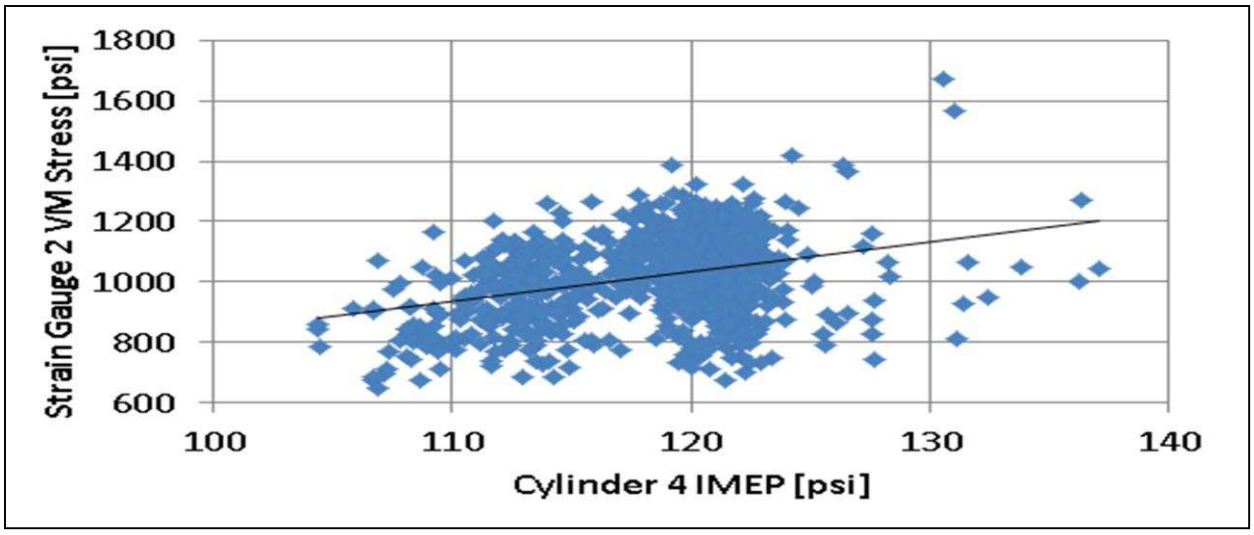

Figure 66: Stress vs Cylinder 4 IMEP

4.4.3 Double Cylinder Deactivation

The double cylinder deactivation attempt was completed during the third test block. Unlike the previous attempt, the engine was started only on cylinders 2 and 4, with the fuel cut to cylinders 1 and 3. This technique was devised to collect as much data as possible before the dynamometer overloaded the engine, ultimately leading to shut down.

When the LBET is started it runs at idle speed, 250 rpm, and the dyno is completely unloaded. Once the LBET was running the load on the dynamometer was slowly increased. The dynamometer load steadily increased until ~50% where the engine shut down like the previous test. Three complete data points were collected on strain gauges 2 and 3. Unfortunately during post processing it was noted strain gauge 3 had a short, despite being in working order the previous day. Each data point had 1,000 combustion cycles for a total of 3,000 points. As expected with increasing load the IMEP of the active cylinders steadily rose. In the first collection the average IMEP of cylinders 2 and 4 were 60 psi and 70 psi, respectively. In the final collection before shutdown the average IMEP of cylinders 2 and 4 were 137 psi and 134 psi, respectively. The average stress also rose with the elevated IMEP measurements. The results can be seen in Table 13. When the LBET shut down due to overload the dynamometer provided 190 bhp of resistance. Meaning if the engine was running on all four cylinders the engine would have provided ~475 bhp, a GMVA rating. As a point of comparison, Figure 67, Figure 68, and Figure 69 illustrate the difference between the GMVA-4 and the GMVA-2 operational conditions.

Table 13: Double Cylinder Deactivation Stress and IMEP Data

	Collection 1	Collection 2	Collection 3
Strain Gauge 2 Avg Stress [psi]	730	744	885
Strain Gauge 2 std [psi]	18	30	68
Cylinder 2 IMEP [psi]	60	90	137
Cylinder 4 IMEP [psi]	70	93	134

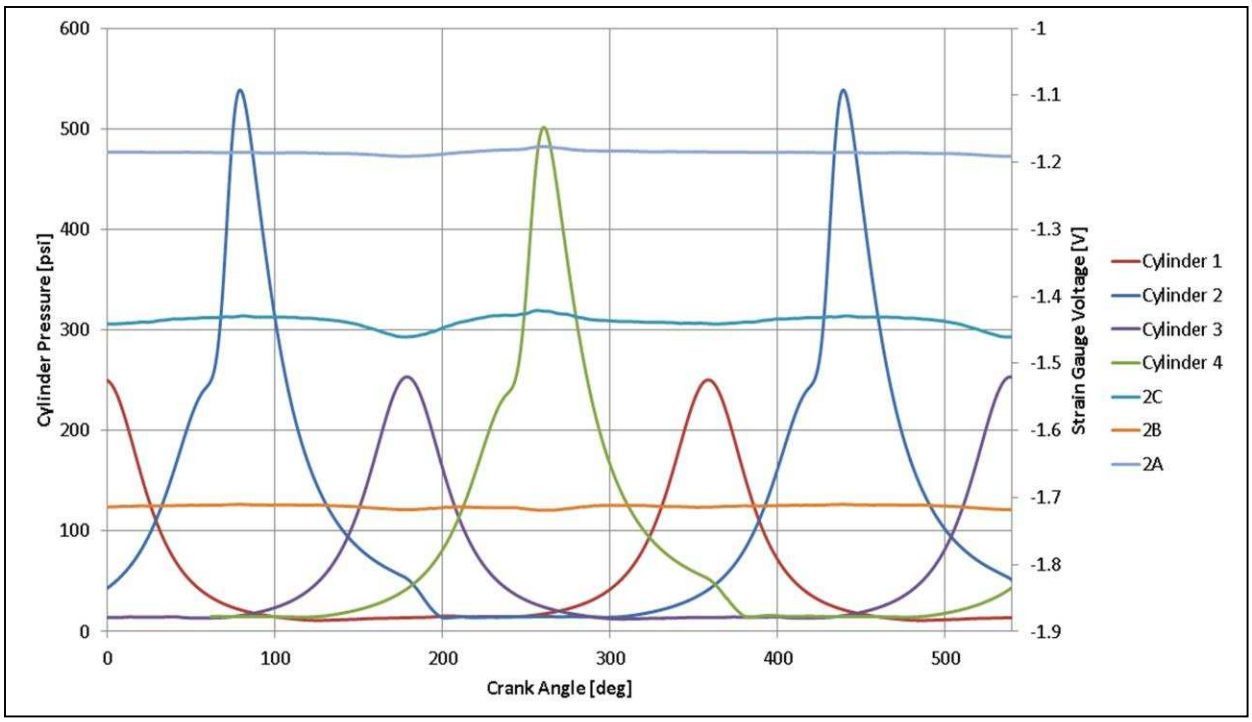

Figure 67: Deactivated Cylinder Traces

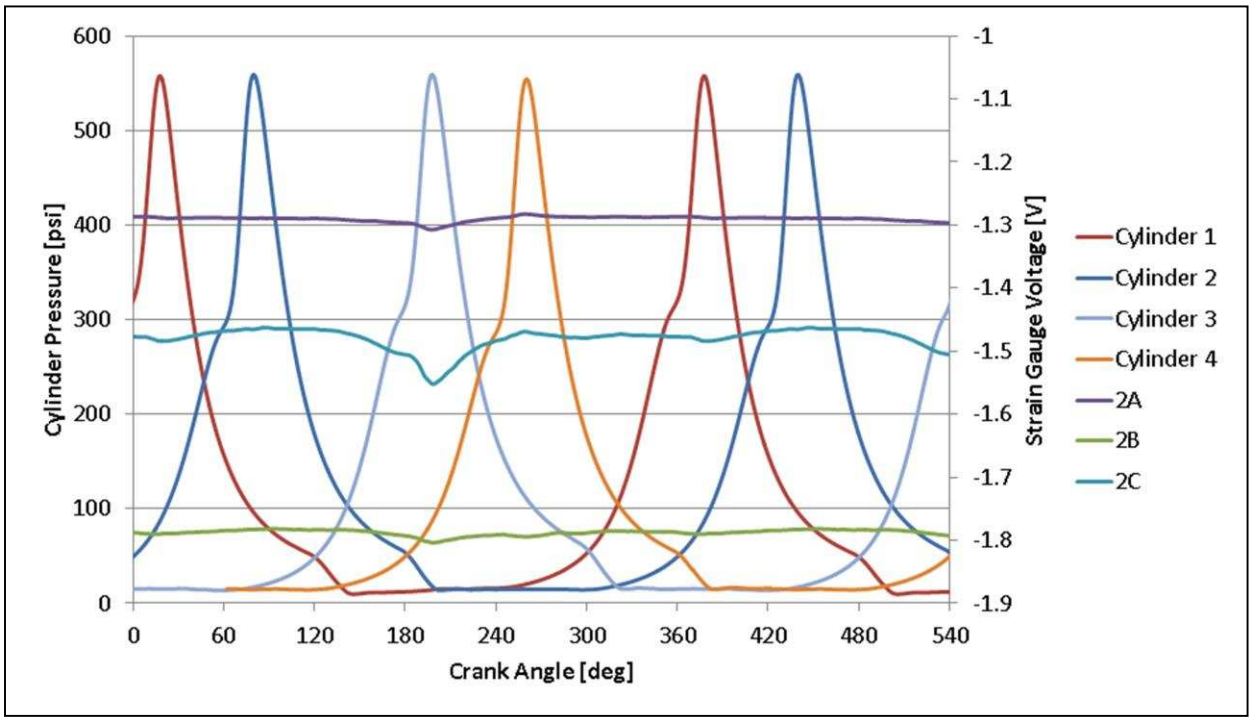

Figure 68: Nominal Cylinder Traces

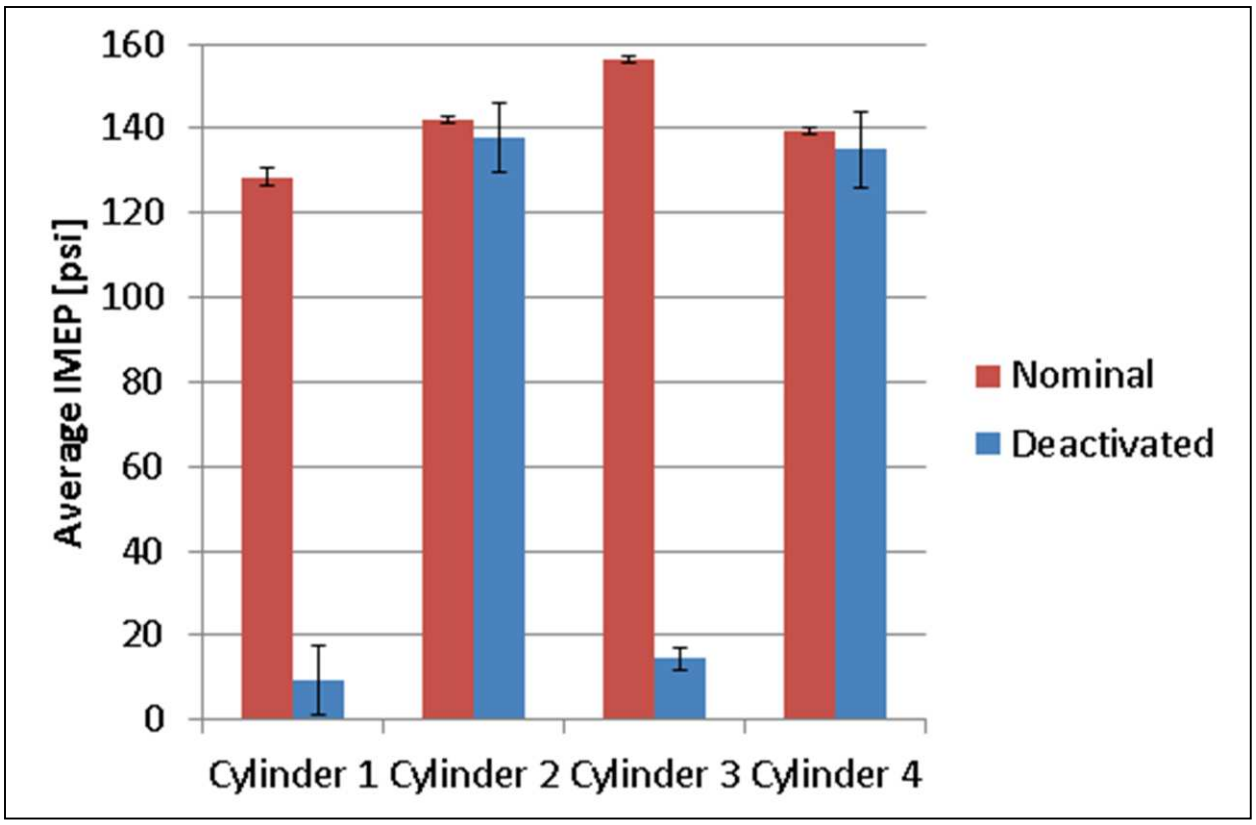

Figure 69: IMEP Comparison between Nominal and Deactivated Conditions with COV as error metric

As can be seen, the deactivated case had a lower average voltage change as compared to the four cylinder case. Consistent with previous testing the greatest voltage change was seen at peak pressure of cylinder 3. Therefor the reduced measured stress for the cylinder deactivation case matches the previous data trends. The frequency of the stresses are outlined in Figure 70. In the frequency histogram, the bulk of the stress events are concentrated near their averages but there is overlap in the high stress events for the deactivated case. Some of the max stress events are at ~92% of the average stress for the nominal case. The cause of the high stress events is not known but cannot be ignored. The high stress events are ~3% of the recorded stresses during the cylinder deactivated case but do not follow a regular pattern of occurrence.

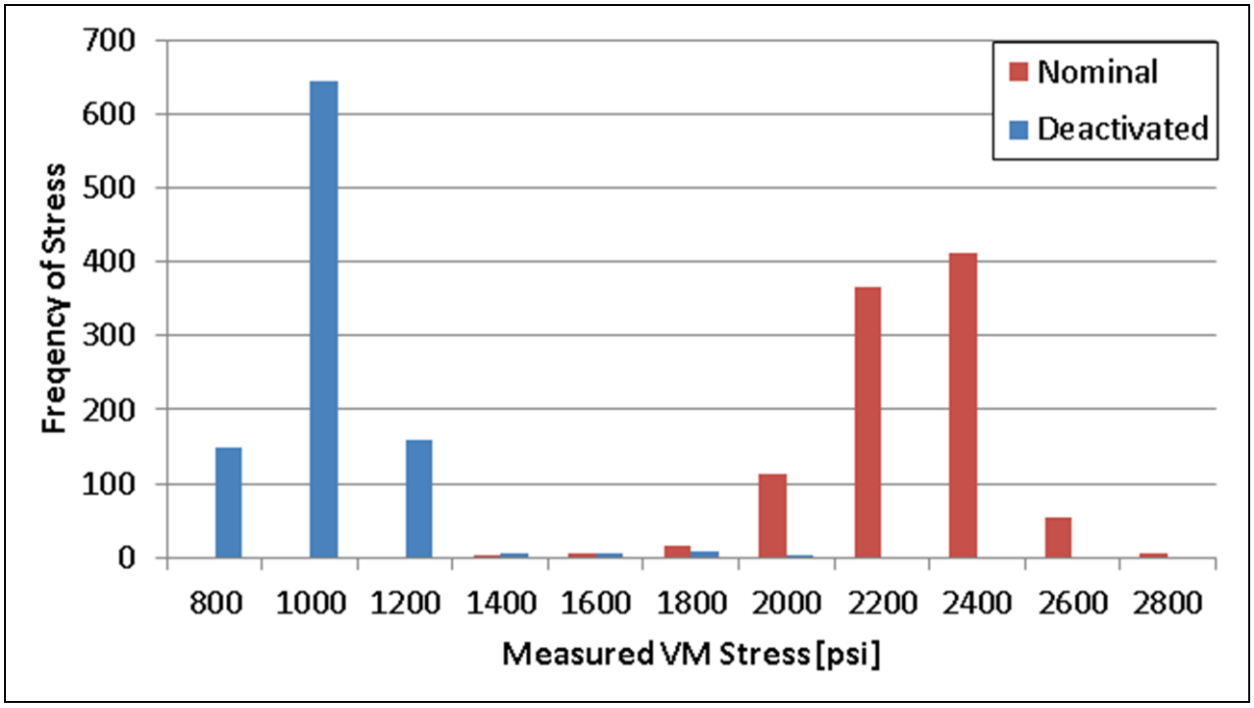

Figure 70: Frequency of Measured Stress at Strain Gauge 2

5 GMVH-2 OPERATION – MODEL EXTRAPOLATION

The FEA model was iterated and validated at the four points of interest for the GMVA operating condition. GMVH-4 operating conditions were inputted in the model to predict the crankcase's response. The GMVH-4 condition was chosen to determine the max expected stress because the experimental data found that the two cylinder operation had high stress events at ~92% of nominal stress. The model predicted the stresses at the points of interest were between 1.6 and 1.9 times greater than the predicted stresses for the GMVA condition, shown in Table 14. This was greater than expected because the peak pressure difference between the two conditions was a ratio of 9:6, or 1.5 times greater and the IMEP's had a ratio of 23:15, or 1.53 time greater. The generated results when then used to determine the worst case scenario stresses during GMVH-2 operation, seen in Table 15, by multiplying the Table 14 results by 0.92.

Recall the fatigue limit of class 25 meehanite was 12 ksi. At the four points of interest, the extrapolated model predicted they would be below the fatigue limit but there were several high stress points that were at or above the limit. The validity of these points cannot be confirmed but

Table 14: GMVH-4 Stress Predictions

			GMVH-4		
Crank Angle	Strain Gauge 1 [psi]	Strain Gauge 2	Strain Gauge 3 [psi]	Strain Gauge 4 [psi]	Max Crankcase Stress [psi]
18.00	1725	2012	631	1202	11729
50.50	2082	2751	1444	996	13412
80.50	2452	3071	1513	899	13542
127.25	1510	2662	2165	909	5306
197.75	3855	3331	2300	2876	9424
229.25	2042	1863	1412	1393	11523
260.50	1784	1828	1031	1160	12031
307.75	2397	3444	464	2183	6461
Max	3855	3444	2300	2876	13542

Table 15: GMVH-2 Stress Predictions

GMVH-2					
Crank Angle	Strain Gauge 1 [psi]	Strain Gauge 2 [psi]	Strain Gauge 3 [psi]	Strain Gauge 4 [psi]	Max Crankcase Stress [psi]
18.00	1587	1851	581	1106	10790
50.50	1916	2531	1328	917	12339
80.50	2255	2825	1392	827	12459
127.25	1390	2449	1992	836	4881
197.75	3547	3065	2116	2646	8670
229.25	1879	1714	1299	1282	10601
260.50	1642	1682	949	1068	11068
307.75	2205	3169	427	2008	5944
Max	3547	3169	2116	2646	12459

should still be considered. Several of the max stress points were in non-accessible parts of the crankcase to install instrumentation or to visually confirm the modeled geometry was correct, an example illustrated in Figure 71. The max stress region was predicted directly above the main crank bearing but there was additional housing on the LBET around the crankcase webbing. The housing around the bearing provided minimal structural support but was needed for proper bearing operation.

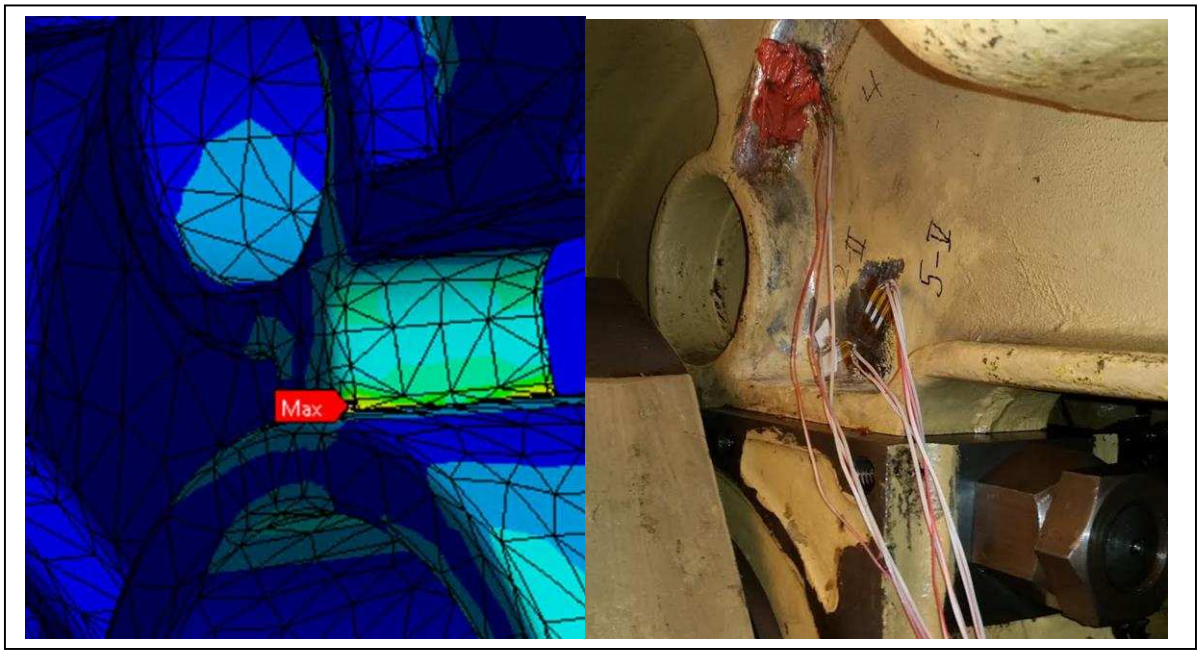

Figure 71: FEA Model Shortfall

Juvinall specifies a method to predict the s-n curve of a material given the fatigue strength and the ultimate tensile strength, seen in Equation 16. S is defined as the failure stress, N is the number of cycles, A and B are unknown constants. The ultimate tensile strength, 26 ksi, is assumed to hold

Equation 16: s-n Curve Prediction [20]

$$\log(S) = A * \log(N) + B$$

true to 10^3 cycle and the fatigue strength, 12 ksi, is assumed to be at 10^6 cycles. The two conditions are used to create two equations and two unknowns leading to A = -0.119 and B = 4.751. The completed equation, seen in Equation 15, is then used to create the approximate s-n curve seen in Figure 72.

Equation 15: Class 25 Meehanite Approximate s-n curve

$$\log(S) = -0.119 * \log(N) + 4.571$$

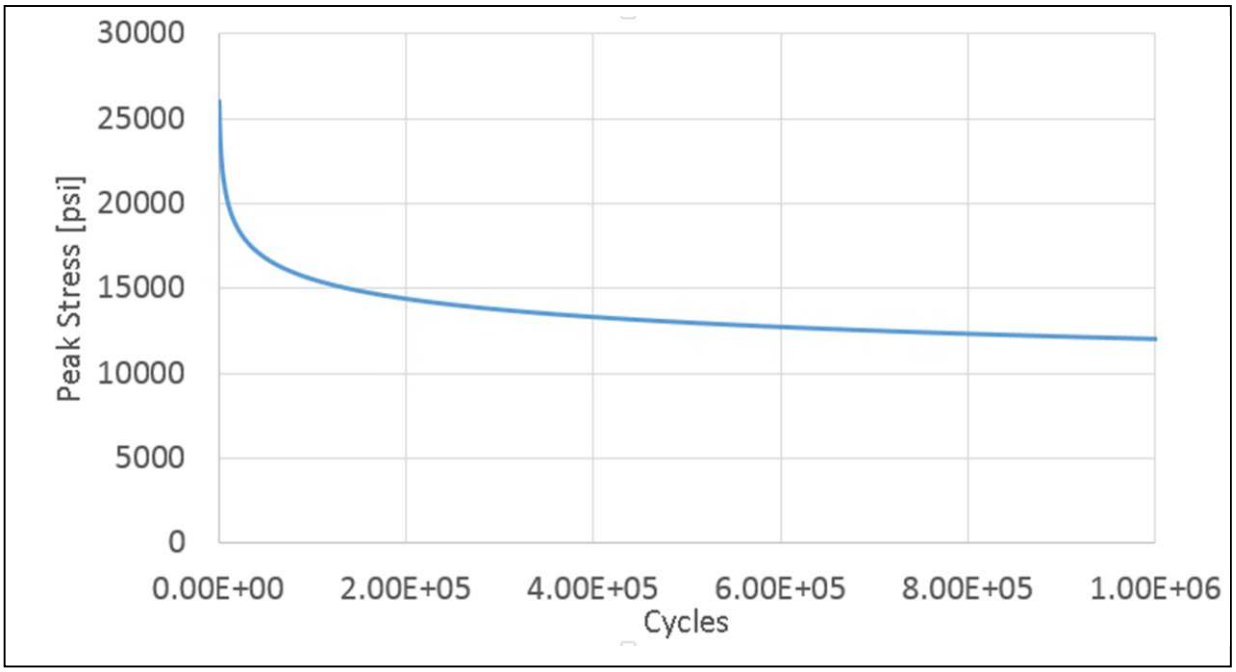

Figure 72: Approximate s-n curve for Class 25 Meehanite

The GMVH-2 model predicted a max frame stress of 12.459 ksi which would lead to a predicted failure at ~7 x 10^5 cycles. Using the experimental finding that high stress events will only be ~3% of cycle, would mean the LBET could operate for 1300 hours before a likely failure. There are several problems with this assumption: first, this assumes the FEA model accurately predicted the high stress regions despite no on-engine validation at those locations, second, the LBET operational history is unknown prior to installation at the EECL, and third, the LBET has not recently been examined for material flaws. Given these concerns, intermediate cases were evaluated between GMVA and GMVH rating.

5.1 INTERMEDIATE TEST CASES

The intermediate cases had peak pressures of 700 psi and 800 psi and used the same bearing force prediction as the previous models. The FEA input conditions can be seen in Table 17 with the results in Table 16.

After examining the intermediate cases it was determined the 800psi peak pressure case would exceed the fatigue limit of class 25 meehanite. But the 700 psi peak pressure case was deemed acceptable. The max stress regions were located in similar locations as the previous models but at lower magnitudes. The LBET would be able to operate with a peak pressure of 700 psi with a two or four active power cylinders, but the two cylinder case would provide an additional safety margin from the fatigue limit. The predicted output powers for the two and four cylinder cases are ~240 bhp and ~600 bhp respectively, slightly below a GMVE rating [6]. The two cylinder predicted output power is still below the lower limit of operation of the dynamometer. To correct this, either outlet flow control will need to be installed or the replacement of the system with an AC motor/generator with a variable frequency drive to regulate load.

Table 16: Intermediate Test Case Results

700 psi Peak Pressure					
Crank Angle	Strain Gauge 1 [psi]	Strain Gauge 2 [psi]	Strain Gauge 3 [psi]	Strain Gauge 4 [psi]	Max Crankcase Stress [psi]
18.00	1291	1659	478	867	10085
50.50	1717	2055	1221	826	11289
80.50	1849	2479	1173	702	11192
127.25	1098	2109	1488	701	4422
197.75	2835	2789	1623	1803	8103
229.25	1702	1494	1057	1055	9596
260.50	1392	1416	803	937	10201
307.75	1947	2484	398	1422	5616
Max	2835	2789	1623	1803	11289
800 psi Peak Pressure					
Crank Angle	Strain Gauge 1 [psi]	Strain Gauge 2 [psi]	Strain Gauge 3 [psi]	Strain Gauge 4 [psi]	Max Crankcase Stress [psi]
18.00	1449	1997	522	1131	11395
50.50	1952	2392	1221	826	12849
80.50	2298	2632	1512	856	13058
127.25	1359	2181	1717	726	5075
197.75	3133	3240	1992	2028	8992
229.25	1953	1779	1157	1113	11387
260.50	1495	1582	909	964	11543
307.75	2065	2652	414	1739	6444
Max	3133	3240	1992	2028	13058

Table 17: Intermediate Test Case Inputs

700 psi Peak Pressure						
Crank Angle [deg]	Cylinder 1 [psi]	Cylinder 2 [psi]	Cylinder 3 [psi]	Cylinder 4 [psi]	Fx1 [lbf]	Fy1 [lbf]
18.00	7.06E+02	1.14E+02	2.24E+01	1.84E+01	1.71E+04	-3.90E+04
50.50	2.91E+02	3.53E+02	2.33E+01	1.87E+01	9.78E+03	-2.06E+04
80.50	1.39E+02	7.06E+02	2.86E+01	2.26E+01	1.38E+04	-5.86E+04
127.25	5.74E+01	1.97E+02	8.71E+01	2.86E+01	6.07E+04	-2.86E+04
197.75	2.24E+01	3.58E+01	6.80E+02	1.29E+02	1.44E+04	-4.89E+04
229.25	2.24E+01	2.12E+01	2.95E+02	3.32E+02	-1.31E+04	-5.32E+04
260.50	2.71E+01	2.25E+01	1.36E+02	7.29E+02	-3.53E+04	-4.63E+04
307.75	8.72E+01	2.24E+01	5.88E+01	1.81E+02	-4.66E+04	-2.26E+04
800 psi Peak Pressure						
Crank Angle [deg]	Cylinder 1 [psi]	Cylinder 2 [psi]	Cylinder 3 [psi]	Cylinder 4 [psi]	Fx1 [lbf]	Fy1 [lbf]
18.00	8.07E+02	1.30E+02	2.56E+01	2.10E+01	1.95E+04	-4.45E+04
50.50	3.32E+02	4.04E+02	2.66E+01	2.14E+01	1.12E+04	-2.36E+04
80.50	1.59E+02	8.07E+02	3.27E+01	2.59E+01	1.58E+04	-6.70E+04
127.25	6.56E+01	2.25E+02	9.95E+01	3.26E+01	6.94E+04	-3.27E+04
197.75	2.56E+01	4.09E+01	7.77E+02	1.47E+02	1.44E+04	-4.95E+04
229.25	2.56E+01	2.42E+01	3.37E+02	3.80E+02	-1.31E+04	-5.37E+04
260.50	3.10E+01	2.57E+01	1.55E+02	8.33E+02	-3.52E+04	-4.68E+04
307.75	9.96E+01	2.56E+01	6.72E+01	2.07E+02	-4.63E+04	-2.47E+04

6 CONCLUSIONS

There are more than 6,000 integral compressor engines in use on US natural gas pipelines, operating 24 hours a day, 365 days a year. Many of these engines have operated continuously for more than 50 years, with little to no modifications. Due to recent emission regulations at the local, state and federal levels much of the aging infrastructure requires retrofit technology to remain within compliance. The Engines and Energy Conversion Laboratory was founded to test these retrofit technologies on its large bore engine testbed. The LBET is a low BMEP Cooper Bessemer GMVTF-4. Newer GMV models, constructed in 1980's, utilize turbocharging to increase the output power, achieving BMEP's nearly double that of the LBET. To expand the lab's testing capability and to reduce the LBET's running cost: material testing, in-depth modeling, and on engine testing was completed to evaluate the feasibility of uprating the LBET to a high BMEP two cylinder engine.

6.1 KEY FINDINGS

6.1.1 Material Testing

Two material samples were removed from the LBET's crankcase and were analyzed for microstructure, density, hardness, and ultimate tensile strength. The literature review specified that Cooper Bessemer GMV's were cast out a meehanite, a specific grade of gray iron, but did not specify the specific grade. The material properties were necessary to accurately model the LBET using FEA.

The crankcase was determined to be cast out of a flake graphite, consistent with common meehanite grades from that era. The density of the material sample was determined using

Archimedes' method finding it had a density of 7.02 g/cc. This density was consistent with the lower strength grades of meehanite. The hardness tests determined the crankcase likely had a hardness between 160 and 180 on the Brinell scale, also consistent with the lower strength grades. Four dogbone samples were machined to determine the ultimate tensile strength of the crankcase material. The samples failed at an average stress of ~24ksi, with no evidence of fatigue failure. Based on the material test results it was determined the LBET crankcase was cast out of a class 25 grade of meehanite, very common for crankcase construction.

6.1.2 Model Construction and Validation

An in-depth three dimensional model of the LBET's crankcase and power cylinders was constructed using a combination of past models, engineering drawings, and on engine measurements. The model was analyzed using FEA to identify potential regions of high stress. The areas of concern were noted to be above the main crank bearing and along the upper engine webbing. These points of interest were instrumented with 3-foil strain gauges to determine if the model findings were valid. The on-engine stress measurements prompted many iterations of the FEA model to be completed. At the conclusion of the modeling iterations, the points of interest were determined to be accurately modeled in the FEA. However, the validity of other high stress region in the crankcase cannot be addressed.

6.1.3 Uprated Operation

The FEA model was extrapolated from a moderate BMEP GMVA conditions to high BMEP GMVH conditions. The model predicted the 4 original points of interest were below the fatigue limit of class 25 meehanite but there were high stress regions above the fatigue limit that were not validated. Suggesting the LBET could not be run as a GMVH-4.

The cylinder deactivated cases measured a lower stress at strain gauge 2 compared to nominal four cylinder operation. The test data noted the greatest change in strain gauge voltage was at the cylinder 3 peak pressure event. When deactivated, cylinder 3's peak pressure dropped from ~600 psi to ~300 psi the average measured stresses dropped by ~50% as well. However, there were several high stress events recorded during cylinder deactivation at ~92% of the nominal average stress condition. The cause of the high stress events was not determined. The high stress events were ~3% of the recorded stresses during the cylinder deactivated case but did not follow a regular pattern of occurrence. Using a general equation to approximate the class 25 meehanite s-n curve, the LBET theoretically could be operated at GMVH-2 conditions for ~1,300 hours before failure but this is not advised because the FEA model was not validated at all locations, the operational history of LBET was not known prior to installation at the EECL, and the crankcase has not had an in-depth inspection.

To avoid premature failure of the LBET, two intermediate uprate conditions were run in the FEA. The intermediate cases assumed a peak pressure of 800 psi and 700 psi. The 800 psi case was determined to have high stress regions above the fatigue limit and deemed unacceptable. The 700 psi predicted the high stress regions to be below the fatigue limit for both four cylinder and two cylinder operation. The 700 psi case equates to roughly a GMVE.

Although the models suggest the LBET could operate as a GMVE-2 an in-depth crankcase examination is suggested to ensure the integrity of the crankcase.

6.2 SHORT COMINGS

6.2.1 Limited Model Validity

The model was validated at four locations in the crankcase, taking several iterations. There were several regions of high stress in the crankcase that could not be practically instrumented or visually inspected, limiting the confirmed validity of the FEA model to the original four points of interest. To address this concern significant strain gauge instrumentation would be required in conjunction with continuous model iteration.

6.2.2 Consistent Strain Gauge Failure

Strain gauge failure was a consistent problem throughout the on-engine testing phase. The likely cause was determined to be insufficient sealant. The sealant material degraded over time in the crankcase, allowing lubrication oil to directly interact with the strain gauge foils, likely leading to shorts. To address this concern a better sealant material would be required as well as additional strain gauges mounted in the crankcase to be redundant.

6.2.3 Poor Load Control during Cylinder Deactivation Experiments

The current water brake dynamometer only has inlet flow control to regulate load. This current method of load control cannot maintain a constant set point below 60% load. This shortfall led to the premature engine shutdown during both cylinder deactivation attempts due to overload. To address this low load concern the addition of outlet flow control is needed to maintain set points below 60% load or the replacement of the system with an AC motor/generator with a variable frequency drive to regulate load.

6.3 DIRECTION FOR FUTURE RESEARCH

6.3.1 Permanent Cylinder Deactivation

Although the LBET cannot safely operate as a GMVH-2 it could still operate as a two cylinder test engine at a GMVE rating. The intent of this research would be to install improved load control at low loads and evaluate the cylinder deactivation techniques. The improved load control could be accomplished either with installing an outlet flow control on the current water brake dynamometer or replacing the system with an AC motor/generator with a variable frequency drive to regulate load.

There are two cylinder deactivation techniques available, remove cylinder 1 and 3 or leave them inside LBET without fuel flow. If the cylinders are removed lube oil system as well the intake and exhaust manifolds would need modification. If the cylinder are left in the crankcase the frictional losses would need to be determined to accurately measure the performance characteristics. At the conclusion of the proposed project, the modified LBET would have to be benchmarked against field engines to determine its ability to test new industry technology.

6.3.2 In-depth Crankcase Inspection

Recall, the LBET could operate at GMVH-2 conditions for 1,300 hours before 7×10^5 high stress cycles occurred, but there were several concerns advising against this. One of the main concerns were the crankcase has not recently been examined for material flaws. Three non-destructive techniques could be used on the LBET to evaluate its current state, liquid penetrant inspection for surface defect detection, and either electromagnetic testing or ultrasonic testing to determine internal flaws outlined by ASM [40]. If there are no signs of fatigue cracks the LBET could operate at elevated conditions above GMVE rating for limited periods.

7 REFERENCES

[1] "U.S. Natural Gas Statisics," 2014. [Online]. Available: http://www.eia.gov/dnav/ng/ng_sum_lsum_dcu_nus_a.htm.

[2] "1985-2013: U.S. Department of Transportation, Pipeline and Hazardous Materials Safety Administration, Office of Pipeline Safety, Annual Report Mileage Summary Statistics." U.S. Department of Transportation, 2014.

[3] N. G. Annual, "Natural Gas Compressor Stations on the Interstate Pipeline Network :," no. November, pp. 1–12, 2007.

[4] U. S. EPA, "AP-42, Compilation of Air Pollutant Emission Factors: Chapter 3.2, Natural Gas-fired Reciprocating Engines," pp. 1–18, 2014.

[5] R. Potter, "Don ' t Retire … ReHire ! The use of Integral Slow Speed Engines As Horsepower Expansion By," no. October, pp. 1–16, 2005.

[6] M. Vernon, "Cooper Bessemer Type GMV Intergral Angle Natural Gas Compressor History," pp. 1–12, 2006.

[7] "Cooper Bessemer GMV Heritage Landmark Award," *ASME Journal of Mechanical Engineering*, 2006. [Online]. Available: https://www.asme.org/getmedia/9e28281d-2403-4337-9ec3-df2251a26ede/240-Cooper-Bessemer-Type-GMV-Integral-Angle-Gas-E.aspx.

[8] G. D. Bourn, F. A. Phillips, and R. E. Harris, "Technologies to Enhance the Operation of Existing Natural Gas Compression Infrastructure," 2005.

[9] K. Evan, "Supercharger Installation." Colorado State University, Fort Collins, CO.

[10] P. Jackson, M. D. and Jones, "Deactivating Compressor Engine Cylinders Saves Fuel." The Oil and Gas Journal, 1976.

[11] B. W. and G. Hutcherson, “Relative Performance of High-Pressure Fuel Gas Delivery - 1997 GMC.pdf.” .

[12] B. F. Smalley, A. J., and Vinyard, S., and Evans, “Power Cylinder Deactivation for Reduced Fuel Consumption Under Part Load,” San Antonio, Texas, 1986.

[13] M. Wilcutts, J. Switkes, M. Shost, and A. Tripathi, “Design and Benefits of Dynamic Skip Fire Strategies for Cylinder Deactivated Engines,” Apr. 2013.

[14] G. Hutcherson, R. Potter, R. Schoonover, and B. Willson, “Evaluation of Low Emission Technologies for Large Bore Natural Gas Engines Prepared for Tenneco Gas Testing conducted by :,” no. July 1995.

[15] J. Adair, D. Olsen, and A. Kirkpatrick, “Exhaust tuning of large-bore, multiculinder, two-stroke, natural gas enigines.pdf,” *Int. J. Engine Res.*, vol. 131, no. 7, 2006.

[16] “GMV-TF Natural Gas Pipeline Compressor User’s Manual,” Mt. Vernon, Ohio.

[17] R. W. Harvey, “GMV-6 Torsional Study,” Maysville, OK, 1989.

[18] “U.S. Crude Oil and Natural Gas Proved Reserves,” 2014. [Online]. Available: http://www.eia.gov/naturalgas/crudeoilreserves/.

[19] F. G. Engineering and C. Applications, “Meehanite® metal selection guide.”

[20] R. C. Juvinall and K. M. Marshek, *Fundamentals of Machine Component Design*, 5th ed. Danvers, MA: John Wiley and Sons, 2012.

[21] D. Schmitt and R. Baker, “Systematic Engine Uprate Technology Development and Deployment for Pipeline Compressor Engines through Increased Torque (November 2004 - October 2005) Prepared by :,” Colorado State University, 2005.

[22] D. Schmitt, “Frame Stress and Crankshaft Modal Analysis on Large Bore Natural Gas Engines,”

Colorado State University, 2005.

[23] K. Gupta and J. Meek, *Finite Element Multidisciplinary Analysis*, 2nd ed. USA: American Institute of Aeronautics and Astronautics, 2003.

[24] R. Cook, *Finite Element Modeling for Stress Analysis*, 1st ed. New York: John Wiley and Sons, 1995.

[25] K. H. Huebner, D. Dewhirst, L., D. E. Smith, and T. G. Byrom, *The Finite Element Method for Engineers*, 4th ed. New York: John Wiley and Sons, 2001.

[26] R. Cook, D. Malkus, M. Plesha, and R. Witt, *Concepts and Applications of Finite Element Analysis, 4th Edition*, 4th ed. New York: John Wiley and Sons, 2001.

[27] A. Becker, *Introductory Guide to Finite Element Analysis*. New York: ASME, 2004.

[28] K. Geels, "Metallographic and Materialographic Specimen Preparation, Light Microscopy, Image Analysis and Hardness Testing"." ASTM International, West Conshohocken, PA, 2007.

[29] G. Vander Voort, *Metallography: Principles and Practice*. Materials Park, Ohio: ASM International, 1984.

[30] ASTM Int., "Standard Test Methods for Tension Testing of Metallic Materials 1," *Astm*, no. C, pp. 1–27, 2009.

[31] R. W. Hertzberg, *Deformation and Fracture Mechanics of Engineering Materials*, 4th ed. Danvers, MA: John Wiley and Sons, 1996.

[32] L. Fisher, *Selection of Engineering Materials and Adhesives*, 1st ed. Danves, MA: Taylor Francis Group, 2005.

[33] G. Aggen, "ASM Handbook Online," *ASM*, Mar-1995. [Online]. Available: http://products.asminternational.org/hbk/index.jsp.

[34] ASTM E18-15, “Standard Test Methods for Rockwell Hardness of Metallic Materials,” *ASTM Int.*, pp. 1–38, 2015.

[35] “Reynold French Cooper Bessemer GMV Repairs,” Reynolds French and Company, Tulsa, OK, 2010.

[36] B. A. Szabo and I. Babuška, “Finite Element Analysis,” p. 368, 1991.

[37] R. Norton, *Machine Design: An Integraed Approach*, 2nd ed. River, NJ: Prentice-Hall, 2000.

[38] G. D. Bourn, F. A. Phillips, and R. E. Harris, “Technologies to Enhance the Operation of Existing Natural Gas Compression Infrastructure,” Morgantown, WV.

[39] “Measuring Strain with Strain Gages,” *National Instruments*, 2016. [Online]. Available: http://www.ni.com/white-paper/3642/en/. [Accessed: 20-Jun-2003].

[40] C. G. Goetzel, *Nondestructive Inspection and Quality Control*, 11th ed. Metals Park, Ohio: American Society for Metals, 1976.

8 APPENDIX

8.1 APPENDIX A MEEHANITE METAL SELECTION GUIDE

MEEHANITE® METAL SELECTION GUIDE

For General Engineering, Heat, Wear and Corrosion Applications

The Meehanite Process Makes A Difference

Meehanite® is the registered tradename of a family of cast ferrous materials manufactured under rigid metallurgical control so that their properties meet established engineering specifications.

The dense, fine grain structure of Meehanite metal which assures casting solidity and uniform physical properties regardless of mass or section is achieved by the use of well established Meehanite control procedures.

The Meehanite Process

This process involves a number of patented features seeking to control and produce the desired graphite distribution and the desired matrix structure in the casting. It depends primarily on the establishment of a melt of desired degree of undercooling often referred to as constitution and the controlled nucleation of this melt, usually by means of alkaline earth silicide additions. It requires very careful selection of raw materials, meticulous process controls and a very thorough knowledge of the foundry behavior of cast iron.

Figure 1. shows how the process is used for flake graphite type irons. Control principles for producing nodular types of graphite are essentially the same, except the process is controlled by wedge tests at three stages of treatment instead of two and specially designed alloys are used to assure full nodularity, even in large, heavy casting sections. (Note Fig. 2.)

The Meehanite process involves the use of standard procedures in all phases of casting manufacture including gating and risering techniques, sand control testing methods and many specialized molding procedures. It eliminates guesswork, thereby resulting in an engineering product of high integrity and reliability.

Figure 1. Meehanite Process For Flake Graphite Irons

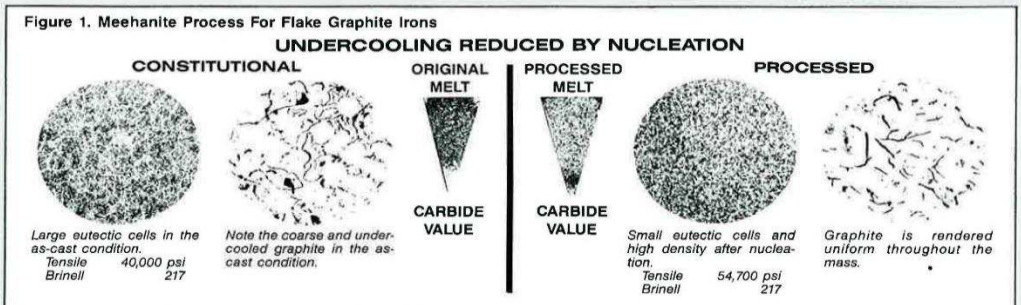

Large eutectic cells in the as-cast condition.
Tensile 40,000 psi
Brinell 217

Note the coarse and undercooled graphite in the as-cast condition.

Small eutectic cells and high density after nucleation.
Tensile 54,700 psi
Brinell 217

Graphite is rendered uniform throughout the mass.

Figure 2. Meehanite Process For Nodular Graphite Irons

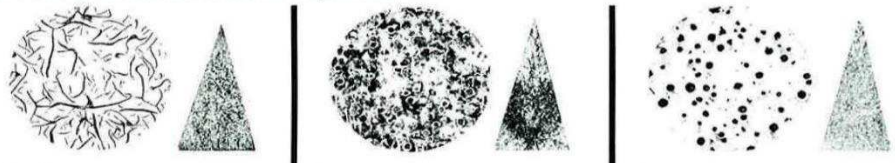

Step 1
Microstructure of soft base Meehanite metal with graphite in flake form selected for purity.

Step 2
Same metal treated with patented Meehanite alloy to produce spheroidal graphite. Wedge is related to casting section to be poured.

Step 3
Third treatment graphitizer metastable carbides. Removes impurities.

For General Engineering, Heat, Wear and Corrosion Applications

Meehanite Metal Types

While the Meehanite process is a closely integrated procedure and will produce a truly quality casting, it is necessary for the engineer to have at his disposal exact figures on the physical and mechanical properties of Meehanite Metal so that he may design with confidence.

For this reason, Meehanite Metal has conveniently been divided into a number of broad type classifications each with its typical properties which enables the engineer to select that type of metal most suited to his particular application.

On the basis of use, the following broad categories apply:

1. General Engineering	Prefix G
2. Wear Resisting	Prefix W
3. Heat Resisting	Prefix H
4. Corrosion Resisting	Prefix C

These categories relate to the end use of the casting and are further sub-divided on the basis of metallurgical structure and property values.

General Engineering Types

This Meehnaite Metal series is classified into flake graphite metals designated by the prefix G and nodular graphite metals designated by the prefix S.

The G, or flake graphite, metals are subdivided according to the tensile strength because this is the most convenient method. This method of division is used even through the engineer may be more interested in specific properties other than tensile strength.

Tensile strength is given in minimum values, but it should be realized that Meehanite Metal G may be produced to any specific minimum value either exactly cooresponding to any specific type or to values that may fall exactly in between designated types.

In short, all properties show a gradual transition from the highest tensile value to the lowest tensile value and are separated into various types only for the purpose of specification.

Flake Graphite "G" Types

Type GM 60—flake graphite, sorbo pearlitic matrix or tempered martensite if heat treated.
Type GA 50—flake graphite, pearlitic matrix.
Type GC 40—flake graphite, pearlitic matrix.
Type GE 30—flake graphite, pearlitic matrix.
Type GF20—flake graphite, ferritic/pearlitic matrix.
Type AQ—flake graphite, pearlitic/bainitic matrix.

The sub-numerals, 60, 50, 40 etc., indicate the PSI units on equivalent standard test bars for each type.

For example:

GA 50 means type GM metal has approximate tensile strength 50,000 psi.

Nodular Graphite "S" Types (Ductliron®).

Sub-division in this series again is for specification convenience. Specific property values of any value within the ranges given may also be provided.

Type SF 60—nodular graphite, ferritic matrix.
Type SP 80—nodular graphite, peralitic/ferritic matrix.
Type SH 100—nodular graphite, pearlitic matrix, or tempered martensite if heat treated.
Type AQS—nodular graphite, pearlitic/bainitic matrix.

Wear Resisting Types (Almanite®).

This series produced primarily for wear resistance while having specific mechanical properties is broadly classified according to metallurgical structures which, in turn, determines the wear resistance.

These metals may contain free carbon as graphite or as carbides or both. Those containing carbides as the major properties of free carbon are white irons.

Subdivisions are:

Type W 1—carbidic, pearlitic matrix.
Type W 2—carbidic, martensitic matrix.
Type W 4—carbidic, austenitic matrix.
Type WS—nodular graphite, bainitic matrix.
Type WSH—nodular graphite, austenitic matrix.

Austempered Ductile Iron Types (Meehanite ADI)

This series offers a unique combination of high strength properties and excellent machinability. It differs from all unalloyed or lightly alloyed common carbon steels and cast irons in that its microstructure does not contain any hard and brittle iron carbide. The basic components of Meehanite ADI types are ferrite, retained austenite and nodular graphite.

The classification is based on median hardness value:

Type K295 Type K325 Type K405

Heat Resisting Types

While even the General Engineering irons do have some good heat resisting properties, the heat resisting types of Meehanite are specifically produced to meet a wide range of high temperature service conditions.

Sub-division is on the basis of type of application, but is characterized by structure, thus:

Type HR—carbidic/pearlitic (heat with wear).
Type HS—nodular graphite, ferritic. (temperature up to 1800°F (981°C).
Type HSV—nodular graphite, ferritic/pearlitic.
Type HE—flake graphite, pearlitic (heat shock).

Corrosion Resisting Types

This series is sub-divided very broadly according to structure, but composition may be varied considerably to suit exact conditions of service. This should be done on the basis of consultation with your casting supplier.

The austenitic nickel types CR and CRS may be modified to meet all standard engineering society specifications for this type of material.

Type CC—flake graphite, pearlitic.
Type CR—flake graphite, nickel/austenitic.
Type CRS—nodular graphite, nickel austenitic.
Type CHS—nodular graphite, ferritic.

General Engineering Applications

Type AQ is a wear and abrasion resisting iron that is readily machinable as-cast but may be "air hardened" after machining with minimum risk of cracking or distortion. Type AQ is easily heat treated and locally hardened. Recommended for dies, punches, spinning mandrels and other hard wearing applications.

Type GM-60 possesses exceptionally high physical properties, including good impact strength and shock resistance—responds well to heat treatment and surface hardening. Type GM machines to a very fine finish and is recommended for heavy section castings where pressure tightness is required.

Type GA-50 combines high strength, toughness, wear resistance and damping capacity with excellent machinability. Responds well to heat treatment, local and surface hardening.

Type GC-40 combines good strength with low coefficient of friction and self lubricating properties. It is easily machinable with a fine, dense, close grain structure. Recommended for heavy brake drums and pressure castings up to 2½" thick.

Type GE-30 combines improved strength and solidity with higher machining feeds and speeds than ordinary gray iron.

Type GF-20 designed principally for high machinability and is used where ultimate strength is not an important factor.

Table 1 **Meehanite Flake Graphite Types**

PROPERTY	TYPE AQ	TYPE GM-60	TYPE GA-50	TYPE GC-40	TYPE GE-30	TYPE GF-20
Tensile Strength—psi	50/65,000	60,000	50,000	40,000	30,000	20,000
Proportional Limit—psi .01% permanent set	25,000	25,000	22,000	14,000	11,500	9,500
Modulus of Elasticity—psi	22,000,000	21,500,000	20,000,000	16,500,000	13,000,000	9,000,000
Modulus of Rigidity—psi	9,500,000	9,500,000	8,750,000	7,750,000	5,500,000	4,000,000
Poisson's Ratio	0.33	0.33	0.32	0.30	0.27	0.24
Modulus of Rupture—psi	93,000	93,000	90,000	80,000	61,000	41,000
Compression Strength—psi	200,000	200,000	180,000	150,000	120,000	90,000
Fatigue Strength—psi	30,000	25,000	22,000	17,500	13,500	11,000
Shear Strength—psi		53,000	50,000	40,000	30,000	21,550
Single Impact—Izod .798" Dia. Unnotched Bar	30-40	30-40	25-35	12-20	6-12	4-9
Brinell Hardness (Nominal)	280-550	230	220	180	up to 160	150
Machinability Rating (Dalcher)	52	50	48	47	38	30
Thermal Conductivity 50-450°F. BTU/Hr/Sq. Ft./Inch Thickenss/°F		355	350	325	290	—
Coefficient of Thermal Expansion Per °F. from 100° to 1000°F.	.00000675	.00000705	.00000720	.00000760	.00000790	—
Specific Gravity	7.34	7.34	7.31	7.25	7.06	6.80
Solid Contraction (Patternmaker's Shrinkage)	5/32"-6/32" per ft. (1.3-1.5%)	5/32"-6/32" per ft. (1.3-1.5%)	5/32"-6/32" per ft. (1.3-1.5%)	4/32"-5/32" per ft. (1.0-1.3%)	1/10"-1/8" per ft. (0.8-1.0%)	1/10" (0.8%)

General Engineering Applications

Type SP-80 possesses in the as-cast condition more than twice the strength of conventional gray cast iron in combination with exceptional toughness. It has a predominantly pearlitic structure, is readily machinable and responds easily to surface hardening by chill casting or by flame or electric induction heat treatment.

Type SH-100 is characterized by its exceptional hardenability. It is particularly suited where high strengths are desired in relatively heavy casting sections. In the as-cast condition it has a pearlitic structure. Any hardness value may be obtained, ranging from that of a free machinable iron to that of the fully hardened tool steel. SH-100 oil quenched from 1650°F and drawn at 750°F results in a good combination of hardness, strength and toughness.

Type SF-60 possesses high ductility and exceptional resistance to shock. It has maximum toughness and machinability. Its structure is essentially ferritic and not readily flame hardened.

Type AQS is an air hardening metal possessing high strength, toughness and hardness. It may be fully air quenched throughout casting section after machining to a wide range of strength and hardness values that are uniform with little or no risk of cracking or distortion. It has high endurance strength and provides an excellent degree of abrasion resistance.

Table 2 **Meehanite Nodular Graphite Types (Ductliron®).**

PROPERTY	TYPE SP-80	TYPE SH-100	TYPE SF-60	TYPE AQS
Tensile Strength—psi	80/100,000	100/170,000	>60,000	80/180,000
Yield Strength—psi	60/75,000	70/130,000	>45,000	70/140,000
Modules of Elasticity (tension) EX 10^6	25	24	23	25
Elongation %	3%—10%	1%—5%	15%—25%	1%—3%
Endurance Limit (unnotched)	39,000	43,000	30,000	53,000
Endurance Ratio (unnotched) (45° notch)	0.49 0.35	0.33 0.25	0.50 0.35	0.33
Poisson's Ratio	0.37	0.37	0.32	
Brinell Hardness (Nominal)	200	207/600	161	225/500
Impact Strength—Charpy Ft. lbs. 10 mm Square bar "V" notch	1-5	1-3	7-15	1-3
Specific Gravity	7.20	7.22	7.18	
Solid Contraction Patternmaker's Shrinkage	5/32" per ft. 1.3%	5/32" per ft. 1.3%	1/8" per ft. 1.0%	5/32" per ft. 1.3%
Specifications Met	ASTM-A48-83	ASTM-A536-84	ASME SA395 MIL-1-24137 Ships ASTM A395-80 ASTM-A536-84	

Heavy-Duty Applications

Type K-295 and K-325 are used for applications such as gears requiring high contact rolling and tooth bending fatigue properties. Also possess high fracture toughness impact strength. *K-405* is for applications involving wear and requiring high tensile and endurance limit. All types are useful to meet high mechanical properties with a 10% weight savings compared to steel. Excellent founding properties enable more accurate castings with saving in machine stock required. Damping capacity and notch sensitivity are superior to steel castings and forgings. Self-lubricating properties of all types make them ideal for wear conditions involving minimal lubrication.

Table 3 **Meehanite ADI Types (Austempered Ductile Iron)**

PROPERTY	TYPE K-295	TYPE K-325	TYPE K-405
Tensile Strength—psi	130,000	145,000	175,000
Yield Strength—psi	98,000	112,000	140,000
Endurance Limit Unnotched Notched	 63 39	 66 47	 74 51
Elongation—%	8-12	5-8	2-5
Hardness (Approx.)	280-310	300-350	380-430

Wear Resisting Applications

Type W is a series of austenitic-martensitic white irons characterized by high hardness and relatively good impact strength. Type W has a pearlitic matrix; Type W2 has a martensitic matrix; Type W4 is highly alloyed to provide an austenitic matrix in the as-cast condition which may be further modified to give a martensitic matrix by heat treatment or by freezing.

Type WS is a hard wearing martensitic iron with exceptional impact strength. . . not readily machinable. . . work hardens in service to high hardness values. Type WS is recommended for crusher jaws, impact hammers, pulverizers, etc.

Type WSH is an austenitic nodular iron possessing superior tensile strength, toughness and ability to work harden under conditions of severe pounding impact. It is extremely difficult to machine. Recommended for crusher liners, hammers, grinding balls, etc.

Table 4 **Meehanite Wear and Abrasion Resisting Types (Almanite®).**

PROPERTY	TYPE W1	TYPE W2	TYPE W4	TYPE WS	TYPE WSH
Tensile Strength—psi	50/60,000	50/60,000	60/80,000	60/80,000	>100,000
Yield Strength—psi				50/65,000	75,000
Modules of Elasticity—psi	26,000,000	26,000,000		24,000,000	24,000,000
Elongation %				2-4	4-10
Brinell Hardness	500/600	500-600	400/700	400/525	350/500
Izod Impact 1.2" bar unnotched ft. lbs.	30-50	40-60	40-70	up to 180	up to 120

Heat Resisting Applications

Type HS compares very favorably from a strength standpoint with any heat resisting metal and is recommended for applications at temperatures up to 1800°F under both conditions of cyclic and continuous heating without thermal shock. Compositional adjustments are made to suit the exact service conditiions. It machines easily and provides maximum resistance to scaling and growth. Recommended for blast furnace parts, hot gas valves, doors, frames, annealing pots.

Type HSV is an iron developed essentially for engineering parts that are subjected to long continuous heating at temperatures up to 1600°F. It has been designed to have the maximum load bearing ability.

Type HR is a strong, dense iron of high rigidity and excellent resistance to scaling under most conditions. It is non-growing for temperatures up to 1350°F and possesses good load carrying ability. Recommended for service conditions without thermal shock such as furnace parts, retorts, tube supports, etc.

Type HE is a freely machinable material in the as-cast condition. Withstands rapid heating and cooling without premature failure, offers good dimensional stability and a good range of strength properties. Recommended for ingot molds, slag pots, hot plates, and parts heated rapidly by a naked flame.

Table 5 **Meehanite Heat Resisting Types**

PROPERTY	TYPE HS	TYPE HSV	TYPE HR	TYPE HE
Tensile Strength—psi	60/100,000	100/120,000	40,000	25,000
Modules of Elasticity—psi	23,000,000	50/80,000,000	21,000,000	10,000,000
Elongation %	2-10	2-10		
Brinell Hardness (Nominal)	200	200	300 or over	170
Thermal Conductivity 50°/450°F. BUT/Hr./Sq. Ft./Inch Thickness		278	360	298
Coefficient of Thermal Expansion Per °F from 100° to 1000°F	.00000700	.00000674	.00000743	.00000666
Machinability	Good	Good	Difficult	Good

Corrosion Applications

Type CC is a general utility material providing good corrosive resistance. It can be used for slightly acid solutions, alkali solutions at temperatures up to 150°F. and concentrated sulphuric acid at temperatures up to 250°F.

Type CR is an austenitic material especially designed to meet a wide variety of corrosion, wear and heat applications. It has flake graphite and chemical analysis conforming to ASTM Specification A-436-61T.

Type CRS is an austenitic material with graphite in the nodular form. It conforms to ASTM designation A439-60T and provides much higher strength than type CR with excellent resistance to corrosion, wear and heat.

Both type CR and CRS are recommended for components which involve handling acid and alkali solution at temperatures up to 1300°F; for abrasive slurries, salt water and other heat and wear applications with or without corrosive media.

Type CHS is a higher strength material with good shock resistance. Compositional adjustments are made to suit exact service requirements. Recommended for use for components subjected to concentrated sulphuric acid or oleum.

Table 6 **Meehanite Heat Resisting Types**

PROPERTY	TYPE CC	TYPE CR	TYPE CRS	TYPE CHS
Tensile Strength—psi	40,000	25,000	58,000	60/100,000
Brinell Hardness	200	131/183	139/202	200
Elongation %			6-20	2-10

8.2 APPENDIX B REYNOLD FRENCH REPAIR BROCHURE

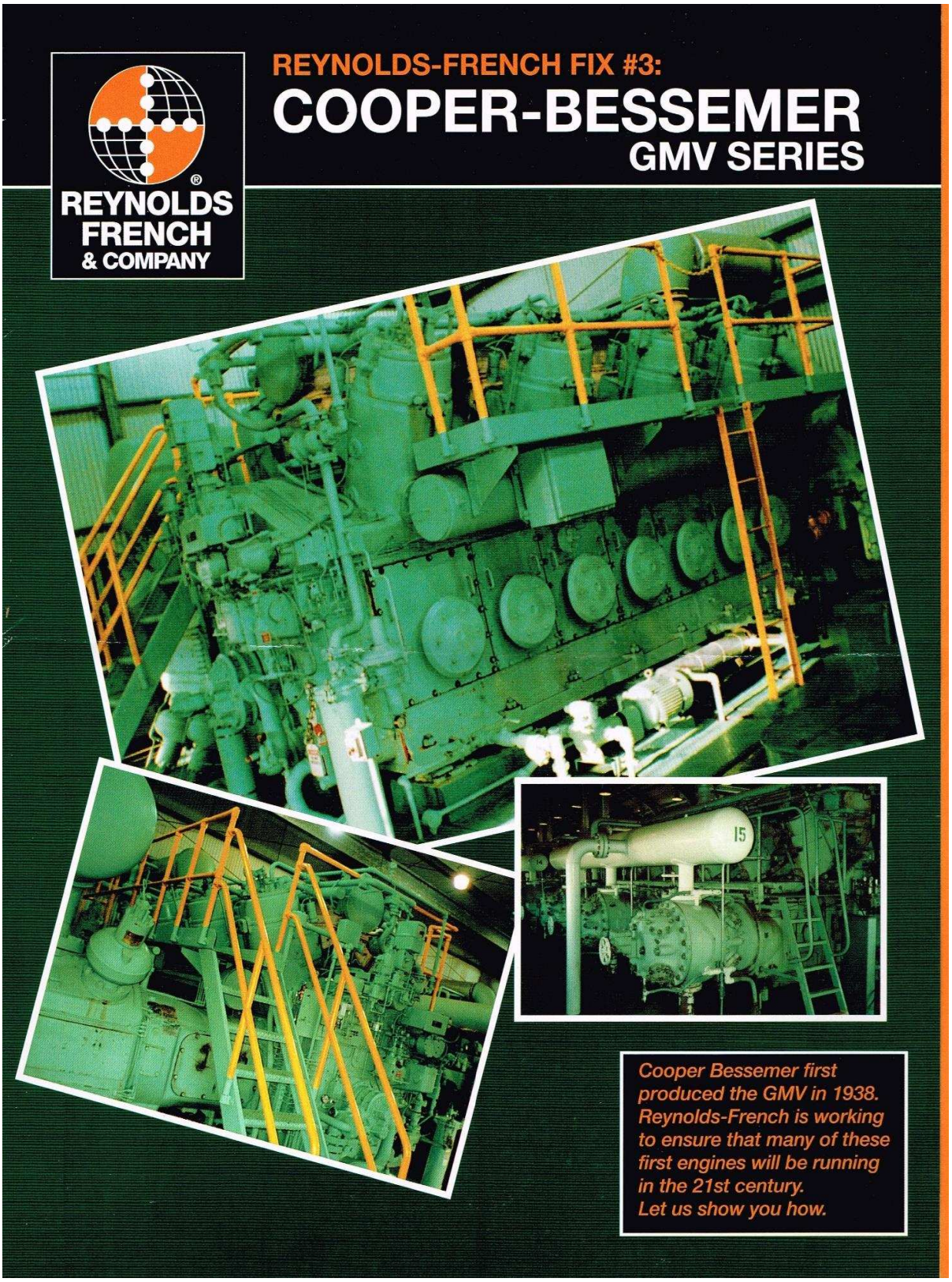

NO ONE HAS REPAIRED MORE GMV SERIES MAIN FRAMES THAN REYNOLDS-FRENCH.

SPREADER BAR AND DOWEL PIN FIT

After years of service, even the best-built equipment will have problems, especially without proper maintenance. This brochure highlights some of the more common problem areas.

Let REYNOLDS-FRENCH inspect and resolve any potential equipment problems you may be having.

Right: GMVC with damaged spreader bar dowel landing replaced. Steel fabrication installed and machined on site.

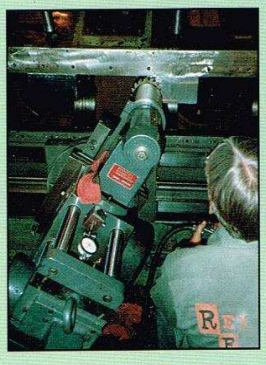

Below: Worn spreader bar dowel pins replaced with oversized pins to correct excessive movement and crankcase door bolt breakage problems.

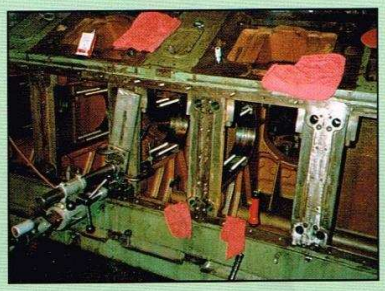

CROSSHEAD GUIDE FLANGE AND AIR BOX

Misalignment of engine, crosshead guide compressor cylinders or bottles can cause major damage to side of main frames.

Right: Crosshead guide flange replaced with steel fabrication and machined on site.

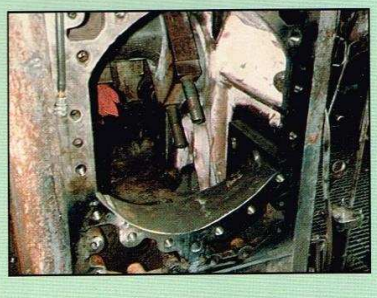

Below left: Damaged wall between airbox and crankcase removed.

Below right: Damaged wall replaced with fabrication and sealed. On site repair.

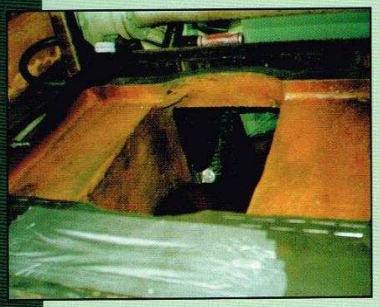

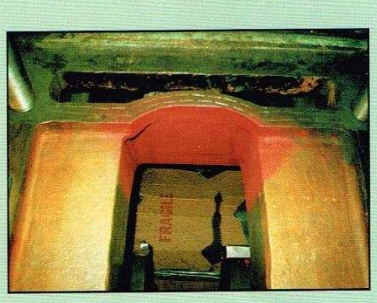

GMV POWER CYLINDER AREA REPAIRS

GMV BASE

The GMV series engines have a common design for the base. As the horsepower was increased with blowers and turbochargers, we found breakage in area shown in the cross sectional drawing to the right. All GMV, GMVTF, GMVA, and GMVC engines built or converted before 1960 should have an annual air box inspection.

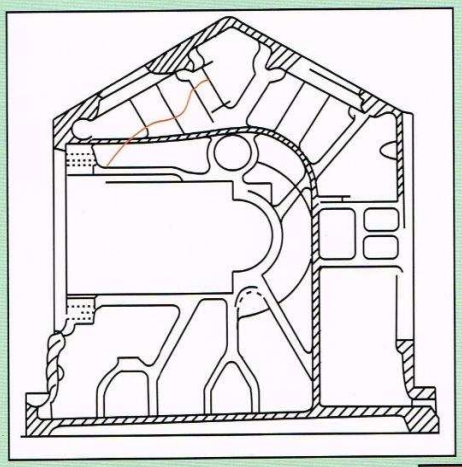

Above: GMV base cross sectional drawing showing area where breakage is found (orange lines).

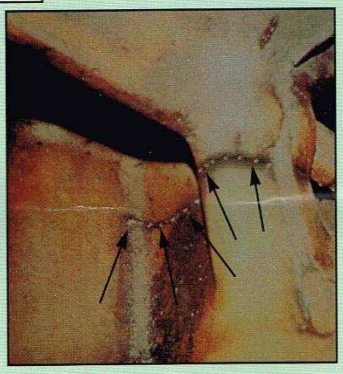

Above: View inside airbox. Cracked power cylinder bolt boss is highlighted (see arrows).

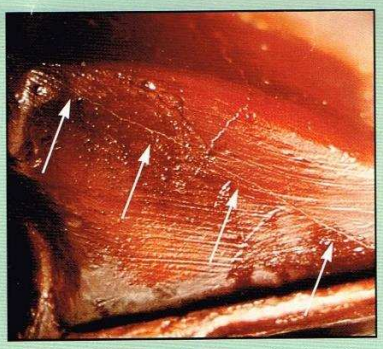

Above: If damage in upper view is not repaired, crack will extend into crankcase webbing in front of main bearing cap (See arrows).

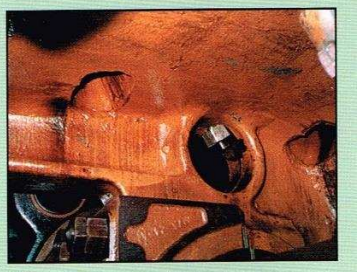

Above: Power cylinder boss is reinforced with special bolt extending from cylinder landing to wrist pin removal hole in crankcase.

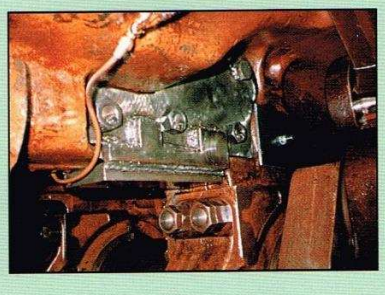

Left: If crack extends as shown in drawing into crankcase, reinforcement will be required.

GMV MAIN SADDLE REPLACEMENT

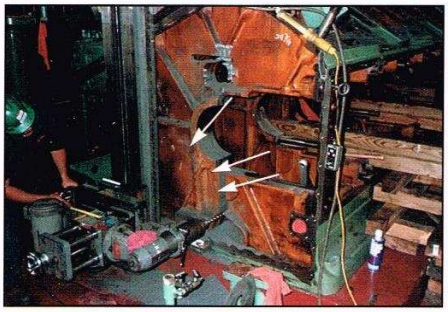

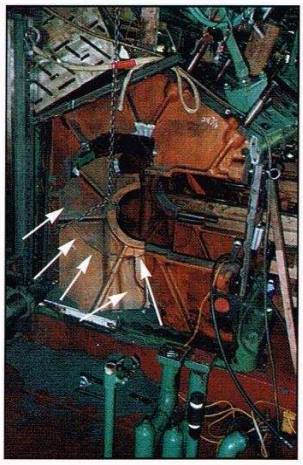

Above: Damaged main bearing being removed by machining.

Upper right: Damaged casting removed. Arrows point out cracked areas.

Lower right: Frame ready to receive fabrication and new main bearing saddle.

Below: Fabrication bolted and secured to cast iron base. Fabrication is welded steel to steel only. Machined to OEM standards.

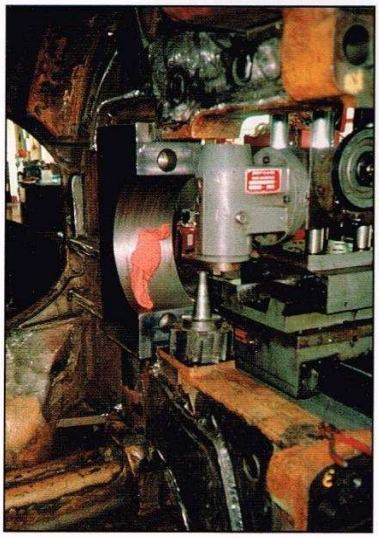

Above: Completed on-site repairs.

A major repair on a GMV, in the field, using steel fabrications and on-site machine work.

REYNOLDS-FRENCH has replaced bearing saddles in many styles of engines using castings or steel fabrications.

FIELD MACHINE WORK

OEM specs maintained by use of portable machine tools and REYNOLDS-FRENCH expertise.

Following are a few of our on-site machine services:

- Portable Milling
- Line Boring
- Crank Pin Turning
- Crankshaft Straightening
- Flange Facing
- Compressor Valve Pockets
- Idler Shaft Bushings
- Crosshead Guides/Flanges

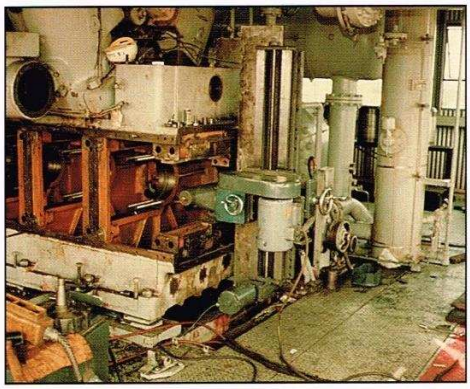

Main bearing cap landing and jaw fit being machined.

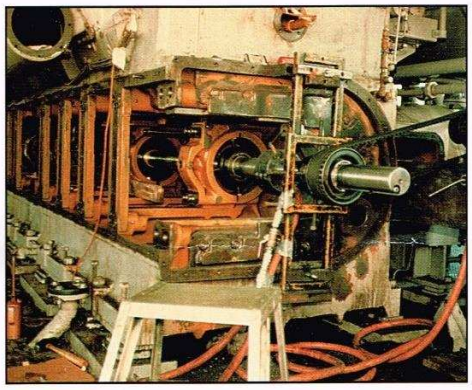

Frame being linebored after repairs to main bearing saddle. Engine bored to OEM standard.

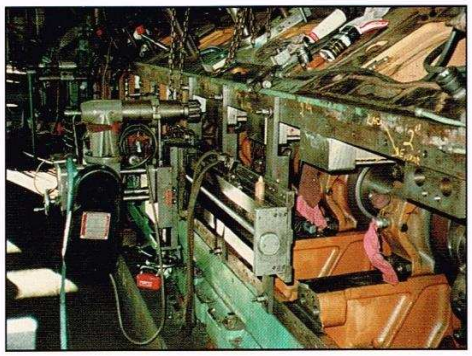

Spreader bar landings and bar fit being milled to size on site.

REPAIR OF POWER CYLINDER HEADS BY BUSHINGS AND METAL LACING

REYNOLDS-FRENCH has repaired and has available many of the hard-to-find GMV cylinder heads.

GMV cylinder head damaged in gas valve hole and spark plug area.

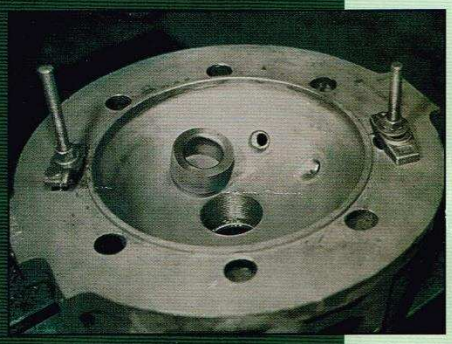

Left: GMV cylinder head bored for bushing in gas valve area. Damaged area removed and will be replaced by bushing screwed in and laced in for complete metal-to-metal contact.

Below: Before and after repairs.

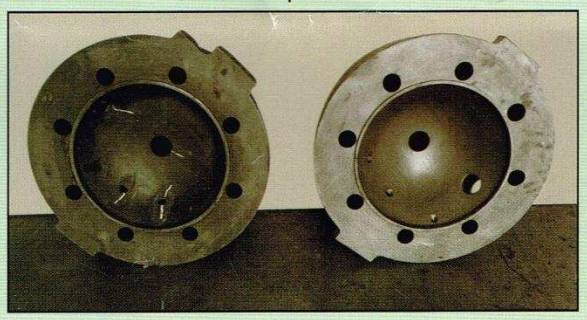

REYNOLDS-FRENCH cold repair on cylinder heads doesn't distort the existing machine surfaces.

REYNOLDS-FRENCH.
Rich in experience. Eager to better serve our customers.

REYNOLDS FRENCH & COMPANY

12525 E. 60th Street
Tulsa, OK 74146-6921
(918) 252-7545
Fax: (918) 252-7540

8.3 APPENDIX C WORKING MODEL SIMULATION

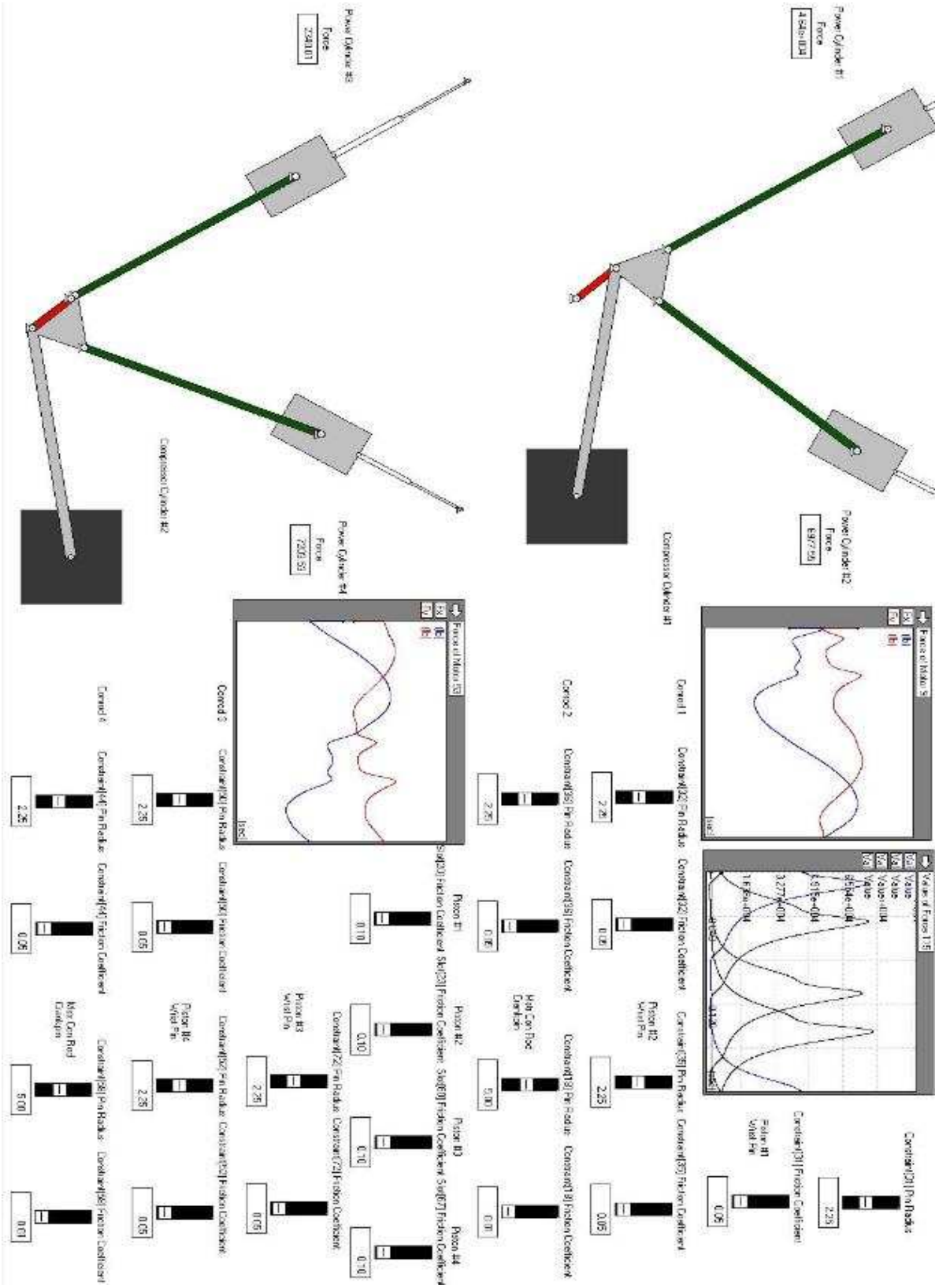

	Bearing Force [lbf]				Pressure Input Forces [lbf]			
Crank Angle [deg]	Fx	Fy	Fx	Fy	Cylinder 1	Cylinder 2	Cylinder 3	Cylinder 4
0	-18820	47330	1430	12450	46410.00	6977.55	2340.012	7203.531
0.25	15010	13730	-29320	41170	46410.00	6977.55	2340.012	7203.531
0.5	14760	13760	-29120	41260	46590.00	7020.96	2339.858	7157.041
0.75	14520	13800	-28920	41350	46760.00	7077.301	2335.394	7108.397
1	14270	13830	-28730	41430	46930.00	7125.946	2330.93	7057.29
1.25	14020	13870	-28530	41520	47110.00	7181.979	2330.16	7008.645
1.5	13760	13940	-28330	41610	47310.00	7239.86	2328.775	6957.845
1.75	13490	14000	-28140	41690	47520.00	7286.195	2325.388	6900.734
2	13220	14090	-27940	41770	47750.00	7342.537	2321.694	6843.931
2.25	12940	14170	-27750	41850	47970.00	7397.954	2323.541	6786.666
2.5	12660	14260	-27550	41920	48200.00	7452.448	2317.691	6728.478
2.75	12370	14360	-27360	42000	48450.00	7511.099	2320.924	6664.747
3	12070	14480	-27160	42080	48720.00	7567.748	2318.461	6609.33
3.25	11760	14620	-26970	42150	49010.00	7621.934	2319.538	6547.293
3.5	11440	14760	-26770	42220	49300.00	7679.815	2317.691	6480.638
3.75	11120	14910	-26580	42290	49600.00	7737.85	2318.307	6412.597
4	10800	15080	-26380	42360	49920.00	7800.81	2316.46	6345.942
4.25	10450	15260	-26190	42430	50260.00	7862.078	2314.612	6281.288
4.5	10100	15460	-26000	42490	50630.00	7919.496	2316.46	6210.168
4.75	9730	15680	-25800	42560	51010.00	7980.764	2315.844	6144.899
5	9360	15910	-25610	42620	51400.00	8043.109	2316.614	6071.008
5.25	8979	16140	-25410	42680	51810.00	8101.451	2315.69	5998.966
5.5	8588	16400	-25220	42740	52240.00	8165.643	2313.997	5925.537

8.4 APPENDIX D STRAIN GAUGE INSTRUMENTATION MANUAL

SPECIFICATIONS		
Strain Gage Construction		Foil strain gage with embedded measuring grid
Measuring Grid		
Material		Constantan
Thickness	µm (microinch)	3.8 or 5 (150 or 197), depending upon strain gage type
Carrier		
Material		Polyimide
Thickness	µm (microinch)	45 ± 10 (1.772 ± 394)
Connections		PTFE wire, Ø - 0.051 mm², approximately 50 mm long, connected to AWG 28 ribbon cables (PVC insulated) through solder sleeves in 2- or 3-wire configurations
Nominal Resistance[1]	Ω	120 or 350 depending upon gage
Resistance Tolerance[1]	%	±0.35
with 0.6 mm and 1.5 mm grid length	%	±1
Gage Factor		approximately 2 (stated on package)
Gage Factor Tolerance	%	±1
with 0.6 mm and 1.5 mm grid length	%	±1.5
Temperature coefficient of gage factor	1/K [1/°F]	(115 ± 10) x 10^{-6} [(64 ± 5.5) x 10^{-6}]
Nominal value of gage factor temperature coefficient		Specified on each package
Reference Temperature	°C (°F)	23
Operating Temperature Range		PTFE cable
for static measurement (zero point related)	°C (°F)	-10 to 155 (-14 to 320)
for dynamic measurement (not zero point related)	°C (°F)	-10 to 155 (-14 to 320)
Transverse Sensitivity for linear 3 mm 120Ω gage	%	±0.2
Temperature Response		Specified on each package
Temperature response as required, adapted to coefficient of thermal expansion		10.8 x 10-6 (6.0 x 10-6)
α for aluminum	1/K [1/°F]	23 x 10-6 (12.8 x 10-6)
α for plastic material	1/K [1/°F]	65 x 10-6 (36.1 x 10-6)
α for austenitic steel	1/K [1/°F]	16 x 10-6 (8.9 x 10-6)
α for titanium	1/K [1/°F]	9 x 10-6 (5.0 x 10-6)
α for molybdenum	1/K [1/°F]	5.4 x 10-6 (3.0 x 10-6)
α for quartz	1/K [1/°F]	0.05 x 10-6 (0.3 x 10-6)
Tolerance of temperature response	°C (°F)	-10 to 120 (-14 to 248)
Mechanical Hysteresis		
1) at reference temperature and strain ε = 1000 µm/m (microstrain) on linear 3 mm 120Ω gage		
at 1st load cycle and adhesive SG496	µm/m (microstrain)	1
at 3rd load cycle and adhesive SG496	µm/m (microstrain)	0.5
Maximum Elongation		
at reference temperature on linear 3 mm 120Ω gage		
Absolute strain value for positive direction	µm/m (microstrain)	20,000 ± 2%
Absolute strain value for negative direction	µm/m (microstrain)	25,000 ± 2.5%
Fatigue Life		
at reference temperature on linear 3 mm 120Ω gage		
Achievable Number of Load Cycles L_v at Alternating Strain ε = ±1000 µm/m and		
zero point variation ≤ 300	µm/m (microstrain)	>1 x 10^7 (test was stopped)
zero point variation ≤ 30	µm/m (microstrain)	5 x 10^6
Minimum Radius of Curvature, Longitudinal and Transverse, at Reference Temperature		
within measuring grid area	mm (inch)	0.3 (0.012)
within solder tab area	mm (inch)	10 (0.394)
Applicable Bonding Materials		
Cold Cure Adhesives		SG496, SG401
Heat Cure Adhesives		TT300

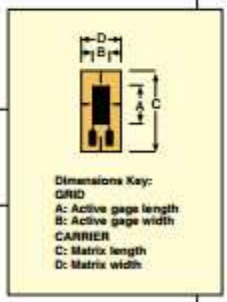

Specifications

Conditions (Unless Noted): Ta = 25°C, Vs = ±15 VDC, G = 500 V/V

Parameter		Minimum	Typical *	Maximum	Units
Amplifier (1)					
Gain Range	Adjustable (2)	100		500	V/V
	w/External Set Resistor	2		5000	
Gain Equation			$R_G = 100.000/(G-2)$		ohms
Gain Equation Accuracy 2 < G < 1000 V/V			3		%
Gain Temperature Coefficient	w/Trimpots		75	150	ppm/°C
	Amplifier alone		25	100	
Nonlinearity, ±10V Output Swing			0.002	0.005	%
Offset Voltage, Input and Output			Adjustable to Zero		
Warmup Drift (3)			±1	±5	µV
Input Offset					
Vs. Temperature:	G = 2V/V		±2	±10	µV/°C
	G = 1000V/V		±0.2	±1	
	At Other Gains, Max.		±0.2 +(20/G)		
Vs. Power Supply			±1	±5	µV/V
Output Offset Adjust Range		±10			V
Input Bias Current (4)			1	5	nA
Vs. Temperature			40		pA/°C
Input Offset Current			1	5	nA
Vs. Temperature			40		pA/°C
Input Impedance (5)			4G ohms || .0047 µF		
Common Mode Input Voltage:	Range, Linear Response		±9		VDC
	Maximum		±15		
CMR (6):	1 kHz bw, DC-60 Hz (7)		100		dB
	10 Hz bw, DC-60 Hz (7)		120		
Input Noise Voltage:	0.1 Hz - 10 Hz		0.3		µV P-P
	10 Hz - 100 Hz		1		
Current:	0.1 Hz - 10 Hz		60		pA P-P
Rated Output:	Voltage, 2 kohm Load	±10			VDC
	Current	±5			mA
	Load Capacitance			1000	pF
	Short Circuit		1 minute		
Dynamic Response (8):	Small Signal Bandwidth		Adjustable		kHz
	Amp Response (see Curve 3)				
Low Pass Filter (9):	Number of Poles		2		
	DC Gain (Pin P to N)		+2		V/V
	Roll Off		40		dB/Dec
Bridge Excitation Supply (10)					
Output Adjustment Range:	w/Trimpot	4		10	VDC
Output Current		0		120	mA
Load Regulation I_L = 0 - 120 mA			0.02	0.05	%
Line Regulation Vin = 14.5 - 16 VDC			0.005	0.01	%/V
Stability (11):	Short Term		0.05		%/24 Hrs
	Long Term		0.2		%/Mnth
	Vs. Temperature		40	80	ppm/°C
	Warm-up Drift		0.01		%
Short Circuit Protection			Short Term - 10 minutes		
Output Noise, 10 Hz - 1 kHz			200		µV P-P
Half Bridge Completion					
Nominal Resistance Value			10		kohms
Initial Accuracy				0.1%	%
Temperature Tracking				5	ppm/°C
Balance Adjustment Range, 350 ohm Bridge			±15		mV
Power Requirements					
Voltage:	Rated Performance		±15		VDC
	Operating	±13		±16	
Current (12)			±12		mA
Environmental					
Ambient:	Operating	-25		53	°C
	Storage	-40		80	

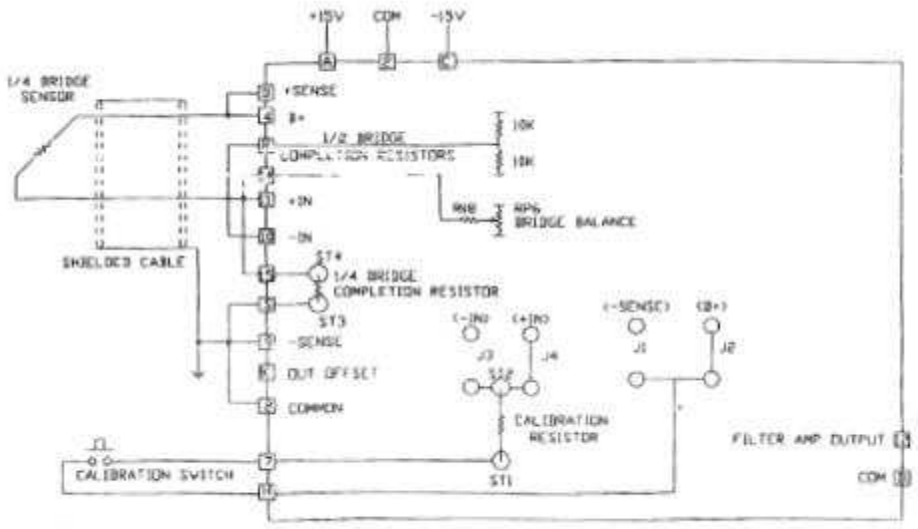

FIGURE 8. 1/4 Bridge - 2 Wire

8.5 APPENDIX E STRAIN GAUGE MOUNTING INSTRUCTIONS

OMEGA®
User's Guide

Shop online at omega.com®
e-mail: info@omega.com
For latest product manuals: www.omegamanual.info

SG401

SG496

SG401 and SG496
Rapid Cure Strain Gauge Adhesives

SECTION 1 - INTRODUCTION

OMEGA's Rapid Cure Adhesives, SG401 and SG496 are modified versions of a solvent-free cyanide-acrylate adhesive specially developed to apply strain gauges of the bonded-resistance type. They are suitable for all series of strain gauges and compatible with most metals of common use and with most synthetic materials. They are not suitable, however, for use with porous materials such as concrete, wood, foam plastic, etc.

This series of Strain Gauge Adhesives is supplied in three different packages. Their part numbers and weights are listed below:

Part Number	Net Weight
SG401	0.10 oz.
SG496	1.00 oz.

SECTION 2 - SETTING AND CURING NOTES

Polymerization (setting) of cyanide-acrylate adhesives occurs by the catalytic reaction of moisture absorbed from the air. The most favorable conditions are given by a relative humidity (RH) between 40% and 70%. In the case of RH less than 30%, the reaction is noticeably retarded and in extreme cases, completely stopped. More than 80% RH causes shock setting. Internal stresses in the adhesive layer caused by shock setting reduce the maximum extensibility of the bond. One should, therefore, always ensure that the limit values of 30% and 80% RH are not exceeded.

Complete setting in the given time is achieved only with thin films. Thick layers of adhesive set very slowly and incompletely; therefore, extremely rough contact surfaces are unsuitable.

The setting speed depends on the chemical condition of the components to be bonded. Alkaline materials accelerate polymerization, whereas acid materials not only retard but can completely prevent setting. (In the latter case, a neutralizer should be used.) Representative figures for the setting time and its dependence upon the quoted materials at a temperature of 20°C (68°F) and an RH of 65% are given in Table 2-1. At the end of these periods, the adhesive will have set sufficiently to allow cable connection to be initiated. **Ultimate curing is achieved after some 24 hours.** However, measurements can be taken after the periods quoted in Table 2-2.

TABLE 2-1
MINIMUM SETTING TIME FOR BONDING

Material	Setting Time
Steel	60 to 120 sec.
Aluminum	50 to 100 sec.
Plastics	10 to 60 sec.

TABLE 2-2
MINIMUM CURING TIME FOR MEASUREMENT

Type of Measurement	Curing Time	
	At 5°C (41°F)	20°C (68°F)
Dynamic	90 min.	10 min.
Static	120 min.	15 min.

SECTION 3 - PREPARING THE SURFACE

The object of preparation is to create a smooth surface that can be wetted. The following steps, which require attention or can be bypassed, depends on the condition of the test piece.

3.1 Coarse Cleaning

Rust, scale, paint, and other such contaminants must be removed from the test area and its surroundings.

3.2 Smoothing Surface

Pitting, protrusions, scratches, and other such imperfections must be removed by grinding, filing, or other suitable methods.

3.3 De-greasing

The choice of a cleaning agent depends on the nature of the contamination and whether the surface is adversely affected by a given cleanser. Powerful grease solvents such as Freon TF, Chlorothene NU, methyl-ethyl-ketone, acetone, and trichlorethylene are normally used. Wax and similar substances dissolve in toluene.

The surface to be cleaned should be washed with gauze pads soaked in solvent. Initial treatment should cover a somewhat larger area than that which is ultimately required. As each new pad of gauze is taken, the zone that receives attention should be progressively reduced to minimize the possibility of continually introducing new particles of dirt from the edges of the zone. Large areas can be brushed with water and an abrasive powder (e.g. AJAX, COMET, etc.). After rinsing, there should remain a surface which is completely wetted with an unbroken film of water. The surface is then dried with a clean cloth (paper towel) or by heat. Ultrasonic cleaning baths or steam degreasing apparatuses can also be used with good effect.

NOTE

The solvent must be chemically clean and should leave no residue. It should never be used directly from the container in which it is stored. A quantity should be transferred to a clean bowl and used from there. Unused fluid in the bowl should never be returned to stock! Use pads of gauze just once and then dispose of them. Never dip a used pad into the solution a second time!

3.4 Surface Roughening

The adhesion between bonded parts depends on the adhesion of the cement with the surfaces wetted by it. Roughening of the surface on the specimen will improve the adhesion by increasing the active surface. Emery paper or cloth should be moved in circles in order to avoid any preferred direction of grooves. Make sure to use only fresh emery paper of a grade that matches the hardness of the specimen material (e.g., for steel use grade 80 to 180; for aluminum use grade 220 to 360). If the roughness becomes too great, air bubbles might form which would prevent effective bonding. The material must be absolutely free of oil and grease. Any surface grooving that might have resulted from the foregoing process must be removed.

If one is familiar with etching processes, this too is possible. If no interference with the surface finish of the test piece is acceptable, the adhesives can be used on smooth or polished surfaces, although its maximum extensibility is then reduced.

3.5 Fine Cleaning

All dirt and dust resulting from the roughening process should be removed carefully. This is achieved with gauze pads soaked in one of the solvents noted in section 3.3. Each pad should be held with clean tweezers and passed over the surface only once. The process should be repeated until the pads show no trace of discoloration. Possible remaining lint should be removed with clean tissue paper. Keep the cleaned area dry! Do not blow with breath or touch with fingers!

To avoid the incidence of new oxidation, the mechanical or chemical treatment of the surface should occur just before adhesion.

SECTION 4 - PREPARATION OF THE STRAIN GAUGE

Prior to attaching the gauge, some users prefer to solder the connections between the gauge and terminal pad, while others prefer to solder after attaching the gauge.

The bonding side of the strain gauge should be carefully cleaned with a gauze pad soaked in Freon, Frigen, or carbon-tetrachloride. Residual moisture must be dried by a radiant heater or a hot-air blower. During this procedure, the strain gauge must be held by tweezers.

SECTION 5 - ATTACHING THE STRAIN GAUGE

Because of the short curing time, it is not possible to readjust the position of the strain gauge once the adhesion process has been initiated.

The gauge width should be extended with a short length of adhesive tape affixed to the upper surface of the gauge, away from the connections. If soldering is to be done after attaching the gauge, protect the solder terminals with tape.

The strain gauge is laid onto the cleaned area of the test piece, and after careful alignment, the protruding part of the adhesive tape is pressed onto the surface (use tweezers). This results in a hinge-like fixture that allows the strain gauge to flap up and down without changing its alignment (see Figure 5-1).

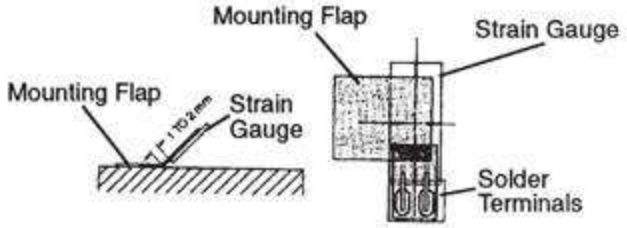

Figure 5-1: Strain Gauge and Mounting Flap

Flip the strain gauge up to expose the adhesion area. Cut off a length of the Teflon® film. If the adhesion area is more than 15 mm (0.6 inch) wide, cut the Teflon strip diagonally. Place one drop of the adhesive onto the adhesion area. Using the Teflon film, distribute the adhesive into a uniformly thin layer by brushing over it just once and lightly pressing the Teflon film downwards. Use as little pressure as possible (see Figure 5-2) because the adhesive will cure immediately if the pressure is too great.

Acid materials delay or inhibit setting of the adhesive. If the bonding surface is acidic, apply a thin coat of neutralizer onto the bonding side of the strain gauge, just enough to wet it. Allow this to dry.

The strain gauge is then carefully flapped over to meet the adhesive surface and covered with Teflon film. Press the Teflon film covering the

adhesive tape and strain gauge until the adhesive has set (see Table 2-1). After a few minutes, remove the Teflon film and carefully release the strain gauge connections from the adhesive. The thickness of the adhesive film in a correctly adhered gauge is 8 micrometers ± 20%. After curing, remove the alignment adhesive tape by peeling it back onto itself at an acute angle.

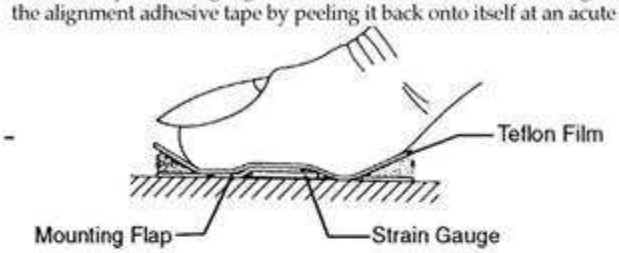

Figure 5-2 : Affixing the Strain Gauge

Experience has shown that problems with the setting of cyanide-acrylates are due mainly to layers of adhesive that are too thick. Therefore, a neutralizer should be used only if a very thin adhesive layer can be guaranteed. The measuring point should be protected against damp chemicals and mechanical damage.

Experience has shown that problems with regard to the setting of cyanide-acrylates are due mainly to layers of adhesive which are too thick. Therefore, a neutralizer should be used only if a very thin adhesive layer can be guaranteed. The measuring point should be protected against damp chemicals and mechanical damage.

SECTION 6 - ATTACHING THE LEAD WIRES

Solder all terminals and secure the instrumentation wire in place, either with adhesive or by mechanical means (see Figure 6-1). After soldering, it is imperative that all soldering points are cleaned of flux residues (even non-corrosive fluxes are hygroscopic and require cleaning).

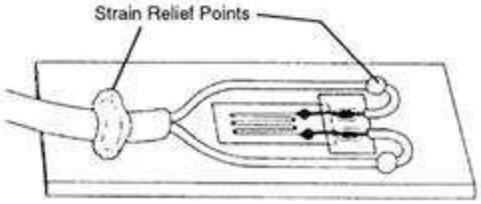

Figure 6-1: Strain Gauge and Lead Wires

A covering should be used to protect the strain gauge from environmental effects. De-grease the entire area and apply the covering (a layer of adhesive) over the strain gauge and lead wire assembly, as shown in Figure 6-2. Cover at least 20 mm (0.8 inch) of the lead wire.

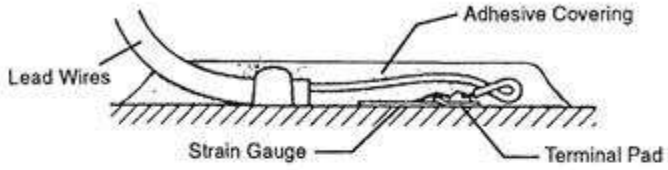

Figure 6-2: Covered Strain Gauge

SECTION 7 - STORAGE

Keep the bottle (or tube) in an upright position, to prevent the adhesive from dripping out and hardening at the drip nozzle and on the screw cap thread. If the adhesive has not been used for a long time, it will harden and seal the tip. Once the tip has been cleaned or cut, the adhesive can be reused.

Protect the adhesive from heat, sunlight, and humidity. Store it in a cool, dry place. The adhesive can be used until its viscosity rises considerably.

A virtually unlimited storage life can be achieved if the adhesive is kept frozen at -15°C (5°F). Before use, defrost the adhesive, making sure it has reached ambient temperature. Repeated freezing does not affect the adhesive.

SECTION 8 - SAFETY MEASURES

Observe the safety regulations, valid in your country, which are designed to avoid accidents associated with the use of adhesives and solvents.

The adhesive itself can do no serious physiological harm. Since it clings to the skin, however, contact should be avoided. Protective goggles should be used. Should, however, the adhesive come into contact with the eyes, rinsing thoroughly with water or boracic solution is necessary. A doctor should be consulted immediately. From previous experience, it has been found that corneal damage heals within a few days and sight remains unimpaired.